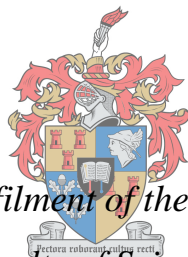


# **A combined computational and experimental study of dichromic crystals**

by

Dirkie Coenraad Myburgh



*Thesis presented in partial fulfilment of the requirements for the degree of  
Masters of Science in the Faculty of Science at Stellenbosch University*

UNIVERSITEIT  
iYUNIVESITHI  
STELLENBOSCH  
UNIVERSITY

100  
1918 · 2018

Supervisor: Prof L. J. Barbour

Co-supervisor: Prof C. Esterhuysen

Department of Chemistry & Polymer Science

Faculty of Science

Stellenbosch University

March 2018

## **DECLARATION**

By submitting this thesis electronically, I Dirkie C. Myburgh declare that the entirety of the work contained therein is my own, original work, that I am the sole author thereof (save to the extent explicitly otherwise stated), that reproduction and publication thereof by Stellenbosch University will not infringe any third party rights and that I have not previously in its entirety or in part submitted it for obtaining any qualification.

*Copyright © 2018 Stellenbosch University  
All rights reserved*

## Abstract

A combination of theoretical and experimental techniques were used in three studies related to dichromic crystals. The first study involves a porous crystal of a Schiff base-containing trianglimine compound undergoing a yellow-to-red colour conversion above a humidity of 55%. Schiff bases are well known for undergoing enolimine-ketoenamine transformations as iono-, solvato-, thermo- or photochromic processes, altering the visible colour properties of the system. In this study a similar transformation occurs owing to the combination of a sorptiochromic and a hydrochromic process, which are both considered as subcategories of solvatochromism. The enolimine-ketoenamine transformation is caused by H-bond formation between water and the oxygen atom of the enol group. This weakens the OH bond allowing a proton transfer from the oxygen to the nitrogen atom. In the presence of H<sub>2</sub>O the ketoenamine state is thermodynamically preferred, whereas in the gas phase the enolimine is preferred.

Secondly, a phase study was performed on a diarylethene compound (1,2-bis(5-pyridyl-2-propyl-3-thienyl)perfluorocyclopentene), **DA-2-[o]**. Diarylethenes are well known for undergoing a ring-closure reaction under UV light and have been shown to exhibit photochromic behaviour in the crystalline state, as is the case for the three polymorphic phases identified for **DA-2-[o]**, **DA-2-[o]- $\alpha$** , **DA-2-[o]- $\beta$**  and **DA-2-[o]- $\gamma$** . The first two are obtained by recrystallisation from acetone and hexane, while the third can be obtained by heating of either **DA-2-[o]- $\beta$**  above 70 °C or **DA-2-[o]- $\alpha$**  above 100 °C. The **DA-2-[o]- $\alpha$**  phase is converted to the **DA-2-[o]- $\beta$**  phase by heating above 100 °C and subsequent cooling to room temperature. The opposite conversion can be achieved by leaving **DA-2-[o]- $\beta$**  in a cupboard under ambient conditions for a period of six months. This result combined with lattice-energy calculations suggests that the **DA-2-[o]- $\alpha$**  phase is the thermodynamically preferred phase.

The final study provides a fundamental explanation for the photoisomerisation reaction of diarylethenes. This was done by developing a method whereby all the major parameter differences between the ring-opened and ring-closed forms are scanned followed by the calculation of the excited state potential energy surface map. This method was then used to illustrate how various structural modifications will affect the ring-closure or ring-opening reaction. The photochromism of the open form was ascribed to the formation of an electron hole after electron excitation from the HOMO to the LUMO. This results in an attractive force between the two adjoining carbon atoms and a downward energy gradient, over the conical intersection, towards the closed form. For the ring-opening it was observed that a twisting action is required before the ring-opening can take place making this an asynchronous process.

## Uittreksel

'n Kombinasie van teoretiese en eksperimentele tegnieke is gebruik in drie studies wat handel oor dichromatiese kristalle. Die eerste studie behels 'n poreuse Schiff-basis bevattende trianglimien verbinding wat 'n geel-tot-rooi kleur verandering ondergaan bo 'n humiditeit van 55%. Schiff basisse is bekend daarvoor dat hulle enolimien-ketoenamien transformasies ondergaan via iono-, solvato-, termo- of fotochromiese prosesse wat gepaard gaan met 'n kleur verandering. In hierdie studie vind 'n soorgelyke transformasie weens 'n kombinasie van 'n sorptiochromiese en 'n hidrochromiese proses plaas. Beide word as sub-kategorieë van solvatochromatisme beskou. Die enol-keto transformasie word aangedryf deur die vorming van waterstofbindings tussen H<sub>2</sub>O en die enol groep. Die OH binding word verswak waarna die waterstof atoom na die stikstof verskuif. In die teenwoordigheid van water is die ketoenamien vorm termodinamies meer gunstig terwyl die enolimien in die gas fase verkies word.

Tweedens is 'n fase studie uitgevoer op 'n diarieleteen verbinding (1,2-bis(5-piridiel-2-propiel-3-tiëniel)perfluorosiklopenteen), **DA-2-[o]**. Diarieleteen verbindings ondergaan 'n ring-vorming onder UV lig. Soms kan hierdie proses plaasvind selfs in die kristal vorm wat die geval is vir die drie polimorfiese fases wat geïdentifiseer is vir **DA-2-[o]**, **DA-2-[o]-α**, **DA-2-[o]-β** en **DA-2-[o]-γ**. Die eerste twee kan verkry word deur **DA-2-[o]** vanaf asetoon en hekasaan respektiewelik te kristalliseer terwyl die derde verkry kan word deur verhitting van of **DA-2-[o]-β** bo 70 °C of **DA-2-[o]-α** bo 100 °C. Verder kan die **DA-2-[o]-α** fase omgeskakel word na die **DA-2-[o]-β** fase deur verhitting bo 100 °C en daaropvolgende verkoeling tot kamer temperatuur. Die teenoorgestelde omskakeling kan bereik word deur **DA-2-[o]-β** in 'n kas vir ses maande te laat staan. Hierdie resultaat, saam met rooster-energie berekeninge, vir beide sisteme, dien as bewys dat die **DA-2-[o]-α** fase termodinamies verkies word.

In die laaste studie word die fotoisomerisasie reaksie van diarieleteen verbindings verduidelik deur hierdie fotochemiese reaksie te bestudeer vanaf 'n nuwe benadering. Hierdie metode is dan gebruik om te illustreer watter effek verskeie strukturele modifikasies op die ring-vorming- of ring-openingsreaksie sal hê deur na kombinasies van potensiële-energie kurwes van die grond en opgewekte toestande te kyk. Die fotochromatisme van die oop vorm kan aan die vorming van 'n elektron leemte na die opwekking van 'n elektron vanaf die HOMO na die LUMO toegeskryf word. Dit veroorsaak 'n aantrekkingskrag tussen die twee koolstof atome, waartussen die binding vorm, en 'n afwaartse energie gradient in die rigting van die geslote-ring toestand. Vir die ring-openings-reaksie word 'n draai-aksie vereis voordat die ringopening kan plaasvind wat hierdie reaksie dus 'n twee-stap proses maak.

## **Acknowledgements**

I would like to extend my sincerest gratitude towards the following people and parties:

My supervisor Leonard J. Barbour for the incredible opportunity to do my masters in his research group and for always encouraging me and my co-students to excel and reach for excellence during our pursuit to becoming well-rounded scientists.

My co-supervisor Catharine Esterhuysen for her patient, excellent and consistent guidance during not only my masters' studies but also throughout my undergraduate and honours degrees.

My colleagues in the De Beers building from both the computational and the supramolecular groups. A lot of insightful discussions, advice and assistance from many different parties helped guide this project to its completion.

My family and friends for a lot of patience, support and love.

University of Stellenbosch for the privilege to study at such an excellent institute as well as for all the equipment and resources necessary for this project.

Lastly I want to thank the National Research Foundation for funding without none of this would have been possible.

## List of abbreviations and symbols

$\hat{T}_e$	Kinetic energy operator for electrons
$\hat{T}_n$	Kinetic energy operator for nuclei
$\hat{V}_{ee} = \hat{W}$	Repulsive potential energy operator between electrons
$\hat{V}_{ne}$	Attractive potential energy operator between nuclei and electrons
$\hat{V}_{nn}$	Repulsive potential energy operator between nuclei
$E_{\text{HK}}$	Hohenberg-Kohn functional
$\Phi_{\text{SD}}$	Slater determinant
$E_{\text{XC}}$	Exchange correlation energy
$\hat{H}$	Hamiltonian operator
$\hat{O}$	Physical observable
$\hat{U}$	Time evolution operator
$\hat{T}$	Time-ordering operator
$\Delta E$	Difference in energy
$^{\circ}\text{C}$	Degrees Celsius
3-D	three dimensional
$\text{\AA}$	Angstrom
AO	Atomic orbital
Ar	Aryl
asu	Asymmetric unit
CASSCF	Complete Active Space SCF
CCDC	Cambridge Crystallographic Data Centre
CI	Configuration interaction
CSD	Cambridge Structural Database
DCM	Dichloromethane
DFT	Density Functional Theory
DNP+	Double Numerical plus polarization
DSC	Differential Scanning Calorimetry
E	Energy
GUI	Graphical User interface
HF	Hartree-Fock
HOMO	Highest Occupied Molecular Orbital
IR	Infrared

IUPAC	International Union of Pure and Applied Chemistry
kcal/mol	kilocalories per mole
LUMO	Lowest Unoccupied Molecular Orbital
MO	Molecular orbital
nm	nanometre
PCM	Polarisable Continuum Model
PES	Potential Energy Surface
ps	picoseconds
PXRD	Powder X-Ray Diffraction
SCF	Self-consistent field
SCRf	Self-consistent reaction field
SCXRD	Single-crystal X-Ray diffraction
TDDFT	Time-Dependent Density Functional Theory
UV	Ultra-Violet
Vis	Visible
VT-PXRD	Variable Temperature Powder X-Ray diffraction
VT-SCXRD	Variable Temperature Single-crystal X-Ray diffraction
ZPVE	Zero point vibrational energy
$\alpha$	alpha
$\beta$	beta
$\gamma$	gamma
$\psi$	Wave function
$n$	Electron density
$v$	External potential

# Table of Contents

<b>DECLARATION</b> .....	<b>i</b>
<b>Abstract</b> .....	<b>ii</b>
<b>Uittreksel</b> .....	<b>iii</b>
<b>Acknowledgements</b> .....	<b>iv</b>
<b>List of abbreviations and symbols</b> .....	<b>v</b>
<b>Table of Contents</b> .....	<b>vii</b>
<b>Chapter 1: Introduction</b> .....	<b>1</b>
1.1 Supramolecular chemistry.....	1
1.2 Computational chemistry .....	2
1.3 Dichromism and other chromic phenomena .....	3
1.4 Schiff bases and trianglimines .....	3
1.5 Diarylethenes .....	4
1.6 Aims, objectives and outline .....	5
<b>Chapter 2: Theoretical Background</b> .....	<b>7</b>
2.1 Quantum mechanics.....	7
2.1.1 The Time-Independent Schrödinger Equation .....	8
2.1.2 The Born-Oppenheimer approximation .....	9
2.1.3 Variational principle.....	10
2.1.4 The Hartree-Fock Approximation .....	11
2.1.5 The Time-Dependent Schrödinger Equation.....	12
2.1.5.1 Time evolution operators .....	13
2.1.6 Basis Sets .....	14
2.2 Density Functional Theory (DFT) .....	15
2.2.1 Electron density and the Hohenberg-Kohn Theorems.....	15
2.2.1.1 The First Hohenberg-Kohn Theorem: Proof of Existence .....	16
2.2.1.2 The Second Hohenberg-Kohn Theorem: Variational Principle .....	17
2.2.2 The Kohn-Sham approach.....	18
2.3 Time-Dependent Density Functional Theory (TD-DFT).....	19
2.3.1 The Runge-Gross Theorem .....	19
2.3.2 The van Leeuwen Theorem.....	20

<b>Chapter 3: Methodology</b> .....	<b>21</b>
3.1 Compounds investigated .....	22
3.1.1 Experimentally obtained compounds .....	22
3.1.1.1 Hexahydroxy-hexaazaheptacyclo-octatetraconta-pentadecaene .....	22
3.1.1.2 Perfluorocyclopentene-diyl-bis-propylthiophene-diyl-dipyridine .....	23
3.1.1.3 Perfluorocyclopentene-diyl-bis-propylthiophene-diyl-diphenyl .....	24
3.1.2 Model compounds .....	25
3.1.2.1 Bis-cyclohexylimino-methyl-benzene-diol .....	25
3.1.2.2 Diarylethenes .....	25
3.2 Analytical techniques .....	26
3.2.1 Single-Crystal X-Ray Diffraction.....	26
3.2.2 X-Ray Powder Diffraction .....	26
3.2.3 Differential Scanning Calorimetry .....	26
3.2.4 Hotstage Microscopy.....	27
3.3 Structural elucidation software .....	27
3.3.1 Cambridge Structural Database version 5.38 .....	27
3.3.1.1 Conquest 1.19 .....	27
3.3.1.2 Mercury 3.9.....	27
3.3.2 XSeed 4.0.....	27
3.4 Computational software .....	28
3.4.1 Gaussian 09 .....	28
3.4.2 Materials Studio 2016 .....	28
3.4.3 Visualisation and processing of data .....	28
3.5 Computational Methods .....	29
3.5.1 Density functionals.....	29
3.5.2 Basis sets .....	30
3.5.3 Geometry optimisations .....	30
3.5.4 Frequencies .....	30
3.5.5 Zero-point corrected energies.....	31
3.5.6 Lattice energies .....	31
3.5.7 Scans .....	32
3.5.8 Solvent model.....	32
 <b>Chapter 4: A theoretical explanation for the solvatochromic behaviour of hexahydroxy-hexaazaheptacyclo-octatetraconta-pentadecaene crystals</b> .....	 <b>33</b>
4.1 Aims and objectives .....	34
4.2 Methods .....	35
4.3 Determination of a model system .....	35

4.4	Stable hydrated states .....	38
4.5	Proposed Mode of interaction of trianglimine 1 with water .....	40
4.6	Discussion .....	46
4.7	Summary .....	46
<b>Chapter 5: Reversible phase transition of a photochromic diarylethene: perfluoro-cyclopentene-diyl-bis-propylthiophene-dipyridine .....</b>		<b>48</b>
5.1	Aims and objectives .....	49
5.2	Methods .....	50
5.3	Results .....	50
5.4	Discussion .....	58
5.5	Summary .....	60
<b>Chapter 6: Photochromic behaviour of diarylethene crystals .....</b>		<b>61</b>
6.1	Aims and objectives .....	62
6.2	Methods .....	62
6.3	The diarylethene photoisomerisation .....	64
6.3.1	Identifying major parameter differences .....	64
6.3.2	Scanning all the major parameters .....	64
6.3.3	Excited state potential energy surfaces .....	66
6.3.4	Ring-closure reaction .....	67
6.3.5	Ring-opening reaction .....	68
6.3.6	Conical intersection and the crossing of states .....	68
6.4	Influence of structural modifications on photoisomerisation .....	71
6.5	Discussion .....	81
6.6	Summary .....	82
<b>Chapter 7: Conclusion and Future work .....</b>		<b>83</b>
7.1	Conclusion .....	83
7.2	Future Work .....	85
<b>References .....</b>		<b>87</b>
<b>Supplementary information .....</b>		<b>92</b>

## Chapter 1: Introduction

Colour plays a vital role in our everyday life and to date a myriad of books have been dedicated to the understanding and study of the origin, manipulation and application of colours in materials to make our life easier in some way or another.<sup>1-3</sup> While the origin of colour has become very well understood over the past few centuries, the interest lies in the manipulation of colour within materials as this finds widespread applications in many areas of the arts and sciences, with so many examples that an attempt to mention a few will exclude most.

Depending on the application there are several desired outcomes when it comes to the design and manipulation of colour in materials. The first is to design a material or substance to be a certain colour and to stay that colour. The purple coloured dye mauveine<sup>4</sup> is one such example. Discovered in 1856, this dye sparked the industrialisation of organic chemistry.<sup>5</sup> Other examples include the indigo dye<sup>6</sup> that has been used for centuries as the colouring agent for jeans, paint used in art and for aesthetic purposes, and the coloured glass filters used in traffic lights. Secondly, a material can be designed to appear one colour under certain conditions but a different colour under another set of conditions, thus exhibiting chromic behaviour and acting as a type of sensor. Such molecules or materials find applications in areas from medicine<sup>7</sup> to robotics<sup>8</sup> to temperature sensitive indicators on food and beverage packaging. The third outcome is a material of which the colour can be altered with some form of external stimulus such as light, heat, friction, pressure, humidity, solvent polarity or pH.<sup>2</sup> Such mechanisms are employed in new methods for developing colour display materials<sup>9</sup> as a substitute to the current, commonly-known and used, liquid crystal displays (LCDs).

One can consider a fourth category where the interest shifts towards the other properties of the material and the colour change is simply a by-product that need not be present. Similar to the third outcome mentioned above such materials can be altered with some form of external stimulus but with the aim of changing some property within the material such as thermal or electrical conductivity. Such systems can still have all the properties and characteristics of a chromic system, only without the visible change in colour.<sup>2</sup> This type of system can be found in molecular switches<sup>10</sup> and molecular motors,<sup>11</sup> of which there are already many biological examples<sup>12</sup> and many potential practical applications as well.<sup>13,14</sup>

### 1.1 Supramolecular chemistry

In 2002 Irie et al. studied how diarylethenes, that exhibit photochromic behaviour in solution, behave once crystallised and showed how these molecules often lose their chromic ability once

in the solid state.<sup>15</sup> The reverse is also possible with a molecule only exhibiting chromic behaviour once in the solid state as is the case for a molecule studied as part of this work. Most applications within either of the above-mentioned categories involve some solid state material and therefore it is important to study the solid state as this is where chromic molecules have the greatest potential to be of practical use.<sup>11,16-18</sup> Studying crystals within the context of supramolecular chemistry is one approach to better understanding how molecules, that do or do not exhibit chromic behaviour in solution, will behave once incorporated into some form of solid state material.

In a broad sense supramolecular chemistry can be described as the study of intermolecular interactions that govern self-assembly in the solid state.<sup>19</sup> A crystal can generally be described as an entity that consist of a regular, three-dimensional arrangement of atoms or molecules with a discrete diffraction pattern, although reality is more complicated.<sup>20</sup> The diffraction pattern can be measured via single crystal X-ray diffraction and analysed to determine a crystal structure, which is the arrangement of atoms and molecules in the crystal. Combining this approach to studying the solid state with theoretical methods can be a good approach to studying not only how molecules prefer to self-assemble but also why they assemble in a certain manner.

## 1.2 Computational chemistry

Computational chemistry is a field of chemistry that makes use of computer programs for the prediction of properties of atoms, molecules and materials. These programs are based on theoretical chemistry, which can be described as the mathematical descriptions of chemistry.<sup>21,22</sup> An example would be quantum theory that is computationally incorporated into the Gaussian<sup>23</sup> program, and can be used to calculate energies and the distribution of electron density within a molecular system, along with a variety of derived properties.

Computational methods are extremely helpful tools for studying systems or properties that are otherwise difficult or impossible to observe, obtain or measure experimentally. An example of such a system is the photochromic diarylethene that undergoes a ring-closure upon irradiation with UV light.<sup>24,25</sup> This reaction takes place on a sub-10-ps time scale, which makes it difficult to study the exact mechanism by which the reaction proceeds. Theoretical modelling can provide otherwise unobtainable insight into the mechanisms of these and other chromic phenomena.

### 1.3 Dichromism and other chromic phenomena

All types of chromic phenomena can be divided into six overarching categories based on the type of external stimulus that brings about the colour change. These are electrochromism (change in current), ionochromism (interaction with an ionic species), mechanochromism (when a chemical or material is put under some form of mechanical stress), photochromism (electromagnetic radiation), solvatochromism (difference in colour when dissolved in different solvents) and thermochromism (change in temperature).<sup>2</sup> There are, however, many intricacies when it comes to defining chromic phenomena and the definitions given are only general. All of these categories can also be divided into a range of subcategories to describe different variations and one system can fall in more than one category at the same time.<sup>2</sup>

Dichromism specifically refers to compounds that can alternate between two different colours or transform from colourless to coloured, and vice versa, due to some external stimulus or change in the environment.<sup>2</sup> This is not to be confused with dichroism which refers to a compound that appear a different colour under orthogonally polarised light. In this work, two systems exhibiting dichromism is studied of which one is an example of vapochromism and the other of photochromism from two different types of compounds, Schiff bases and diarylethenes.

### 1.4 Schiff bases and trianglimines

Trianglimine is a common name given to a group of compounds of which the basic backbone is a ring structure consisting of three cyclohexyl and three phenyl rings connected in an alternating fashion by imine groups as illustrated in Figure 1-1. These compounds have been used previously as inclusion compounds in the field of supramolecular chemistry.<sup>26-28</sup>

Schiff bases are a group of imine-containing compounds of the form  $R_2C=NR'$  ( $R' \neq H$ ) often considered synonymous to azomethines,  $HRC=NR'$  ( $R' \neq H$ ).<sup>29</sup> These compounds are used extensively within coordination chemistry as mono-, bi- and polydentate ligands.<sup>30-32</sup> Many Schiff bases can undergo an enolimine-ketoenamine transformation (Figure 1-2) owing to an intramolecular proton transfer.<sup>33-37</sup> These compounds are found in biological processes<sup>38</sup> and also have application in

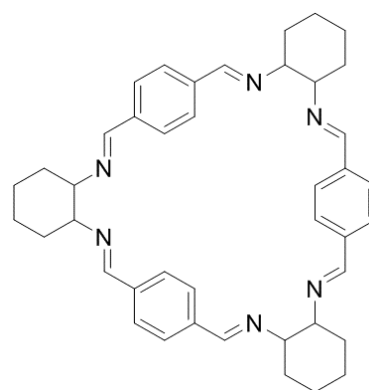


Figure 1-1: Trianglimine. Additions can be made onto the phenyl or cyclohexyl rings as well as onto the nitrogen atoms.

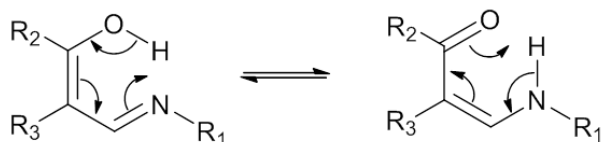


Figure 1-2: Enolimine-ketoenamine tautomerism ( $R_1, R_2, R_3 = \text{alkene, alkyl, aryl}$ ).

areas such as medicine<sup>39</sup> and chemical sensing.<sup>40</sup> The enol and keto forms have different UV-Vis absorption spectra resulting in these compounds exhibiting chromic phenomena. The enolimine-ketoenamine transformation shown in Figure 1-2 has been seen to occur as an iono-, solvato-, thermo-, or photochromic process.<sup>34</sup> In this work, a Schiff-base-containing trianglimine compound that undergoes an enolimine-ketoenamine tautomerisation in the crystalline phase is studied. The transformation is shown to occur as a result of a combination of a sorptiochromic and a hydrochromic process, which are both subcategories of solvatochromism.<sup>2</sup>

## 1.5 Diarylethenes

1,2-diarylethenes are a group of compounds of the form  $\text{Ar}-\text{C}=\text{C}-\text{Ar}$ .<sup>41,42</sup> The simplest example of a 1,2-diarylethene is stilbene, which is a well-studied compound and known to undergo photoisomerisation upon irradiation with UV light to produce dihydrophenanthrene (Figure 1-3). Dihydrophenanthrene can be converted back to stilbene via irradiation with visible light. This is an example of dichromism as there are two forms, open and closed, which have different UV-Vis absorption spectra and thus different colours. Dihydrophenanthrene is, however, an unstable product and will revert back to stilbene within 2 minutes. Dihydrophenanthrene can also react with oxygen in air to undergo a hydrogen-elimination reaction resulting in phenanthrene.

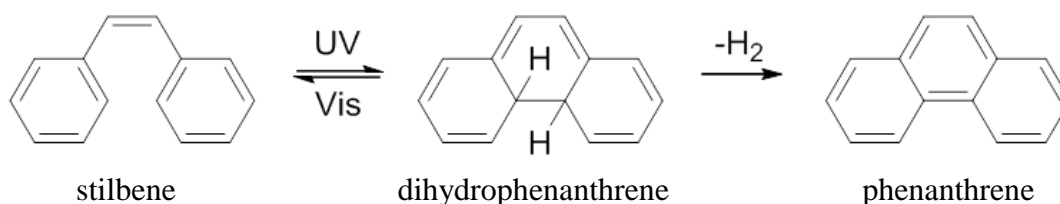


Figure 1-3: Stilbene undergoes a ring-closure reaction upon irradiation with UV light. Dihydrophenanthrene can convert back to stilbene under irradiation with normal light or convert to phenanthrene in air via a hydrogen-elimination reaction.

Kellogg et al.<sup>43</sup> found that the lifetime of the closed form could be increased to periods of 12 to 15 hours by replacing the phenyl groups with thiophene rings (Figure 1-4). The reason for this was later explained by a computational study done by Irie et al.<sup>44</sup> The very high aromatic stabilisation energy offered by the phenyl rings in stilbene makes it much more

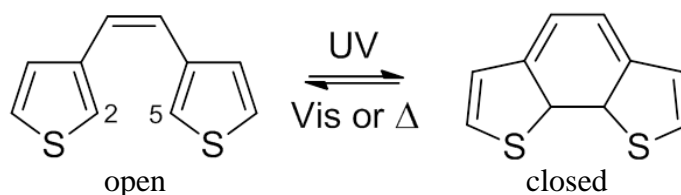


Figure 1-4: Dithienylethene undergoes a ring-closure under UV light and a ring-opening under visible light.

thermodynamically preferred than dihydrophenanthrene. By introducing a group with less aromatic stabilisation energy, such as thienyl, furyl or pyrrolyl, the difference in energy between the open and closed forms is decreased, making both forms thermodynamically stable. By substituting with a methyl group at the 2 and 5 positions of the thienyl the H<sub>2</sub>-elimination reaction is further suppressed, thus stabilising the closed form. This is the design principle behind diarylethenes.

The finding by Kellogg sparked the design of many more diarylethenes.<sup>45</sup> These compounds have the potential to be used in memory devices and molecular switches.<sup>25,46</sup> There are, however, some requirements for such applications to be realised, including thermal stability of both the open and closed forms, resistance to degradation, high sensitivity and rapid response to external stimulus. The diarylethenes must also be able to reversibly undergo ring-closure and ring-opening in the solid or crystalline state. In the past few years good progress has been made in identifying diarylethenes that perform well in all of these categories.<sup>46–49</sup>

In this work the polymorphism and photochromism of a new diarylethene will be studied. New insight will be provided into the reason why a certain packing arrangement was adopted in different solvents and conditions. Further insight into the mechanism behind the photochromic behaviour of the diarylethene will be provided.

## 1.6 Aims, objectives and outline

The aim of this study is to gain insight into the origins of colour changes in different materials. The first objective (described in Chapter 4) is to explain the dichromic behaviour of a crystal from a schiff-base-containing trianglimine compound, using computational methods and a model compound. These crystals appear yellow at a humidity below 55% and red at a humidity higher than 55% and thus display a form of solvatochromism. The way in which water interacts with the system, resulting in a spontaneous colour change, will be explained.

The next objective (described in Chapter 5) is to study the polymorphism of a new photochromic diarylethene compound. This is done with the aid of various analytical techniques as described in the materials and methods section. The results will be compared to a study done on a similar compound, by Kobatake and Kitagawa,<sup>50</sup> illustrating how a small change in the molecular structure affects the packing in the solid state.

The last objective (described in Chapter 6) is to provide a fundamental explanation for the diarylethene photoisomerisation reaction. This will be done using a method that involves scanning all the major parameter differences, between the ring-closed and ring-opened forms, followed by the calculation of the excited state potential energy surface map. This method will then be applied to a range of model compounds to illustrate the effect that various structural modifications will have on the diarylethene ring-closure or ring-opening reaction.

The theoretical background to the computational methods used is presented in Chapter 2 while the materials and methods are presented in Chapters 3. The results of this work are thus presented in three parts, Chapters 4 to 6, of which each contains individual introduction, aims and objectives, and methods sections that will provide more background, relevant to the specific topic discussed in the chapter. Each chapter will be discussed and summarised individually but jointly concluded in Chapter 7. Future work will also be discussed in this final chapter, followed by a references section.

## Chapter 2: Theoretical Background

All theoretical calculations are fundamentally dependent on the quantum mechanical constructs developed early in the 20<sup>th</sup> century and thus a brief background is given as to the origin of these theories and how they are implemented to solve problems in chemistry. Although initially done by hand, ultimately for the field of theoretical chemistry to advance, theories of quantum chemistry needed to be mathematically incorporated into computer programs that allow the automation of calculations. Hence the term theoretical chemistry and computational chemistry became inseparable.

In this chapter a brief discussion is given on the theoretical methods used in this work. Although many other books and resources exist on the topic of quantum chemistry and theoretical chemistry, the books by Ullrich,<sup>51</sup> Jensen<sup>22</sup> and Koch and Holthausen<sup>52</sup> were used extensively but not exclusively for this review. The field of quantum chemistry is truly vast and so reference will only be made to concepts relevant to this work.

### 2.1 Quantum mechanics

By the end of the 19<sup>th</sup> century new developments in experimental physics demonstrated the inadequacy of classical physics, since phenomena were observed that could not be explained using the laws of classical mechanics.<sup>53</sup> The complication lay in the fact that light and electrons seemed to possess a wave-particle duality, which was an unknown concept at that time. This was resolved in 1926 and 1927 with a new theory called quantum mechanics, which accurately describes the behaviour of photons and electrons. This theory asserts that for certain experiments the outcome is fundamentally unpredictable and one can only calculate the probability of certain outcomes. Quantum mechanics was later used to solve real problems in chemistry, based on this new understanding of particles in nature.<sup>54</sup>

As stated by Jensen, one of the four features necessary for describing a system is the position and velocity of the particles.<sup>22</sup> For an atom or molecule, this would mean that the positions and velocities of the nuclei and electrons need to be determined in order to describe the system. The positions and velocities of the nuclei can, to a certain extent, easily be determined since they behave in a classical manner. The positions and velocities of the electrons, however, have to be defined in a probabilistic manner, since they do not follow the classical laws. Therefore quantum mechanics is essential for describing the electrons in a molecular system; this is done using a wave function that replaces the classical concept of a trajectory.<sup>55</sup>

### 2.1.1 The Time-Independent Schrödinger Equation

The time-independent Schrödinger equation was proposed by Erwin Schrödinger in 1926 as a way of determining the wave function of any molecular system.<sup>55</sup>

$$\hat{H}\psi_i(\vec{x}_1, \vec{x}_2, \dots, \vec{x}_N, \vec{R}_1, \vec{R}_2, \dots, \vec{R}_M) = E_i\psi_i(\vec{x}_1, \vec{x}_2, \dots, \vec{x}_N, \vec{R}_1, \vec{R}_2, \dots, \vec{R}_M) \quad (2.1)$$

The  $M$ -nuclei and  $N$ -electron wave function  $\psi_i(\vec{x}_1, \vec{x}_2, \dots, \vec{x}_N, \vec{R}_1, \vec{R}_2, \dots, \vec{R}_M)$  is the  $i^{\text{th}}$  eigenstate of the Hamiltonian operator  $\hat{H}$ , with an associated energy eigenvalue  $E_i$ . Each term  $\vec{x}_n$  represents the three spatial coordinates, denoted as  $\vec{r}_n$ , and one spin coordinate, denoted as  $s_n$ , for electron  $n$ , while each term  $\vec{R}_m$  represents the three spatial coordinates for nucleus  $m$ .

The differential operator  $\hat{H}$  represents the total energy of the system and can be divided into the kinetic and potential energy parts for the nuclei and electrons (given in atomic units):<sup>52</sup>

$$\hat{H} = \hat{T}_n + \hat{T}_e + \hat{V}_{ne} + \hat{V}_{ee} + \hat{V}_{nn} \quad (2.2)$$

$$\hat{T}_e = -\frac{1}{2} \sum_{k=1}^N \nabla_k^2, \quad \hat{T}_n = -\frac{1}{2} \sum_{A=1}^M \frac{1}{M_A} \nabla_A^2$$

$$\hat{V}_{ne} = -\sum_{k=1}^N \sum_{A=1}^M \frac{Z_A}{r_{kA}}, \quad \hat{V}_{ee} = \sum_{k=1}^N \sum_{l>1}^N \frac{1}{r_{kl}}, \quad \hat{V}_{nn} = \sum_{A=1}^M \sum_{B>A}^M \frac{Z_A Z_B}{r_{AB}}$$

The indices  $k$  and  $l$  run over the  $N$  electrons while  $A$  and  $B$  denote the  $M$  nuclei. The kinetic energy operators for the nuclei and electrons are represented by  $\hat{T}_n$  and  $\hat{T}_e$  respectively. The Laplacian operator  $\nabla_k^2$  is defined as the sum of differential operators in Cartesian coordinates

$$\nabla_k^2 = \frac{\partial}{\partial x_k^2} + \frac{\partial}{\partial y_k^2} + \frac{\partial}{\partial z_k^2} \quad (2.3)$$

and  $M_A$  equals the mass of nuclei  $A$  in multiples of the mass of an electron (which is 1 au). The potential energy operators are represented by  $\hat{V}_{ne}$ ,  $\hat{V}_{ee}$  and  $\hat{V}_{nn}$ , which are the attractive electrostatic interaction between the nuclei and electrons, the repulsive potential energy between electrons and the repulsive potential energy between nuclei, respectively. Lastly the distance between two particles  $p$  and  $q$  is represented by  $r_{pq} = |\vec{r}_p - \vec{r}_q|$  and  $Z_m$  represents the atomic number or nuclear charge of nucleus  $m$ .

### 2.1.2 The Born-Oppenheimer approximation

The Schrödinger equation can be simplified further by making an approximation famously called the *Born-Oppenheimer*, or clamped-nuclei, approximation. This takes advantage of the large difference in mass between electrons and nuclei. The mass of a proton ( $^1\text{H}$ ) is 1836.15 au compared to the 1 au of an electron, which means that the nucleus within an atom moves much more slowly than the electrons. Consequently, it is a reasonable approximation to assume the nuclei are fixed, while the electrons are moving in the potential field produced by the nuclei. The kinetic energy of the nuclei now becomes zero while the nucleus-nucleus repulsion potential energy is reduced to a constant and thus the Hamiltonian from equation (2.2) is reduced to the electronic Hamiltonian:

$$\hat{H}_{elec} = \hat{T}_e + \hat{V}_{ne} + \hat{V}_{ee} \quad (2.4)$$

$$\hat{T}_e = -\frac{1}{2} \sum_{k=1}^N \nabla_k^2, \quad \hat{V}_{ne} = - \sum_{k=1}^N \sum_{A=1}^M \frac{Z_A}{r_{kA}}, \quad \hat{V}_{ee} = \sum_{k=1}^N \sum_{l>1}^N \frac{1}{r_{kl}}$$

Upon solving the Schrödinger equation for  $\hat{H}_{elec}$  one now obtains the electronic wave function  $\psi_{elec} = \psi_j$  and the electronic energy  $E_{elec} = E_j$ . In fact, the Schrödinger equation can now also be reduced to a wave function that is only dependent on the electron coordinates, with the nuclear coordinates only entering parametrically:

$$\hat{H}_{elec} \psi_j(\vec{x}_1, \vec{x}_2, \dots, \vec{x}_N) = E_j \psi_j(\vec{x}_1, \vec{x}_2, \dots, \vec{x}_N) \quad (2.5)$$

The total energy  $E_{tot}$  is now the sum of the electronic energy  $E_{elec}$  and the nucleus-nucleus repulsion potential energy  $\hat{V}_{nn} = E_{nuc}$  from equation (2.2):

$$\hat{V}_{nn} = E_{nuc} = \sum_{A=1}^M \sum_{B>A}^M \frac{Z_A Z_B}{R_{AB}}$$

$$E_{tot} = E_{elec} + E_{nuc} \quad (2.6)$$

The term  $\hat{V}$  from equation (2.4), which is the attractive potential that the nuclei exert on the electrons, is often denoted as the external potential. As will be shown in a later section, time-dependent factors are introduced via this term. For simplicity's sake, from now on only the electronic part will be considered, thus 'elec' is dropped from equation (2.5).

### 2.1.3 Variational principle

The first step into solving the Schrödinger equation (2.5) is to set up the Hamiltonian for a specific system. This is done by substituting the parameters for a given system into the different parts of the Hamiltonian (2.4). Secondly, the eigenfunctions  $\psi_j$  and their corresponding eigenvalues  $E_j$  need to be determined for the given Hamiltonian. Unfortunately, the Schrödinger equation can only be solved analytically for systems with two interacting particles while for larger systems there is no exact strategy for solving the equation.<sup>22</sup> There is, however, a way of approaching the ground state wave function  $\psi_0$  in a systematic, step-by-step fashion and this is where the *variational principle* is of great importance within quantum chemistry.<sup>52</sup>

For a system in the  $j^{\text{th}}$  many-body eigenstate, the expectation value  $O_j$  associated with a physical observable  $\hat{O}$  can be calculated using any normalised wave function  $\psi_{\text{trial}}$  as follows, using Dirac's bra-ket notation for integrals:<sup>52</sup>

$$O_j = \int \dots \int \psi_{\text{trial}}^* \hat{O} \psi_{\text{trial}} d\vec{x}_1, d\vec{x}_2, \dots, d\vec{x}_N \equiv \langle \psi_{\text{trial}} | \hat{O} | \psi_{\text{trial}} \rangle \quad (2.7)$$

The variational principle now states that by applying the Hamiltonian operator  $\hat{H}$ , the energy  $E_{\text{trial}}$  calculated for any guessed wave function  $\psi_{\text{trial}}$  will always be higher than the energy  $E_0$  calculated for the true ground state wave function  $\psi_0$ ,

$$\langle \psi_{\text{trial}} | \hat{H} | \psi_{\text{trial}} \rangle = E_{\text{trial}} \geq E_0 = \langle \psi_0 | \hat{H} | \psi_0 \rangle \quad (2.8)$$

with  $E_{\text{trial}} = E_0$  only in the case where  $\psi_{\text{trial}} = \psi_0$ .<sup>52</sup>

Therefore, without making approximations the only current strategy to finding the true ground state wave function  $\psi_0$  is by searching through all acceptable N-electron wave functions to find the wave function that gives the lowest energy, which is then denoted  $\psi_0$ . This is obviously not possible, but the variational principle can still be applied to subsets and as long as such a subset still contains the ground state wave function, the variational principle will allow  $\psi_0$  to be found. A subset is made by making an approximation to solving the Schrödinger equation and thus this has become the ultimate goal in quantum chemistry. Many schemes have been devised to do just that, including Hartree-Fock (HF) theory, configuration interaction (CI) expansions and quantum Monte Carlo approaches to mention a few. In the next section we will consider the Hartree-Fock approximation.

### 2.1.4 The Hartree-Fock Approximation

Although the Hartree-Fock method was not directly applied in this study it will be discussed here, as it is considered the cornerstone of most wave function-based quantum chemical methods and will aid in the understanding of density functional theory, which will be discussed later in this chapter.<sup>52</sup>

As previously mentioned it is impossible to search through all acceptable N-electron wave functions. Thus a subset needs to be defined that is practically manageable yet offers a reasonable approximation to the exact wave function. In the Hartree-Fock scheme the N-electron wave function is approximated by an antisymmetrised product of N one-electron wave functions, which is usually referred to as the Slater determinant:

$$\psi_0 \approx \phi_{SD} = \frac{1}{\sqrt{N!}} \begin{vmatrix} \psi_1(\vec{x}_1) & \psi_2(\vec{x}_1) & \cdots & \psi_N(\vec{x}_1) \\ \psi_1(\vec{x}_2) & \psi_2(\vec{x}_2) & \cdots & \psi_N(\vec{x}_2) \\ \vdots & \vdots & \ddots & \vdots \\ \psi_1(\vec{x}_N) & \psi_2(\vec{x}_N) & \cdots & \psi_N(\vec{x}_N) \end{vmatrix} \quad (2.9)$$

This can be written in a short-hand manner giving only the diagonal elements:

$$\phi_{SD} = \frac{1}{\sqrt{N!}} \det\{\psi_1(\vec{x}_1) \ \psi_2(\vec{x}_2) \ \dots \ \psi_N(\vec{x}_N)\} \quad (2.10)$$

The one-electron functions  $\psi_i(\vec{x}_i)$  are denoted spin orbitals, and composed of two parts, the spatial orbital  $\phi_i(\vec{r})$  and either of the two spin functions,  $\alpha(s)$  or  $\beta(s)$ :

$$\psi(\vec{x}) = \phi_i(\vec{r}) \alpha(s) \text{ or } \psi(\vec{x}) = \phi_i(\vec{r}) \beta(s) \quad (2.11)$$

The spin functions are orthonormal, in other words  $\langle \alpha | \alpha \rangle = \langle \beta | \beta \rangle = 1$  and  $\langle \alpha | \beta \rangle = \langle \beta | \alpha \rangle = 0$  and for computational convenience the spin orbitals are also usually chosen to be orthonormal:

$$\langle \psi_i | \psi_j \rangle = \begin{cases} 1, & \text{for } i = j \\ 0, & \text{for } i \neq j \end{cases}, \delta_{ij} \quad (2.12)$$

Now that the form of the wave function has been established, the variational principle can be used to find the Slater determinant  $\phi_{SD}$ , which yields the lowest energy, using the self-consistent (SCF) field procedure. This is an iterative method whereby an approximate Hamiltonian is used to solve the Schrödinger equation in order to obtain a better set of orbitals. These are then used to solve the Schrödinger equation over and over until the result converges.

$$E_{HF} = \min_{\phi_{SD} \rightarrow N} E[\phi_{SD}] \quad (2.13)$$

The energy is calculated using the Hamiltonian with the appropriate Slater determinant  $\phi_{SD}$ :

$$E_{HF} = \langle \phi_{SD} | \hat{H} | \phi_{SD} \rangle \quad (2.14)$$

The cut-off criteria of the program used to perform the SCF procedure will determine how close the final Slater determinant  $\phi_{SD}$  is to the true ground state wave function  $\psi_0$ .

### 2.1.5 The Time-Dependent Schrödinger Equation

Time-dependence is introduced to the system by making the external potential subject to change over time. The Schrödinger equation now becomes

$$\hat{H}(t)\psi(\vec{x}_1, \dots, \vec{x}_N, t) = i \frac{\partial}{\partial t} \psi(\vec{x}_1, \dots, \vec{x}_N, t) \quad (2.15)$$

with the Hamiltonian and the wave function now having time as a parameter.<sup>51</sup> In this case, generally speaking the wave function is not necessarily an eigenfunction of the Hamiltonian, and thus on the right-hand side one cannot simply write the energy  $E$  as an eigenvalue.<sup>56</sup> The initial state or wave function  $\psi(t_0) \equiv \psi_0$  is propagated over a time interval  $[t_0, t_1]$ , thus from an initial time  $t_0$  to some time in the future  $t_1$ . The time-dependent Hamiltonian of the  $N$ -particle system is now given as

$$\hat{H}(t) = \hat{T}_e + \hat{V}_{ne} + \hat{V}_{ee} \quad (2.16)$$

$$\hat{T}_e = -\frac{1}{2} \sum_{k=1}^N \nabla_k^2, \quad \hat{V}_{ne}(t) = -\sum_{k=1}^N v(\vec{r}_k, t), \quad \hat{V}_{ee} = \sum_{k=1}^N \sum_{k>1}^N \frac{1}{r_{kl}}$$

with the Born-Oppenheimer approximation already introduced to the system.<sup>51</sup> The electron kinetic-energy operator  $\hat{T}_e$  and the electron-electron interaction operator  $\hat{V}_{ee}$  stay exactly the same as in the time-independent case. The external potential is, however, now dependent on time and can be divided into two parts as follows:

$$v(\mathbf{r}, t) = v_0(\mathbf{r}) + v_1(\mathbf{r}, t)\theta(t - t_0) \quad (2.17)$$

Considering the right-hand side of equation (2.17) the first part  $v_0(\mathbf{r})$  is the external potential for the system in its ground state. This is the potential produced by the nuclei but can also include other constant external potential fields such as a magnetic or electric field. The time-dependent part of the external potential  $v_1(\mathbf{r}, t)$  is introduced at time  $t_0$  via a step function  $\theta(t - t_0)$ , which is equal to 1 for positive values, but 0 for negative values.

### 2.1.5.1 Time evolution operators

It is easier to understand the behaviour of the system by writing the Schrödinger equation in terms of a time evolution operator:<sup>51</sup>

$$\psi(t) = \hat{U}(t, t_0)\psi_0 \quad (2.18)$$

The time evolution operator  $\hat{U}(t, t_0)$  starts acting on the initial ground state wave function  $\psi_0$  at some time  $t_0$  resulting in the evolution of  $\psi_0$  into  $\psi(t)$  at some time after  $t_0$ . The time evolution operator can be written in terms of the Hamiltonian as

$$\hat{U}(t, t_0) = \hat{T} \exp \left\{ -i \int_{t_0}^t dt' \hat{H}(t') \right\} \quad (2.19)$$

with  $\hat{T}$  as a time-ordering operator. Since the external potential (2.17) consists of time-independent and time-dependent parts so too does the Hamiltonian

$$\hat{H}(t) = \hat{H}_0 + \hat{H}_1(t) \quad (2.20)$$

with  $\hat{H}_1(t)$  describing a time-dependent perturbation, non-zero only for  $t \geq t_0$  owing to the switch-on function from equation (2.17). Replacing this expression for the Hamiltonian in equation (2.19) yields the following expression for the time-evolution operator:

$$\hat{U}(t, t_0) = e^{-i\hat{H}_0(t-t_0)} \hat{U}_1(t, t_0) \quad (2.21)$$

Consider now a quantum mechanical observable  $\hat{a}$  (representing a physically measurable property) with a ground state expectation value that is given by

$$a_0 = \langle \psi_0 | \hat{a} | \psi_0 \rangle \quad (2.22)$$

with  $\psi_0$  representing the ground state many body wave function before time  $t_0$  associated with the static Hamiltonian  $\hat{H}_0$ . Assuming now that the system has reached time  $t_0$  the time evolution operator is switched on, acting on  $\psi_0$  resulting in  $\psi(t)$ . The expectation value now becomes time-dependent:

$$a(t) = \langle \psi(t) | \hat{a} | \psi(t) \rangle \quad (2.23)$$

The difference between the time-dependent expectation value  $a(t)$  and its initial static value,  $a(t) - a_0$ , is called the *response* of  $a_0$  to the perturbation introduced by the time-dependent part of the Hamiltonian  $\hat{H}_1(t)$ .

### 2.1.6 Basis Sets

A basis set is a set of functions, consisting of vectors and coefficients that mathematically approximate the shape of the atomic orbitals (AOs) used for constructing the wave function.<sup>57</sup> Once atoms are combined to form a molecule, these functions are linearly combined to form molecular orbitals (MOs). A larger basis set (such as 6-311++G(d,p) compared to 6-31G) provides for more coefficients that can be fine-tuned to make a better approximation of the shape of the orbitals. A larger set of functions, however, requires more resources to compute.

Two types of orbitals are commonly used, Slater type orbitals (STOs) and Gaussian-type orbitals (GTOs) of the form:<sup>22</sup>

$$\phi_{STO}(r, \theta, \phi) = \alpha Y_{lm}(\theta, \phi) r^{n-1} e^{-\zeta r} \quad (2.24)$$

$$\phi_{GTO}(r, \theta, \phi) = \alpha Y_{lm}(\theta, \phi) r^{(2n-2-l)} e^{-\zeta r^2} \quad (2.25)$$

In two aspects GTOs are considered inferior to STOs. At the nucleus, which is at a distance of 0 Å, GTOs have a zero slope whereas STOs have a cusp. For this reason GTOs do not represent the proper behaviour near the nucleus. The other problem with GTOs is the fact that they fall off too rapidly far away from the nucleus and thus also don't represent the correct behaviour further away from the nucleus. In general about three times as many GTOs as STOs are necessary for reaching a given level of accuracy. In Figure 2-1 three Gaussian-type basis functions were used to approximate one Slater-type function. Despite these drawbacks GTOs are still much more computationally efficient since the factor  $r$  in the exponent of STOs requires taking a square root ( $r = \sqrt{x^2 + y^2 + z^2}$ ) which takes very long to compute and so GTOs are still used almost universally for electronic structure calculations.

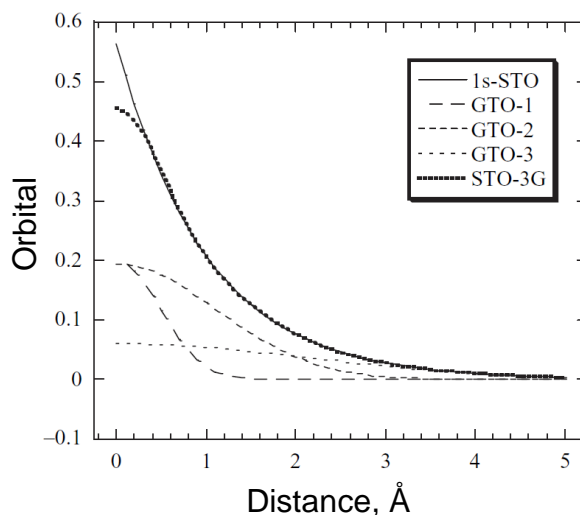


Figure 2-1: A Slater type orbital is modelled with a linear combination of three Gaussian-type Orbitals.<sup>22</sup>

## 2.2 Density Functional Theory (DFT)

Once the wave function for a specific system has been determined, any information required can be obtained by applying an associated operator  $\hat{O}$  (for a specific property) to the ground state wave function  $\psi_0$  in order to obtain the expectation value  $O_j$ .<sup>51</sup> Thus we want to address the question: if the wave function contains all the information we would ever need then why the necessity for density functional methods? The situation was summarised in a concise manner by Dirac in 1929:<sup>51</sup>

“The fundamental laws necessary for the mathematical treatment of a large part of physics and the whole of chemistry are thus completely known and the difficulty lies only in the fact that application of these laws leads to equations that are too complex to be solved.”

Wave function methods counter an “exponential wall” and for an increasing number of particles it simply becomes impractical to even store a wave function of that size. Kohn (1999) stated that the many-electron wave function  $\psi_j(\vec{x}_1, \vec{x}_2, \dots, \vec{x}_N)$  for a system of  $N$  electrons is not a legitimate scientific concept when  $N \geq 10^3$ .<sup>51</sup>

A different approach would be to solve for specific properties and not for the whole wave function. This makes practical sense, since the wave function contains much more information than we would ever need and in general a chemist is only interested in properties that can be characterised by a single number or a few variables, such as energies and single-particle probability densities. In principle, DFT allows us to obtain all properties of a many-body system exactly without solving the many-body Schrödinger equation. This statement is proven in the Hohenberg-Kohn theorems.

### 2.2.1 Electron density and the Hohenberg-Kohn Theorems

Density Functional Theory was born in 1964 when a paper by Hohenberg and Kohn proved the basic theorems that DFT is based on.<sup>52</sup> When considering a system of  $N$  particles in a finite region of space, governed by the many-body Hamiltonian, the single-particle probability density of the electronic ground state is given by

$$n_0(\vec{r}) = N \int \dots \int |\psi(\vec{x}_1, \vec{x}_2, \dots, \vec{x}_N)|^2 d\vec{s}_1 d\vec{x}_2 \dots d\vec{x}_N \quad (2.26)$$

remembering that  $\vec{x}_N = (x_N, y_N, z_N, s_N)$ . Although the theorems will be discussed the proofs will not be explained but are fairly trivial to understand and have been adequately explained in many resources.

### 2.2.1.1 The First Hohenberg-Kohn Theorem: Proof of Existence

The first Hohenberg-Kohn theorem states that there is a one-to-one correspondence between the external potential  $v(\vec{r})$  and the ground state density  $n_0(\vec{r})$  or, differently put, the external potential is a unique functional of the ground state density  $v[n_0(\vec{r})]$ .<sup>52</sup> This can be illustrated schematically as follows:

$$\begin{aligned} v(\vec{r}) \Rightarrow \hat{H} \Rightarrow \psi_0 \Rightarrow n_0(\vec{r}) \\ v'(\vec{r}) \Rightarrow \hat{H}' \Rightarrow \psi'_0 \Rightarrow n'_0(\vec{r}) \end{aligned} \quad n_0(\vec{r}) \neq n'_0(\vec{r}) \quad (2.27)$$

In other words two potentials that differ by more than a constant, such as  $v(\vec{r}) \neq v'(\vec{r}) + c$ , will always produce two different ground state wave functions, where  $\psi_0$  and  $\psi'_0$  differ by more than a trivial phase factor  $e^{-ic}$ , which will always produce two different ground state densities,  $n_0(\vec{r})$  and  $n'_0(\vec{r})$ .

Now since the kinetic and electron-electron interaction operators  $\hat{T}_e$  and  $\hat{V}_{ee}$  are fixed, this implies that the Hamiltonian is also a functional of the electron density i.e.  $\hat{H}[n_0(\vec{r})]$  and thus not only the ground state  $\psi_0$  but all the eigenstates become functionals of the electron density  $n_0(\vec{r})$ . This leads us to the conclusion that all the ground-state and excited-state properties are dependent on the ground-state particle density  $n_0(\vec{r})$ .

Using the same terminology as was used in section 2.1.2 we can say that the electron density contains the information about the parameters  $N$ ,  $r_{kA}$  and  $Z_A$  that ultimately determines the energy of the system, which can be summarised schematically:

$$n_0 \Rightarrow \{N, r_{kA}, Z_A\} \Rightarrow \hat{H} \Rightarrow \psi_0 \Rightarrow E_0 \quad (2.28)$$

Since the complete ground-state energy is a functional of the ground-state electron density the individual parts must also be, and so we can write

$$E_0[n_0] = T_e[n_0] + E_{ne}[n_0] + E_{ee}[n_0] \quad (2.29)$$

which can be divided into the parts that are dependent on the system and the parts that are universal or independent of  $N$ ,  $r_{kA}$  and  $Z_A$ :

$$E_0[n_0] = \underbrace{\int n_0(\vec{r})V_{ne}d\vec{r}}_{\text{system dependent}} + \underbrace{T_e[n_0] + E_{ee}[n_0]}_{\text{universally valid}} \quad (2.30)$$

with  $E_{ne} = \int n_0(\vec{r})V_{ne}d\vec{r}$ . By collecting the independent parts into a new quantity we now arrive at what is called the Hohenberg-Kohn functional  $F_{HK}[n_0]$ :

$$E_0[n_0] = \int n_0(\vec{r})V_{ne}d\vec{r} + F_{\text{HK}}[n_0] \quad (2.31)$$

$$F_{\text{HK}}[n_0] = T_e[n_0] + E_{ee}[n_0] = \langle \Psi_0 | \hat{T}_e + \hat{V}_{ee} | \Psi_0 \rangle \quad (2.32)$$

The functional  $F_{\text{HK}}[n_0]$  contains the functional for the kinetic energy  $T_e$  and that for the electron-electron interaction  $E_{ee}$ . The  $F_{\text{HK}}[n_0]$  functional is often called the holy grail of density functional theory, since if it were known the Schrödinger equation would have been solved exactly. Since it is a universal functional independent of the system at hand, it applies to systems of all sizes.

The explicit forms of both  $T_e$  and  $E_{ee}$  are, however, still unknown. From the latter the classical Coulomb part  $J[\rho]$  can at least be extracted since it is known

$$E_{ee}[n_0] = J[n_0] + E_{nucl}[n_0] \quad (2.33)$$

and thus

$$F_{\text{HK}}[n_0] = T_e[n_0] + J[n_0] + E_{nucl}[n_0] \quad (2.34)$$

where  $E_{nucl}$  is the non-classical contribution to the electron-electron interaction containing. Therefore finding the explicit expression of the functionals  $T_e[n_0]$  and  $E_{nucl}[n_0]$  has become the major challenge in density functional theory.

### 2.2.1.2 The Second Hohenberg-Kohn Theorem: Variational Principle

The second theorem from Hohenberg and Kohn states that the universal functional  $F[n]$ , responsible for the ground state energy of the system, will deliver the lowest energy if and only if the input density is in fact the ground state density  $n_0$ .<sup>52</sup> This means we can apply the now well-known variational principle in this context, which can be expressed in the following manner:

$$E_0 \leq E[n(\vec{r})] = \hat{T}_e[n(\vec{r})] + E_{ne}[n(\vec{r})] + E_{ee}[n(\vec{r})] \quad (2.35)$$

For any trial density  $n(\vec{r})$  the energy obtained from equation (2.35) will be higher than the true ground state energy  $E_0$  with  $E[n(\vec{r})] = E_0$  only when  $n(\vec{r}) = n_0$ . These two theorems form the foundation on which all density functional theory methods are built. In the next section we will discuss how these theorems can be put to work via the Kohn-Sham approach, which allows us to calculate densities without solving the full many-body Schrödinger equation.

## 2.2.2 The Kohn-Sham approach

In order to further simplify the Hohenberg-Kohn functional  $F_{\text{HK}}$  (2.32), Kohn and Sham suggested the introduction of a non-interacting reference system, which gives the same density as the true system, built from a set of one-electron orbitals. The kinetic energy of the non-interacting system is calculated as

$$T_S = -\frac{1}{2} \sum_i^N \langle \psi_i | \nabla^2 | \psi_i \rangle \quad (2.36)$$

Since the kinetic energy for the non-interacting system is not equal to the true kinetic energy,  $T_S \neq T_e$ , Kohn and Sham introduced the following separation of the functional  $F[n(\vec{r})]$

$$F[n(\vec{r})] = T_S[n(\vec{r})] + J[n(\vec{r})] + E_{\text{xc}}[n(\vec{r})] \quad (2.37)$$

with  $E_{\text{xc}}$  as the so-called exchange-correlation energy and defined in the following manner:

$$E_{\text{xc}}[n] = (T_e[n] - T_S[n]) + (E_{ee}[n] - J[n]) = T_C[n] + E_{\text{nucl}}[n] \quad (2.38)$$

and thus from equation (2.31) the total DFT energy can be written as

$$E_{\text{DFT}}[n] = T_S[n] + E_{ne}[n] + J[n] + E_{\text{xc}}[n] \quad (2.39)$$

Thus the major part of the energy can to be calculated exactly with only a small part that needs to be estimated using the so-called exchange-correlation energy  $E_{\text{xc}}$ . Unlike the Hartree-Fock approach for which an approximation is introduced from the start, the Kohn-Sham approach in DFT is, in principle, exact, with the approximation only entering when having to decide on an explicit description for the exchange-correlation potential energy:

$$\begin{aligned} E[n(\vec{r})] &= T_S[n(\vec{r})] + J[n(\vec{r})] + E_{ne}[n(\vec{r})] + E_{\text{xc}}[n(\vec{r})] \\ &= -\frac{1}{2} \sum_i^N \langle \psi_i | \nabla^2 | \psi_i \rangle + \frac{1}{2} \sum_i^N \sum_j^N \int \int |\psi_i(\vec{r}_1)|^2 \frac{1}{r_{12}} |\psi_j(\vec{r}_2)|^2 d\vec{r}_1 d\vec{r}_2 \\ &\quad - \sum_i^N \int \sum_A^M \frac{Z_A}{r_{1A}} |\psi_i(\vec{r}_1)|^2 d\vec{r}_1 + E_{\text{xc}}[n(\vec{r})] \end{aligned} \quad (2.40)$$

with the unknown potential defined as the functional derivative of the exchange-correlation energy with respect to the electron density:

$$V_{\text{xc}} = \frac{\delta E_{\text{xc}}}{\delta n} \quad (2.41)$$

## 2.3 Time-Dependent Density Functional Theory (TD-DFT)

Time-Dependent Density Functional Theory is used to describe and simulate dynamic processes in quantum many-body systems, especially excitation processes and the associated time evolution in the atoms, molecules or matter.<sup>51</sup> Whereas DFT is concerned with ground state phenomena, TD-DFT is applied to systems away from the ground state. Such systems are described by the time-dependent Schrödinger equation on a fundamental level. Similarly to DFT, TD-DFT provides a formally exact alternative to solving the full many-body time-dependent Schrödinger equation. The proof to this statement lies in the Runge-Gross theorem.

### 2.3.1 The Runge-Gross Theorem

For each different time-evolution operator (2.18) there is a distinct time-dependent Hamiltonian,  $\hat{H}(t) = \hat{H}_0 + \hat{H}_1(t)$ , (2.20) with a distinct external potential  $v(\mathbf{r}, t)$  acting on the initial state  $\psi_0$  to produce a distinct wave function  $\psi(t)$ . A second map now also generates a density  $n(\mathbf{r}, t)$  from  $\psi(t)$ . This can be illustrated as follows:<sup>51</sup>

$$v(\mathbf{r}, t) \xrightarrow[\text{fixed } \psi_0]{i\partial\psi/\partial t = \hat{H}(t)\psi} \psi(t) \xrightarrow{\langle \psi(t) | \hat{n} | \psi(t) \rangle} n(\mathbf{r}, t) \quad (2.42)$$

The aim of the Runge-Gross theorem is thus to prove that potentials also produce distinct densities  $n(\mathbf{r}, t)$  starting from a given initial state  $\psi_0$ . The proof will not be discussed but the theorem can be summarised as follows: Two densities  $n(\mathbf{r}, t)$  and  $n'(\mathbf{r}, t)$  evolving from an initial many-body state  $\psi_0$  under the influence of two different potentials  $v(\mathbf{r}, t)$  and  $v'(\mathbf{r}, t) \neq v(\mathbf{r}, t) + c(t)$  switched on at  $t_0$  will become different infinitesimally later than  $t_0$ , therefore implying that there is a one-to-one correspondence between densities and potentials. This is illustrated in Figure 2-2.

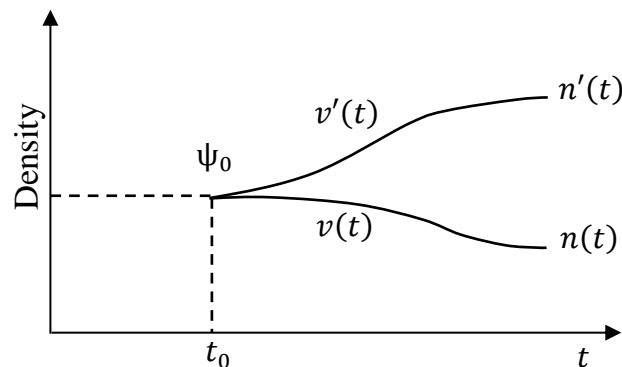


Figure 2-2: Illustration of the Runge-Gross Theorem.

Thus the time-dependent density is a unique functional of the potential, but the opposite is also true that the external potential is a unique functional of the time-dependent density. This is the fundamental existence theorem of TD-DFT and tells us, at least on a formal level, that the time-dependent density is all we need to obtain any desired observable  $\hat{a}$  of the time-dependent many-particle system. For this to be practically useful we would need a scheme for calculating the time-dependent densities without solving the full many-body Schrödinger equation. This scheme is called the Kohn-Sham approach, as was mentioned in the DFT section. The van Leeuwen theorem provides the formal proof that allows us to use a time-dependent Kohn-Sham approach to solve for densities.

### 2.3.2 The van Leeuwen Theorem

In order to make Time-dependent DFT practical we would like to use the same trick as in DFT by replacing the interacting system with an auxiliary non-interacting system that produces the same density.<sup>51</sup> The Runge-Gross theorem does not prove that we are allowed to do this and so we need to go further. The question is as follows: Can exactly the same density  $n(\mathbf{r}, t)$  be reproduced in a many-body system with different electron-electron interactions  $W$  under the influence of different external potentials starting from different initial states  $\psi_0$ ?

This is indeed possible and the proof lies in the van Leeuwen Theorem, which can be summarised as follows: For a time-dependent density  $n(\mathbf{r}, t)$  associated with a many-body system for a given particle-particle interaction  $\hat{V}_{ee}$ , external potential  $v(\mathbf{r}, t)$ , and initial state  $\psi_0$ , there exists a different many-body system featuring an interaction  $\hat{V}_{ee}'$  and a unique external potential  $v'(\mathbf{r}, t)$  that will produce the same time-dependent density. The initial state  $\psi'_0$  in this system must be chosen such that it correctly yields the given density and its time derivative at the initial time. This can also be illustrated pictorially as follows:

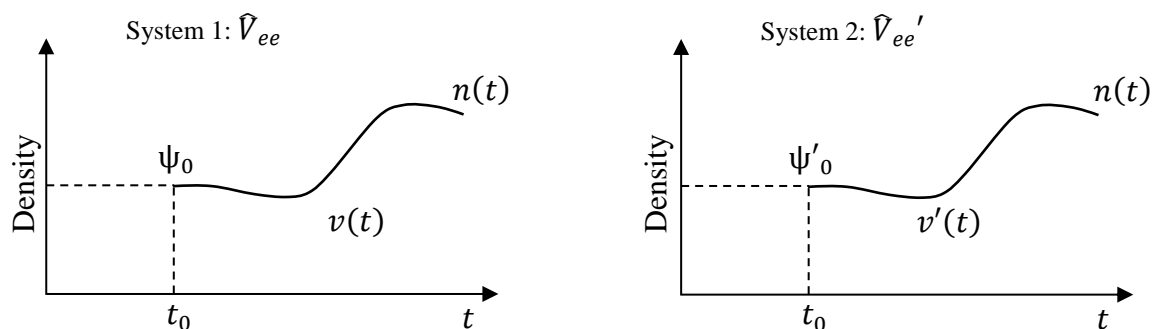


Figure 2-3: Illustration of the van Leeuwen theorem. Two different initial states can produce the same density under the influence of different external potentials.

## Chapter 3: Methodology

A wide range of experimental and computational techniques was employed during this research project, along with numerous programs and software essential to make the project feasible and process and represent data in a logical manner. The compounds that were investigated are discussed, followed by the analytical techniques and computational methods. In the final two sections analytical and computational software are discussed. A CPK colouring scheme (Table 3-1) is used throughout the project although there may be slight deviations in the tone and style. Throughout the project images of isolated molecules were created with Chemcraft<sup>58</sup> while images of periodic systems were generated with POV-Ray within the X-Seed<sup>59</sup> environment.

Table 3-1: Colouring scheme used in this study

Atom	Colour	
Hydrogen	White	
Carbon	Grey	
Nitrogen	Blue	
Oxygen	Red	
Fluorine	Lime Green	
Sulphur	Yellow	

### 3.1 Compounds investigated

Compounds investigated in this project are separated into two sections: Experimentally obtained compounds and theoretical model compounds.

#### 3.1.1 Experimentally obtained compounds

##### 3.1.1.1 Hexahydroxy-hexaazaheptacyclo-octatetraconta-pentadecaene

The compound 13,27,42,44,45,47-Hexahydroxy-3,10,17,24,31,38-hexaazaheptacyclo[38.2.2.212,15.226,29.04,9.018,23.032,37]octatetraconta-1(42),2,10,12,14,16,24,26,28,30,38,40,43,45,47-pentadecaene) falls within the class of compounds called trianglimines and thus this compound will be referred to as trianglimine **1**. Trianglimine **1** was previously synthesised by collaborators (Dr Marcin Kwit, Dr Agnieszka Janiak, Adam Mickiewicz University, Poznań, Poland). In a 1:1 ratio of ethanol and dichloromethane (DCM) the compound crystallises in the  $R3$  space group with 11 Å-wide one-dimensional channels (Figure 3-1). The crystals appear yellow at humidities lower than 55% but red at humidities higher than 55%. The crystal structures of both the yellow and red forms were determined by Dr Janiak upon visiting our laboratory. The solvatochromic behaviour of these hydrochromic crystals will be described in Chapter 4.

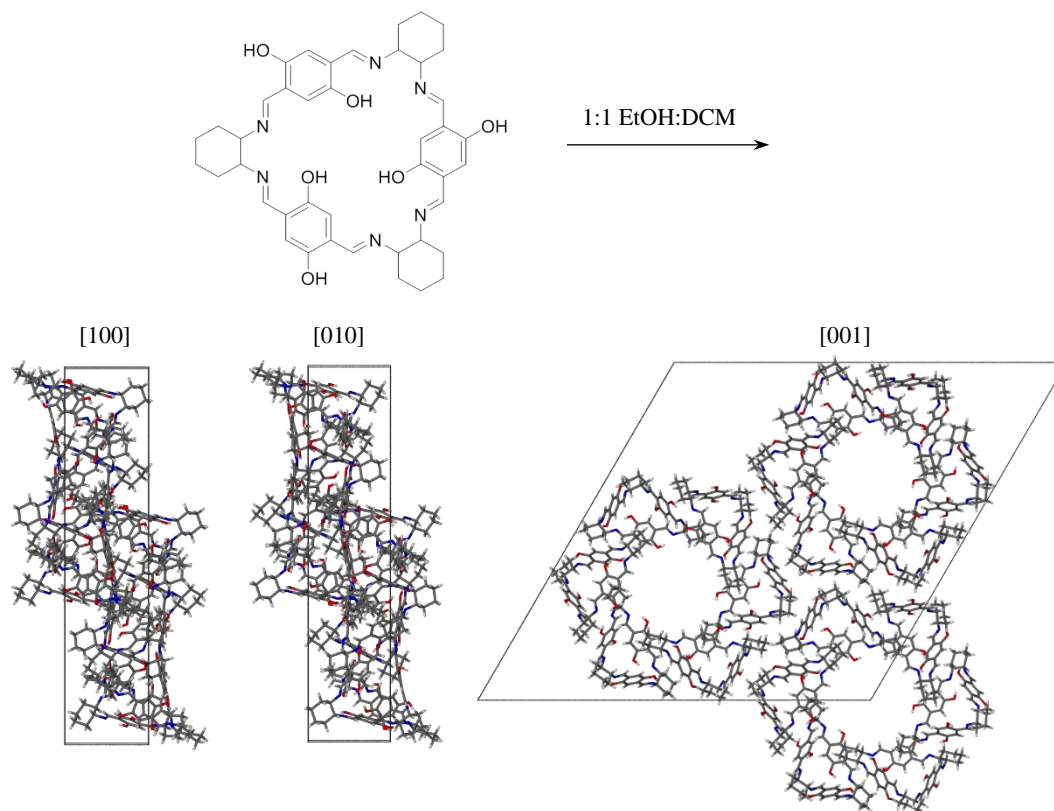


Figure 3-1: The molecular formula and crystal packing of Trianglimine **1** viewed along the [100], [010] and [001] directions.

### 3.1.1.2 Perfluorocyclopentene-diyl-bis-propylthiophene-diyl-dipyridine

The compound 4,4'-(4,4'-(perfluorocyclopent-1-ene-1,2-diyl)bis(5-propylthiophene-4,2-diyl))dipyridine (**DA-1**) is a diarylethene synthesised by a colleague from the Barbour group, Dr D. Castell.<sup>60</sup> **DA-1** exhibits photochromic behaviour as it undergoes a ring-closure reaction upon irradiation with UV light and a ring-opening reaction upon irradiation with visible light (Figure 3-2). This phenomenon occurs in solution as well as in the solid or crystalline state. In Chapter 5 a phase study, done on diarylethene **DA-1**, will be described where the ring-opened form will be referred to as **DA-1-[o]** and the ring-closed form as **DA-1-[c]**. Crystals of the thermodynamically preferred phase grow in acetone and are referred to as **DA-1-[o]- $\alpha$**  while the kinetically-preferred phase grows in hexane and is referred to as **DA-1-[o]- $\beta$**  (Figure 3-3). In Chapter 6 a theoretical study done on **DA-1**, as well as on a series of other model diarylethenes compounds, is presented.

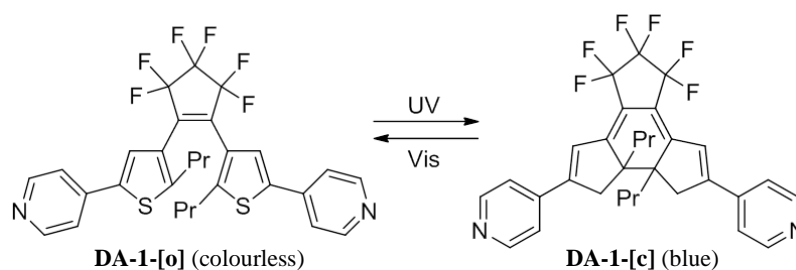


Figure 3-2: 4,4'-(4,4'-(perfluorocyclopent-1-ene-1,2-diyl)bis(5-propylthiophene-4,2-diyl))dipyridine (**DA-1-[o]**) and its ring-closed form (**DA-1-[c]**).

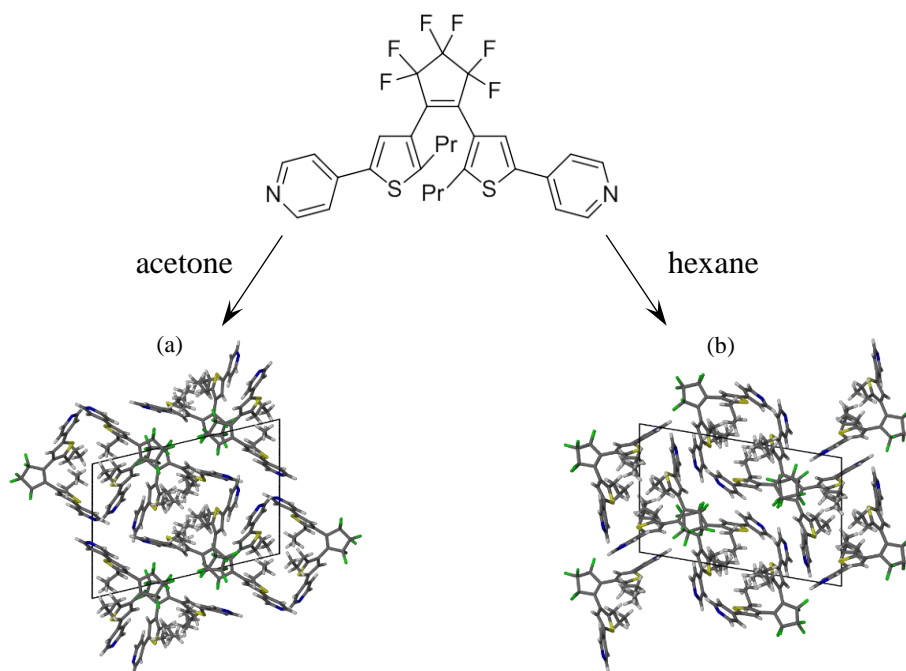


Figure 3-3: Molecular packing diagrams for the (a) **DA-1-[o]- $\alpha$**  phase and the (b) **DA-1-[o]- $\beta$**  phase

### 3.1.1.3 Perfluorocyclopentene-diyl-bis-propylthiophene-diyl-diphenyl

The compound 3,3'-(perfluorocyclopent-1-ene-1,2-diyl)bis(5-phenyl-2-propylthiophene) (**DA-10**) is a diarylethene previously studied by Kobatake and Kitagawa.<sup>50</sup> This compound is very similar to **DA-1** and also undergoes a photoisomerisation reaction upon irradiation with UV- or visible light (Figure 3-4). This compound and its crystal forms are discussed in Chapter 5 and compared to the results obtained for **DA-1-[o]**. Similar to **DA-1-[o]**, **DA-10-[o]** crystallised in two phases, **DA-10-[o]- $\alpha$**  and **DA-10-[o]- $\beta$** , from acetone and hexane respectively (Figure 3-5). The only difference between **DA-1** and **DA-10** is that **DA-1** contains pyridyl groups while **DA-10** contains phenyl groups.

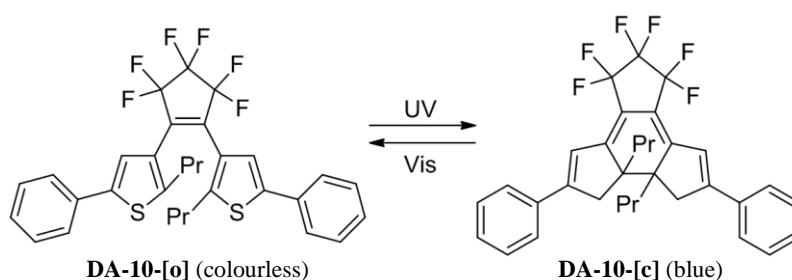


Figure 3-4: 3,3'-(perfluorocyclopent-1-ene-1,2-diyl)bis(5-phenyl-2-propylthiophene) (**DA-10-[o]**) and its ring-closed form (**DA-10-[c]**).

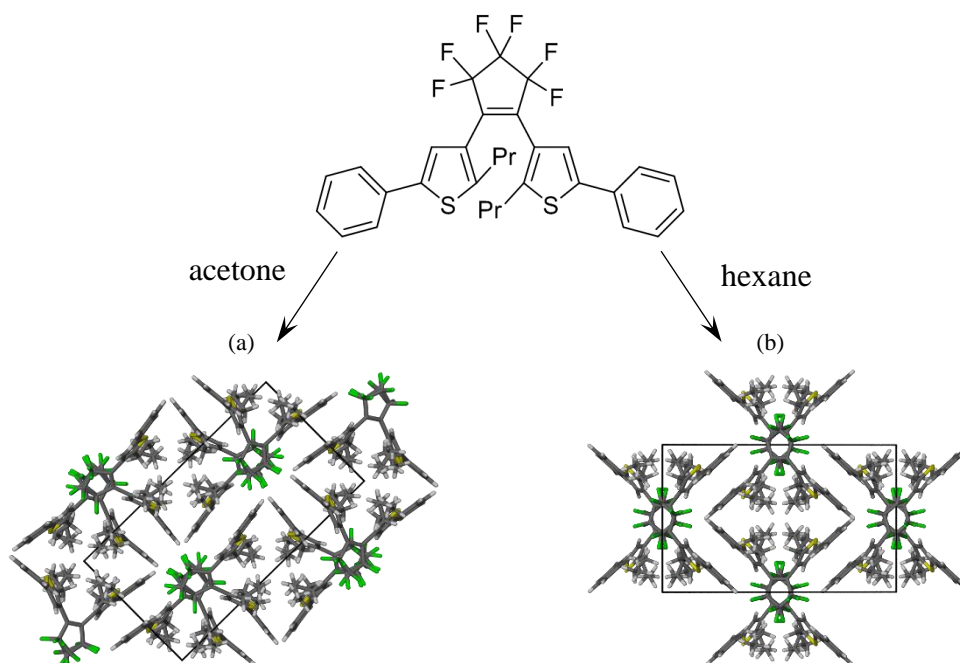


Figure 3-5: Molecular packing diagrams for the (a) **DA-10-[o]- $\alpha$**  phase and the (b) **DA-10-[o]- $\beta$**  phase

### 3.1.2 Model compounds

#### 3.1.2.1 Bis-cyclohexylimino-methyl-benzene-diol

The molecule 2,5-bis(E-(cyclohexylimino)methyl)benzene-1,4-diol (Figure 3-6) serves as a model compound for trianglimine **1**, which is described in Chapter 4. Reducing trianglimine **1** to this compound allows for the calculation of energy differences and the modelling of interactions with water, at a high level of theory, to explain the yellow-to-red colour conversion of the trianglimine **1** crystals.

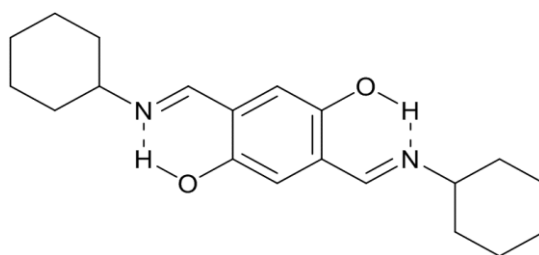


Figure 3-6: 2,5-bis(E-(cyclohexylimino)methyl)benzene-1,4-diol. The central hydroquinone part of trianglimine **1** is responsible for the visible colour of the system, i.e. it is the chromophore used as a model for this study.

#### 3.1.2.2 Diarylethenes

In Chapter 6 a series of model diarylethene compounds studied using computational methods will be described. The set of diarylethenes are labelled **DA-2** to **DA-9** as shown in Figure 3-7. In Chapter 6 **DA-2-[o]** will refer to the ring-opened form of **DA-2** and **DA-2-[c]** to the ring-closed form. Although the structures were optimised in the gas phase, their initial geometries were based on that of similar diarylethene compounds found in the CSD.

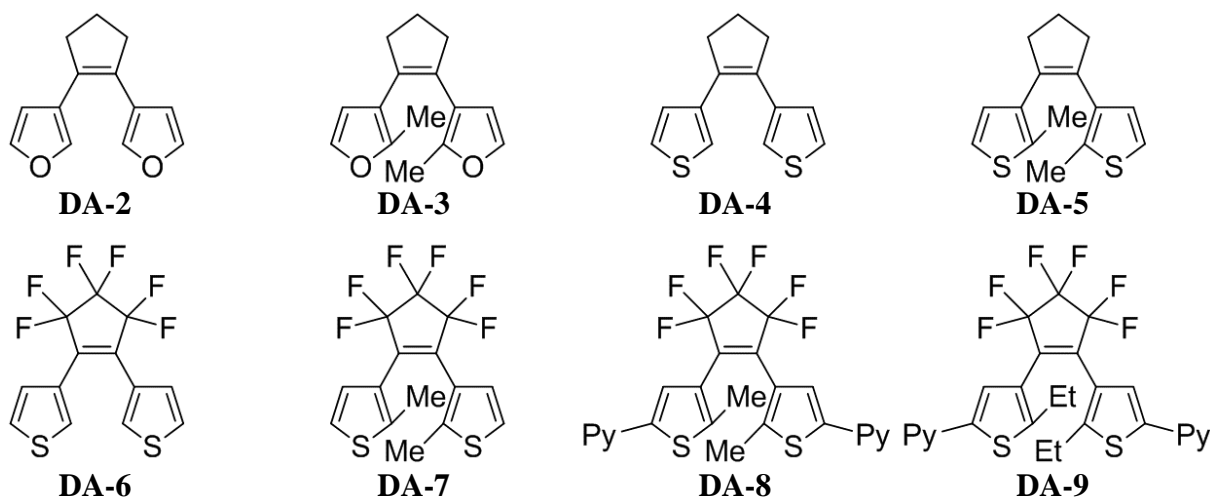


Figure 3-7: Model compounds used in computational study of diarylethenes described in Chapter 6.

## 3.2 Analytical techniques

Various analytical techniques were employed for the study described in Chapter 5. These will be discussed in this section.

### 3.2.1 Single-Crystal X-Ray Diffraction

Single-Crystal X-Ray Diffraction (SCXRD) data were collected on two different instruments. The first is a Bruker 3-circle SMART Apex II CCD single-crystal X-ray diffractometer with an INCOATEC I $\mu$ S HB microfocus tube (Mo-K $\alpha$  radiation  $\lambda = 0.71073 \text{ \AA}$ ) fitted with a multilayer monochromator and equipped with an Oxford Cryostream cooling system. Data were captured with a charge-coupled device (CCD) area detector and crystal data reduction carried out using the Apex III<sup>61</sup> software package, which is also used to operate the instrument. The second instrument is a Bruker 4 axis KAPPA D8 Venture with an INCOATEC I $\mu$ S 3.0 microfocus tube (Mo-K $\alpha$  radiation  $\lambda = 0.71073 \text{ \AA}$ ) also with a multilayer monochromator and an Oxford Cryostream cryostat supplied with liquid nitrogen. Data were captured with a Photon II CMOS detector and crystal data reduction carried out with the Apex III software package, which was also used to operate the instrument. Crystal structures were solved and refined by using the SHELX-97<sup>62</sup> program suite within the XSeed<sup>59</sup> graphical user interface. The positions of hydrogen atoms were calculated using riding models.

### 3.2.2 X-Ray Powder Diffraction

Routine Powder X-ray Diffraction (PXRD) data collections were recorded on a Bruker D2 Phase instrument equipped with a Lynxeye 1D detector and a Cu-K $\alpha$  radiation source ( $\lambda = 1.5418 \text{ \AA}$ ). For variable temperature PXRD experiments a PANalytical X'pert PRO instrument was used. This instrument is also equipped with a Cu-K $\alpha$  radiation source ( $\lambda = 1.5418 \text{ \AA}$ ) and has an X'Celerator detector. An Oxford Cryostream 700Plus cryostat was used to control the temperature with a liquid nitrogen feed.

### 3.2.3 Differential Scanning Calorimetry

Differential Scanning Calorimetry (DSC) is an analytical technique that involves measuring the heat flow of a sample as a function of the temperature. The instrument used to perform DSC experiments is a TA Instrument Q100 with a nitrogen flow of 50 ml/min. Sample sizes can vary from about 0.5 mg to 5.0 mg and are typically heated and cooled at a rate of 10 °C/min. The TA Instruments Universal Analysis program was used to analyse thermograms.

### **3.2.4 Hotstage Microscopy**

Hotstage microscopy is a setup used for visualising crystals under varying temperature. A system for controlling the temperature, including a liquid nitrogen feed for cooling, is combined with a camera and a lens that allows for clearly visualising crystals on the sub-millimetre scale. The setup is controlled by a program called Linksys.

## **3.3 Structural elucidation software**

Various programs that are adapted for studying and comparing periodic systems were used in the project and will be discussed concisely below.

### **3.3.1 Cambridge Structural Database version 5.38**

The Cambridge Crystallographic Data Centre (CCDC) is an organisation based in Cambridge, England whose main purpose is the management of the Cambridge Structural Database (CSD),<sup>63</sup> which is a collection of nearly one million small-molecule crystal structures. The CCDC also writes programs that are used for studying periodic systems, of which two were used in this dissertation, namely Mercury and Conquest.

#### **3.3.1.1 Conquest 1.19**

Conquest<sup>64</sup> is a program dedicated to searching the CSD for crystal structures using a range of search parameters, such as the publication where the crystal structure was reported, or by fragments of structures.

#### **3.3.1.2 Mercury 3.9**

The main purpose of Mercury<sup>65</sup> is the three-dimensional visualisation of crystal structures and for analysing and comparing structures obtained from a CSD search via Conquest. The program contains various tools that are helpful in this regard, such as prediction of powder patterns from crystal structures, identification of close contacts and the overlaying of structures.

### **3.3.2 XSeed 4.0**

XSeed<sup>59</sup> is a program designed for X-ray crystallographers, first published in 2001 but continually updated until the current version, XSeed 4.0. The program has two main functions: the first is to serve as a graphical user interface for solving crystal structures via the SHELX-97<sup>62</sup> program suit; the second is the production of high quality molecular graphics utilising the POV-ray program.

## 3.4 Computational software

Two programs were used for carrying out quantum chemical calculations: Gaussian was used for isolated systems, while periodic calculations were carried out using Materials Studio.

### 3.4.1 Gaussian 09

Gaussian 09<sup>23</sup> is a computational chemistry computer program that uses quantum chemistry for carrying out calculations in the prediction of physical properties of atoms, molecules and materials. The program was originally released in 1970<sup>66</sup> as Gaussian 70 by John Pople and was revolutionary for the use of Gaussian-type orbitals instead of Slater-type orbitals,<sup>67-70</sup> which resulted in a significant improvement in performance on the then limited computational capabilities of software. Gaussian Inc. continued to release new versions of the program every few years up until the version, used in this project (Gaussian 09) and the currently available version called Gaussian 16, which was released in 2016. The continuous improvements of the Gaussian program allows for ever more cutting-edge research to be performed within the domain of physical and theoretical chemistry.

### 3.4.2 Materials Studio 2016

Materials Studio<sup>71</sup> is a program used for the modelling of crystalline materials, developed by BIOVIA, a firm that specialises in software for scientific research. The program contains a range of modules or components, each serving a specific purpose for the studying of properties of materials. The graphical user interface is convenient to use, especially in the study of periodic systems, for which the program is well suited. Two modules were used for the calculation of lattice energies: Forcite for the initial optimization of hydrogen positions and then DMol<sup>3</sup> for the final optimization and lattice energy calculations<sup>72,73</sup>.

### 3.4.3 Visualisation and processing of data

Various programs and tools were used for analysing and presenting data from Gaussian log files. Chemcraft<sup>58</sup> makes analysing Gaussian logs files fairly easy by extracting the relevant data and presenting it in a graphical user interface (GUI) that is easy to interact with. Other programs that were used include Gaussview<sup>74</sup> and Avogadro.<sup>75</sup> Materials Studio already has a GUI allowing for analysing data within the program itself.

These tools are convenient for analysing single jobs, as described in Chapters 4 and 5. In Chapter 6, however, a large number of log files were produced from the scans. Making the

three-dimensional plots from these scans required generating and submission of a large number of Gaussian input files and the extraction of data from the subsequent log files. To make this process feasible some form of automation was required, which was achieved by BASH Shell scripting within the Linux terminal. Details regarding how to set up a Gaussian input file for running calculations is provided in the supplementary information. Shell scripts used for generating and extracting data are also provided in the supplementary information, as well as further details regarding running of calculations and the visualisation and processing of data.

## 3.5 Computational Methods

The methods and basis sets used in this study are described below.

### 3.5.1 Density functionals

The meaning of the word functional refers to a function that is a function of a function. As was illustrated in equation (2.39) from the Kohn-Sham approach,  $T_S$ ,  $E_{ne}$ ,  $J$  and  $E_{xc}$  are all functionals of the electron density with  $E_{DFT}[n] = T_S[n] + E_{ne}[n] + J[n] + E_{xc}[n]$ . As the Kohn-Sham approach shows it is only the exchange-correlation energy  $E_{xc}$  part that needs to be estimated and therefore this is the major difference between different functionals within density functional theory (DFT), with each functional taking a different approach to estimating the exchange-correlation part of the total energy.

As was mentioned, DFT is not the only approach to approximating solutions to the Schrödinger equation (Chapter 2). Other approaches include configuration interaction (CI) expansions, diagrammatic Green's function techniques, quantum Monte Carlo approaches and others.<sup>51</sup> These are, however, outside the scope of this project. DFT and Time-Dependent DFT were used for all calculations carried out throughout this project. In Chapter 4 a range of functionals were compared to establish which yields the best agreement with the experimental spectra. These include functionals from a large range of classes such as local (B97D<sup>76,77</sup>, B98<sup>78</sup> and PBEPBE-D3<sup>79,80</sup>), hybrid (B3LYP-D3<sup>81</sup>), meta (M06-D3<sup>82</sup>) as well as long-range corrected (CAM-B3LYP-D3<sup>83</sup> and  $\omega$ B97XD<sup>84</sup>) functionals. Dispersion correction (in most cases Grimme's D3 correction)<sup>77,85,86</sup> were added to all functionals except for B98, for which GD3 has not been parameterised. B3LYP was used for all other calculations in Chapter 4. In Chapter 5 the PBEPBE functional was used for carrying out periodic lattice energy calculations. In Chapter 6 UB3LYP-D3 was used. The unrestricted method was used since scans were performed in the triplet state.

### 3.5.2 Basis sets

Only Gaussian-Type<sup>87</sup> orbital basis sets were used in this project. For the work in Chapter 4 the 6-311++G(d,p) basis set<sup>87-90</sup> was used except for calculations done on the asymmetric unit for which the 6-311G basis set was used since the addition of polarisation and diffuse functions made the calculation too expensive. The DNP+ (Double Numerical plus polarisation, with the addition of diffuse functions) basis set was used for lattice energy calculations in Chapter 5. In Chapter 6 the 6-311++G basis set was used. The addition of polarisation functions increased the computational cost past what was feasible, even without the addition of diffuse functions, and thus they were excluded from the basis set. Geometries were compared to that of experimental data from the CSD and found to be in good agreement.

### 3.5.3 Geometry optimisations

A geometry optimisation is a procedure whereby a program takes an input molecular geometry and makes small adjustments to the atomic positions whilst calculating the energy at each optimisation step until the minimum-energy structure is found. One should remember that in principle the true minimum will never be reached since the program will continue to perform optimisation steps only until the convergence criterion has been reached (Maximum force = 0.000450, Maximum displacement = 0.001800). This criterion can be altered and will determine how close the final structure is to the true minimum-energy structure. The final outcome is also highly dependent on the initial geometry and one must take care to provide an input structure that is near to the true desired structure. The default method used in Gaussian is the Berny<sup>91</sup> optimisation algorithm, which was used for calculations in this work. Materials Studio also has a range of available algorithms including adopted basis Newton-Raphson (ABNR), steepest descent, Quasi-Newton and more. For this work the Smart algorithm was used, which is a combination of the former three algorithms.

### 3.5.4 Frequencies

Frequencies are calculated for various different reasons: The first and most obvious is the prediction of an IR spectrum, which can, for example, be used in comparison with experimental spectra as an aid for confirming the structure of a synthesised molecule. Frequencies are also calculated after a geometry optimisation as a way of confirming that a minimum-energy structure has been obtained. If the structure is at a minimum all the frequencies will be positive, while if the structure is at a saddle point at least one of the frequencies will be negative. Frequencies are also used for calculating zero-point corrected energies.

### 3.5.5 Zero-point corrected energies

The total electronic energy  $E_{tot}$  is calculated as the energy relative to the nuclei and electrons when completely separated from each other. This is the energy for the molecular system completely at rest in the ground state. Although this already provides valuable information about the system this is not a physically probable state as a result of the Heisenberg uncertainty principle:<sup>22</sup>

$$\sigma_x \sigma_p \geq \frac{\hbar}{2} \quad (3.1)$$

A molecular system can never exist in a state where it sits motionless at the bottom of a potential well, otherwise its momentum and position will be completely known violating the Heisenberg uncertainty principle. This can be corrected for by adding the zero-point vibrational energy (ZPVE) to the total energy to obtain the zero point corrected total energy:

$$E_0 = E_{tot} + \text{ZPVE} \quad (3.2)$$

This is the energy for the lowest accessible energy state of the system and accounts for the vibrations that the molecule undergoes. The ZPVE can be calculated using the frequencies for all the normal modes of vibration of the molecular system  $\nu_i$ :

$$\text{ZPVE} = \sum_i 0.5h\nu_i \quad (3.3)$$

### 3.5.6 Lattice energies

The lattice energy of a crystal structure is the stabilisation energy as a result of the different parts coming together to form a crystal structure. This can be used to identify which phase, or phases, is thermodynamically preferred. In Chapter 5 the lattice energies calculated for the different crystal structures are reported. These were calculated as follows:

$$E_{latt} = E_{cryst}/z - \sum_i E_{asu_i} \quad (3.4)$$

with  $E_{latt}$  as the lattice energy of the asymmetric unit,  $E_{cryst}$  as the energy of the unit cell of the crystal structure,  $z$  as the number of asymmetric units per unit cell and  $E_{asu_i}$  as the energy of molecule  $i$  in the asymmetric unit when calculated as an isolated system.

### 3.5.7 Scans

The Gaussian program allows for relaxed scans of atomic distances, angles or dihedral angles to be carried out. A scan involves changing a specific parameter, such as the distance between two atoms, in a stepwise fashion from an initial to a final value. For fixed scans this is done rigorously while with relaxed scans a geometry optimisation is carried out at each scan step whilst fixing the parameter(s) that is being scanned. When a relaxed scan with multiple parameters is requested it will proceed as illustrated in Figure 3-8. At first only parameter A will be scanned with geometry optimisations taking place at each scan step whilst fixing parameter B. Parameter B will then be stepped once in the forward direction and A scanned backwards until reaching the initial value. Both parameters are stepped 9 times from their initial to their final values resulting in 10 scan steps for each parameter and thus  $10 \times 10 = 100$  scan steps in total.

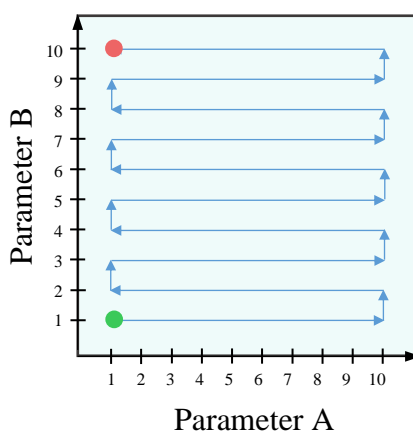


Figure 3-8: Illustration of how Gaussian performs scans of two parameters. The scan starts at the green dot and proceeds as indicated by the arrows until reaching the red dot.

### 3.5.8 Solvent model

An implicit solvent model or continuum solvation model is a way of modelling the solvent environment without explicitly having to include possibly hundreds of solvent molecules in the calculation. If this was done a system can quickly become too complex to be treated by quantum mechanics. The implicit solvent model allows for the study of a system in the solvent phase that otherwise would not have been possible. The solvent environment is generated by placing a uniform distribution of point charges around the solute. The polarizability of this model solvent is determined by the dielectric constant  $\epsilon$ , which is unique for each different solvent. In this project the Self-Consistent Reaction Field (SCRF)<sup>92</sup> approach was used along with the Polarisable Continuum Model (PCM), which is the default for the Gaussian program.

## Chapter 4: A theoretical explanation for the solvatochromic behaviour of hexahydroxy-hexaazaheptacyclo-octatetracontapentadecaene crystals

Under specific conditions trianlimine **1** will crystallise in the space group  $R3$  forming yellow crystals with 11 Å wide one-dimensional channels, as illustrated in Figure 4-1. These crystals undergo a rapid yellow-to-red colour conversion (Figure 4-2) above a critical humidity of 55%, at which point water vapour is absorbed into the channels. Via a computational study it was determined that the water interacts with the system by hydrogen bonding to accessible hydroxyl groups driving forward an enolimine-ketoenamine conversion via a [1,5]H shift.

This type of enolimine-ketoenamine equilibrium amongst Schiff bases is well known to occur as a photo-, thermo-, solvato- or ionochromic process.<sup>34,36,37</sup> This means that upon irradiation with light, upon heating, interaction with a solvent or interaction with an ionic species, respectively, a proton is shifted from the oxygen onto the nitrogen. This affects the hybridization of the oxygen and nitrogen atoms, and also changes the conjugated  $\pi$ -electron system resulting in a bathochromic shift, i.e. a change in a spectral band to a longer wavelength, in the UV-Vis spectrum.

Unit Cell Parameters	
Space group	$R3$
$a$ [Å]	50.685(4)
$b$ [Å]	50.685(4)
$c$ [Å]	9.633(4)
$\alpha$ [°]	90
$\beta$ [°]	90
$\gamma$ [°]	120
Volume [Å <sup>3</sup> ]	21431.68

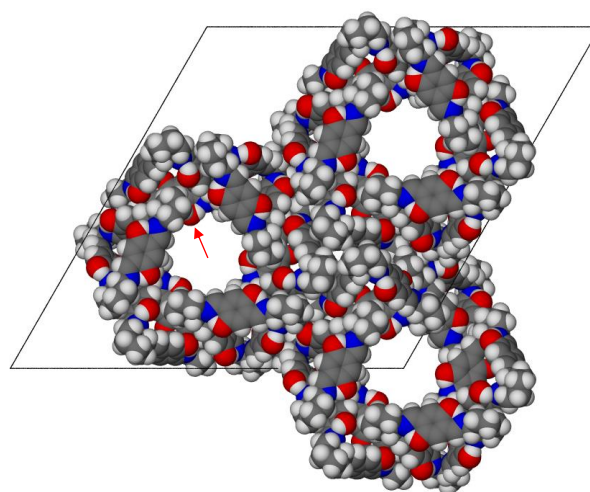


Figure 4-1: The unit cell of trianlimine **1** as crystallised in the  $R3$  space group. Hydroxyl groups are clearly visible pointing into the pores and accessible by water molecules (indicated by red arrow).



Figure 4-2: Crystals from trianlimine **1** absorb water above a humidity of 55%. The water diffuses into the channels from the left and right sides, causing a yellow-to-red colour change.

The system under investigation undergoes a similar transformation via a combination of sorptiochromic and hydrochromic processes. The porosity<sup>93</sup> of the system allows the framework to interact with atmospheric gases throughout the crystal. Atmospheric water can condense on the surface of the channels, interact with and alter the framework and afterwards leave the crystal through the channels allowing the framework to return to its original state. Both hydro- and sorptiochromism are considered sub-categories of solvatochromism.<sup>2</sup>

A computational approach was adopted for establishing the final, ketoenamine (red) state of the system, because crystal data alone was inadequate for determining the structure of the final state. The water molecules in the channels are disordered and thus their positions and mode of interaction could not be established with SCXRD. Hydrogen positions are also difficult to establish accurately with X-ray diffraction data alone, which is problematic since a small change such as a proton transfer can have a large effect on the colour properties of the material.

#### **4.1 Aims and objectives**

The aim of this study is thus to use computational means to explain the cause of the yellow-to-red colour conversion. Studying the colour properties of a system requires a high level of theory since the energy differences involved in colour changes are very small. This is troublesome for a periodic system of such a size and therefore the first objective is to reduce the periodic system to a smaller, model system that in itself contains all the information necessary for explaining the colour properties of the bulk material. This will be done by identifying and isolating the chromophore of the system.

The next objective is to establish the final state of the system. This involves establishing the positions of hydrogen atoms that are unknown or uncertain within the framework in such a manner that it would explain the red colour of the material. The initial (yellow) state has been established since the compound was synthesised and characterised and the crystal data provides a clear picture of what the system looks like and where all hydrogen atoms are located.

This leads to the final goal of this study, which is to establish the mode of interaction of the framework with water that would explain how the system spontaneously evolves from the initial to the final state when the water interacts with the system.

## 4.2 Methods

The crystals of trianglimine **1** (Figure 4-3) were previously grown by a colleague, Dr Agnieszka Janiak,<sup>94</sup> and the crystal structure determined with the crystal in both the yellow and red form. In addition, the UV-Vis spectrum of crystals in both forms and the H<sub>2</sub>O sorption was measured as a function of humidity (Dr A. Janiak). As stated above, this information alone does not provide us with the knowledge required to establish a mode of interaction, hence the current computational study was undertaken.

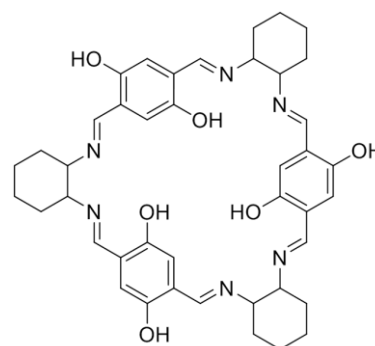


Figure 4-3: Trianglimine **1**.

Since Materials Studio<sup>71</sup> has a graphical user interface suitable for studying periodic systems, it was initially used for identifying which parts of the asymmetric unit are accessible to water, how large the channels are and what parts of the system are possibly responsible for the visible colour of the crystals. The accessible surface can be calculated and visualised using the Atom Volumes and Surfaces Tool. All results presented in this chapter are from calculations carried out with Gaussian 09<sup>23</sup> using DFT for optimisations and calculating frequencies and orbitals and TD-DFT for predicting spectra. For calculations done on the asymmetric unit (section 4.3) B3LYP-D3 was used with the 6-311G basis set. In section 4.4, the 6-311++G(d,p) basis set was used in combination with a range of methods, namely B3LYP-D3, B97D, B98, CAM-B3LYP-D3, M06-D3, PBEPBE-D3 and,  $\omega$ B97XD. Dispersion correction were added to all functionals except for B98, for which dispersion has not been parameterised. B3LYP-D3 showed the best comparison to the experimental spectrum and was therefore used, along with the 6-311++G(d,p) basis set, in section 4.5.

## 4.3 Determination of a model system

As previously mentioned in Section 4.1, the periodic system needs to be reduced to a smaller, isolated model system that can be studied at a high level of theory. This is essential because the colour change is a result of small changes in the energies of the molecular orbitals, particularly the highest occupied and lowest unoccupied orbitals. The UV-Vis spectrum was predicted for the asymmetric unit (Figure 4-4) and the orbitals calculated (Figure 4-5). From this the peaks with significantly large intensities in the UV and visible regions can be identified. These excitations take place between predominantly six pairs of occupied (particularly HOMO down to HOMO-5) and unoccupied (LUMO up to LUMO+5) molecular orbitals.

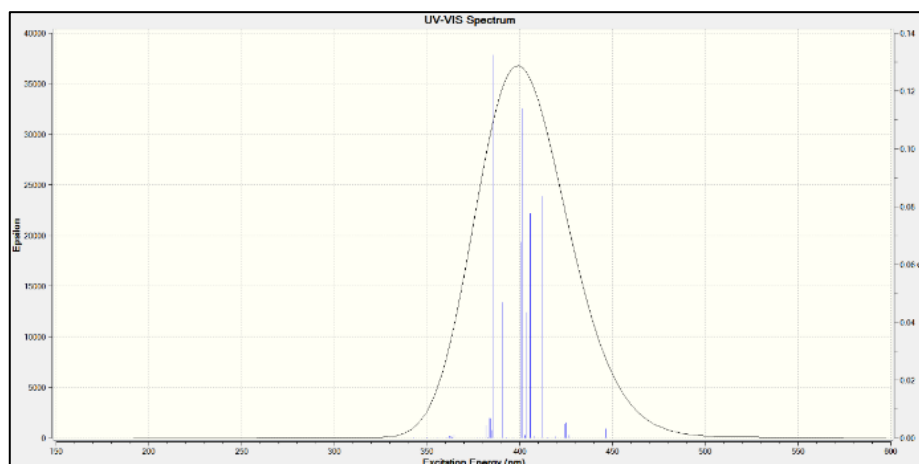


Figure 4-4: Predicted UV-Vis spectrum for the asymmetric unit of the Trianglimine **1** crystals.

These twelve molecular orbitals (Figure 4-5) can be used to identify the chromophore(s) of the system. The six highest occupied orbitals, HOMO-5 up to the HOMO, are always located on the hydroquinone parts of the molecules. The same is the case for the LUMO up to LUMO+5 orbitals. Also important to note is that each pair of occupied and unoccupied orbitals responsible for a signal in the UV-Vis spectrum is located on the same phenyl ring with a negligible amount of overlap. This suggests that the chromophores are located on the hydroquinone parts of the system, which makes sense since these orbitals have mainly *p*-orbital character. These *p* orbitals are involved in a delocalised  $\pi$ -bonded system and  $\pi$  bonds are usually higher in energy than  $\sigma$  bonds, with the corresponding anti-bonding orbitals being lower in energy than  $\sigma$  anti-bonding orbitals. It is typical for organic molecules that show colour (such as indigo) to have large systems of conjugated *p* orbitals.<sup>3</sup> The chromophore is therefore on the hydroquinone part of the molecule and will therefore be isolated in this study.

This was achieved by cutting the chromophore (Figure 4-6) out from the periodic system along with two cyclohexyl groups on either side. This new model compound was then optimised in the gas phase. From this structure all the information needed to provide an explanation for the large scale colour properties can be extracted. It is important to remember that this is still an approximation done for a specific purpose, which is to explain the colour properties of the system. In the periodic system the chromophore is still involved in interactions with its neighbouring atoms.

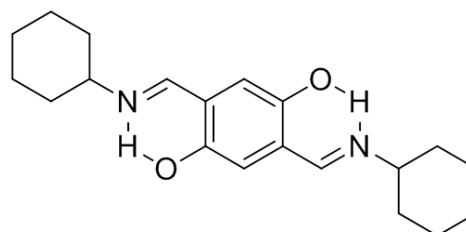


Figure 4-6: The central hydroquinone part of trianglimine **1** is responsible for the visible colour of the system, i.e. the chromophore, to be used as a model compound for this study.

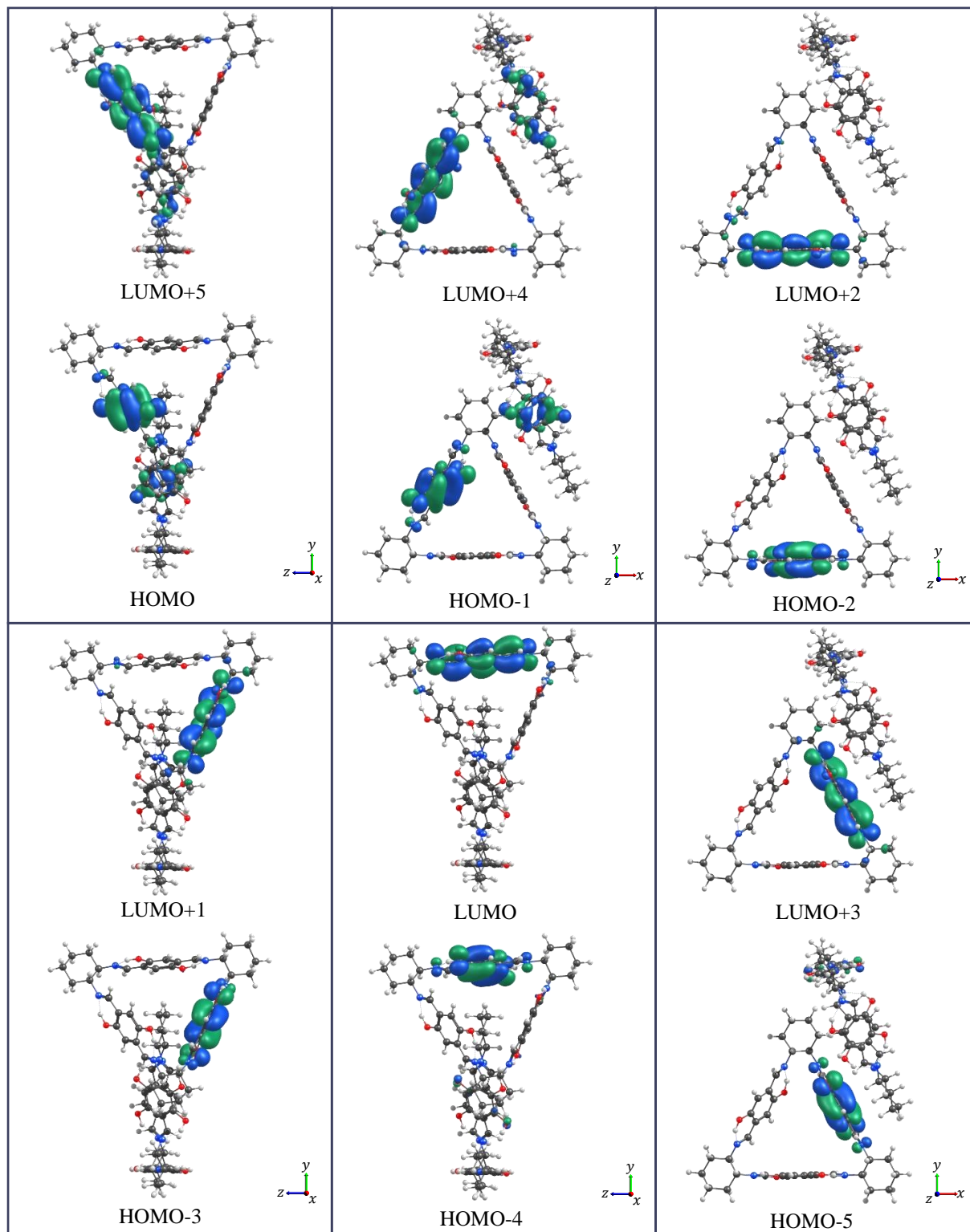


Figure 4-5: The six highest occupied MOs and six lowest unoccupied MOs are displayed (isovalue set to 0.03) on the asymmetric unit and in pairs of occupied and unoccupied orbitals. Each pair of occupied and unoccupied orbitals correspond to one of the six largest peaks in the predicted UV-Vis spectrum for the asymmetric unit (Figure 4-4).

#### 4.4 Stable hydrated states

Utilising the simplified model identified above, the chromophore can be altered to obtain different isomers for which the UV-Vis spectra can be predicted for comparison to the experimentally observed spectra. Since hydrogen atomic positions cannot be determined accurately using X-ray diffraction, the focus was put on the position of the hydrogen atoms whilst from X-ray data it is already known that only small changes occur in the positions of heavy atoms. The five most reasonable structures are illustrated in Figure 4-7. The system was altered in a way that could reasonably take place under mild conditions, upon interaction with water and at room temperature. This was done by simply varying the position of the alcoholic hydrogen atoms, which can either point inwards, hydrogen bonded to the nitrogen, point outwards, eliminating the hydrogen bond, or be shifted onto the nitrogen. The latter affects the system in a manner that alters the hybridisation of the oxygen and nitrogen atoms involved, and breaks the aromaticity of the phenyl ring. This is illustrated in Figure 4-8.

A range of DFT functionals were used to optimise each of the five conformations and predict the UV-Vis spectra using TD-DFT calculations. The results are listed in Table 4-1. These can be compared to the experimental spectra (Figure 4-14), where a peak could be identified at 404 nm for both the dry and hydrated (yellow and red) crystals, along with a small but diffuse peak at roughly 530 nm that occurs only for the hydrated structure.

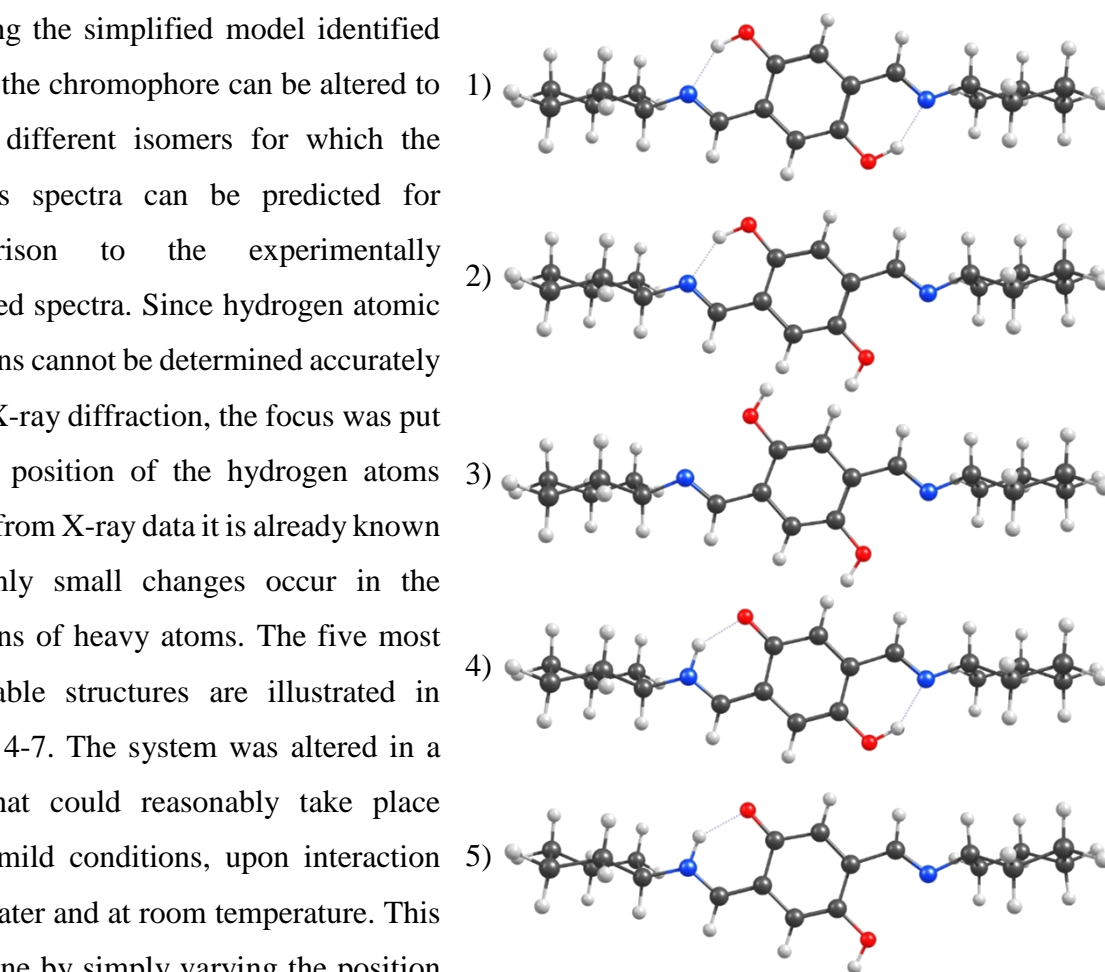


Figure 4-7: Five isomers of the chromophore are illustrated, showing the different possible alcoholic hydrogen positions. The structures are labelled 1 to 5 for referencing purposes.



Figure 4-8: A [1,5]H shift results in the keto-isomer.

Table 4-1: 1 to 5 refers to Structures 1 to 5 from Figure 4-7. HOMO-LUMO transitions in wavelength (nm).

Functional	Structure # (results in wavelength, nm)				
	1	2	3	4	5
B3LYP-GD3	405	374	346	516	457
B97D	475	433	397	602	521
B98	402	371	344	509	453
CAM-B3LYP-GD3	356	333	312	449	408
M06-GD3	392	366	342	500	448
PBEPBE-GD3	495	445	404	606	521
$\omega$ B97XD	357	334	314	450	409

Upon going from structure **1** to **2** to **3** one hydrogen bond between the alcoholic hydrogen and the nitrogen atoms is eliminated at each step. This causes a hypsochromic shift (a change in a spectral band to a shorter wavelength) in the single peak that falls within the visible spectrum (see changes in wavelengths listed in Table 4-1). This trend is observed for all of the functionals to varying degrees. B3LYP-D3 shows the best comparison to the experimental spectrum with structure **1** having a peak at 405 nm. B98 (without dispersion correction) is also close with a peak at 402 nm. CAM-B3LYP-D3 and  $\omega$ B97XD overestimate the energy and B97D and PBEPBE-D3 underestimate it.

Upon going from isomer **1** to **4** and **5** a bathochromic shift (a change in a spectral band to a longer wavelength) is observed in both cases where one of the alcoholic hydrogen atoms is shifted onto the nitrogen atom and, for structure **5**, the second is rotated outwards, eliminating the hydrogen bond. For predicting structure **4** and **5** the functionals perform similarly to above.

It is important to note that the lowest-energy excitation, corresponding to the transition falling within the visible spectrum, was always a singlet excitation (excited state with a multiplicity of 1) and resulted from the excitation of a single electron from the HOMO to the LUMO. This allows us to draw some conclusions based on the energies of the HOMO and LUMO orbitals in order to rationalise the spectral shifts observed upon going from structure **1** to one of the four isomeric structures.

Firstly the intramolecular hydrogen bond between the hydrogen and nitrogen atoms, although having an overall stabilising effect, draws electron density away from the conjugated  $\pi$ -system. Once the hydrogen bond is broken the  $p$ -electrons on the nitrogen can have a larger contribution to the conjugated  $\pi$ -system and thus to the HOMO. Twisting one alcoholic hydrogen atom outwards, results in an increased contribution from the nitrogen  $p$ -orbital to the

HOMO. Twisting the second hydrogen atom outwards has exactly the same effect (refer to structures **1**, **2** and **3** from Figure 4-7). The increase in the *p*-orbital character of the HOMO results in a decrease in its energy, and an increase in the energy of the LUMO. The larger gap requires a higher energy for excitation hence a shorter wavelength in the UV-Vis spectrum.

Upon transferring one of the alcoholic hydrogen atoms onto the nitrogen a different outcome is observed. The hydroxyl group becomes a ketone, the imine becomes an amine and the aromaticity of the phenyl ring is broken to allow the movement of electrons, as shown in Figure 4-8, and hence formation of the N-H bond. This causes an increase in the energy of the HOMO and a decrease in the energy of the LUMO. The smaller gap requires less energy for excitation resulting in a bathochromic shift.

Since B3LYP-D3 shows the best agreement with the experimental spectrum – with a peak at 405 nm compared to the experimental one at 404 nm – it will be used for further calculations. The peak at 516 nm for structure **4** correlates well with the peak at 530 nm in the experimental spectrum, which suggests that this is in fact the final state that we are looking for. The peak at 530 nm lies within the green region of the visible spectrum resulting in some of the blue, green and yellow light being absorbed and a complementary and thus visible red colour. Similarly 405 nm lies within the violet/indigo region of the spectrum which has a complementary and thus visible yellow colour.

This solves the problem of determining what the final state should look like. An alcohol converting to a ketone accompanied by an imine to amine transformation, results in the observed yellow-to-red conversion upon hydration of the crystals.

#### **4.5 Proposed mode of interaction of trianglimine 1 with water**

Lastly, the role of water in spontaneously producing the final ketoenamine state needs to be determined. We assume that the proton transfer occurs from the alcohol to the imine, and not from a hydrogen atom elsewhere. This type of transfer (illustrated in Figure 4-8) can only occur if the hydrogen points inwards towards the nitrogen, with a hydrogen bond that would direct the movement of the hydrogen atom towards the nitrogen. Furthermore, the alcohol form must be destabilised, making the imine form favourable and the OH bond needs to be weakened allowing the OH bond to stretch. Stretching the OH bond allows for a [1,5]H shift to take place, transferring the hydrogen atom from the oxygen to the nitrogen.

This process can only occur upon the formation of a hydrogen bond between incoming water molecules and the oxygen from the alcohol, as illustrated in Figure 4-9. In order to test this hypothesis H<sub>2</sub>O molecules are added randomly to structures **1** and **4**, in the manner

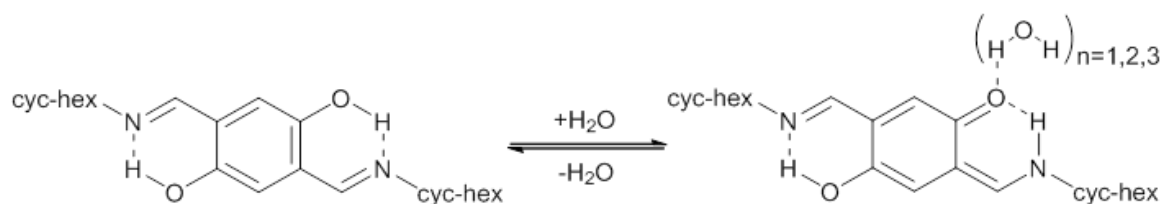


Figure 4-9: A [1,5]H shift results in the keto-isomer. This breaks the aromaticity and affects the hybridisation of the oxygen and nitrogen atoms. A mode of interaction with water is suggested which would drive this reaction forward.

Table 4-2: Difference in energy between the enolimine and ketoenamine forms depending on the number of H<sub>2</sub>O molecules added in the above position as illustrated in Figure 4-9. For adding a solvent to the calculation a polarizable continuum solvent model (PCM) was used.  $\Delta E$  is calculated as the energy of the ketoenamine form minus that of the enolimine form. Thus a positive value suggests the enolimine is more favourable and a negative value the ketoenamine.

No. of H <sub>2</sub> O molecules	$\Delta E$ (kcal/mol)	
	Gas phase	Solvent (water)
0	5.68	1.87
1	3.25	-0.72
2	-1.13	-2.48
3	-2.05	-4.44

illustrated in Figure 4-9, to form mono-, bi- and trifurcated systems. The structures were allowed to optimise, either in gas phase or in the presence of a continuum solvent model. The final optimised geometries are illustrated in Figure 4-10 to Figure 4-13 and the energies summarised in Table 4-2.

A clear trend is observed upon going from a single water molecule to a bifurcated or trifurcated system. Initially, in the gas phase the enolimine form is 5.68 kcal/mol higher in energy than the ketoenamine form but upon the addition of one water molecule, to hydrogen bond to the alcohol, the energy difference is lowered to 3.25 kcal/mol. Upon addition of two or three H<sub>2</sub>O molecules to form hydrogen bonds, the ketoenamine form becomes lower in energy than the enolimine form, with differences of 1.13 and 2.05 kcal/mol respectively. Including a solvent model strengthens this trend, so that addition of one water molecule already results in the ketoenamine form being lower in energy, while for a trifurcated system the amine is up to 4.44 kcal/mol lower in energy than the alcohol form.

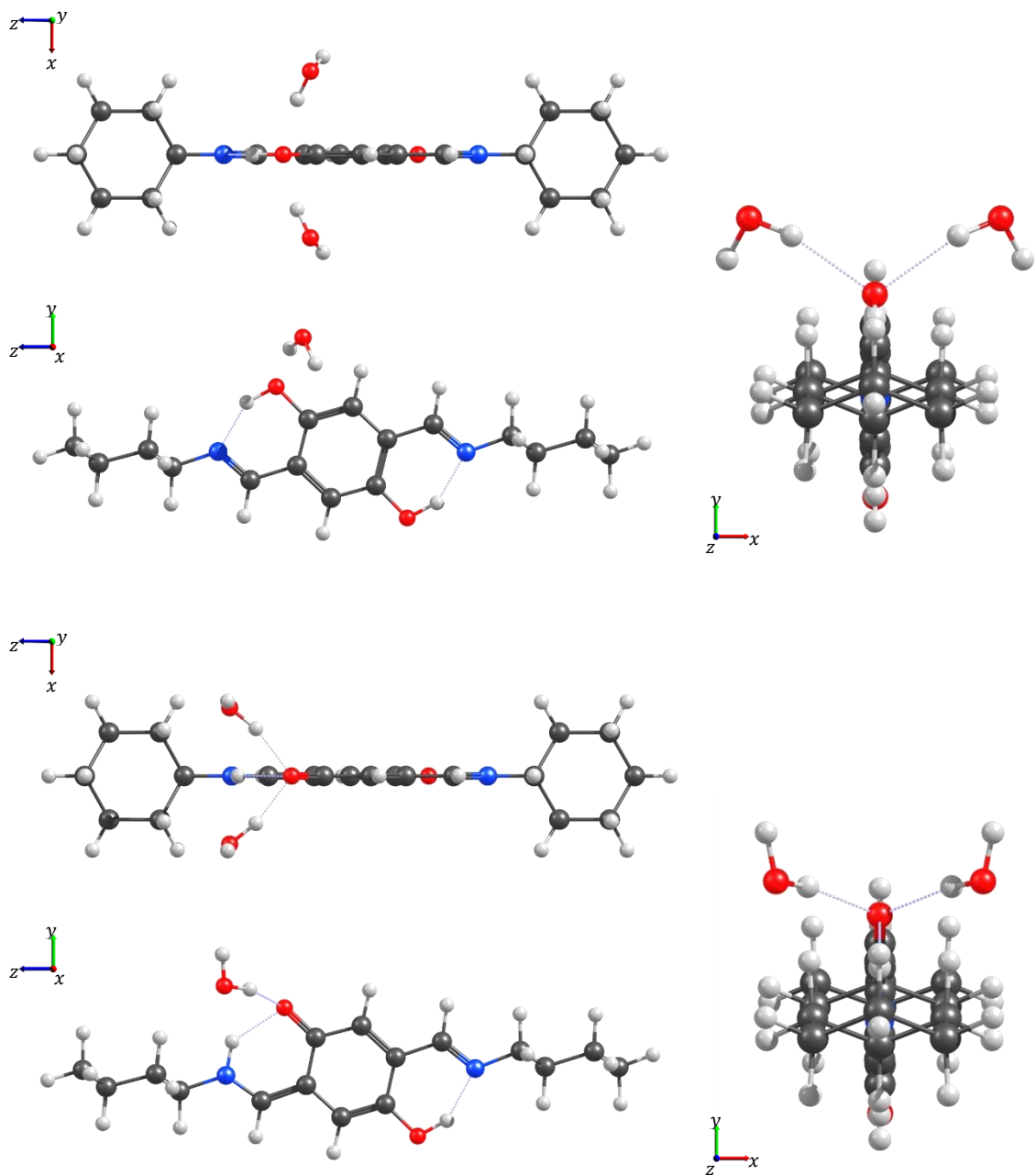


Figure 4-10: Bifurcated systems in the alcohol (top) and amine (bottom) form, optimised in the gas phase

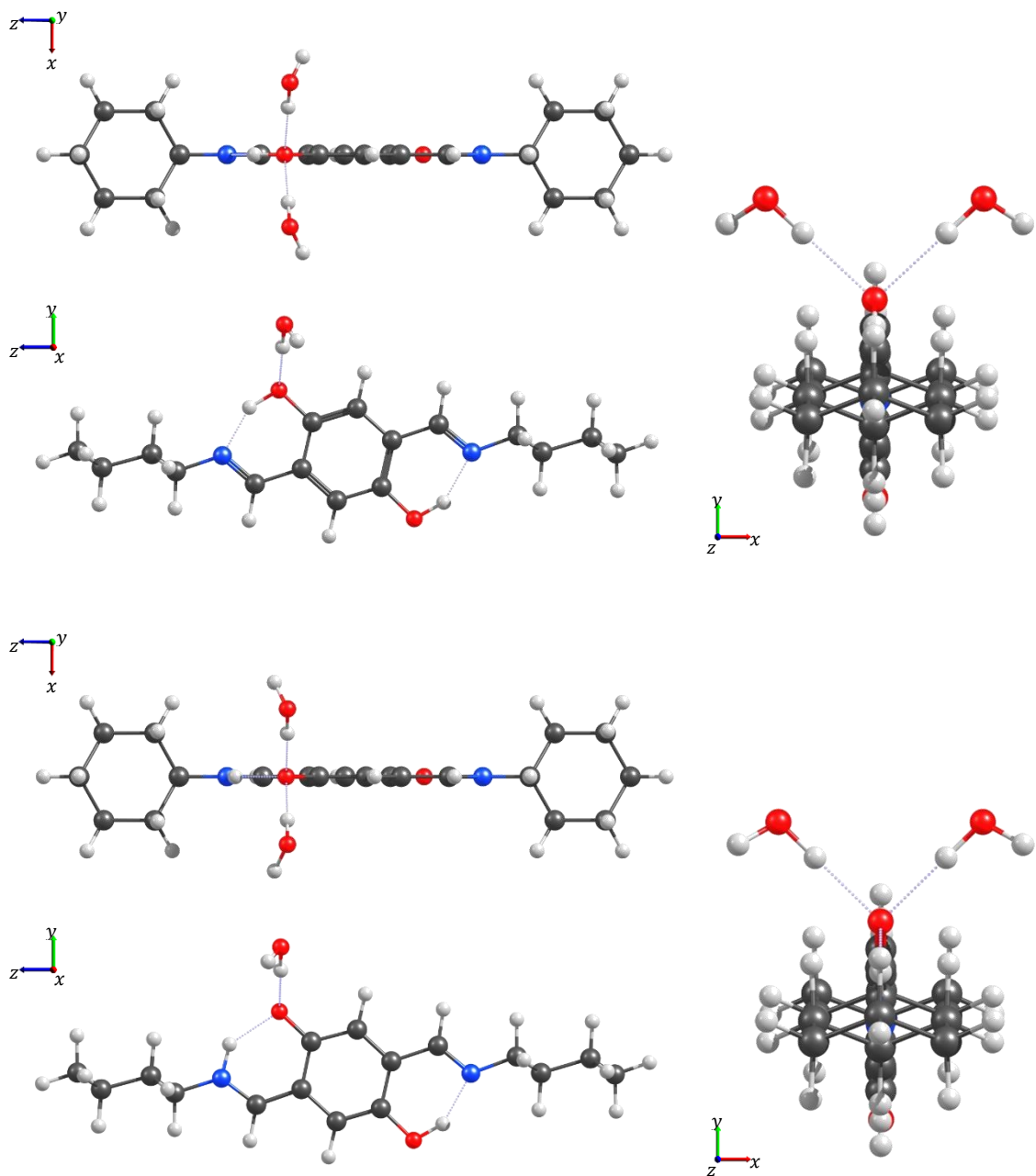


Figure 4-11: Bifurcated systems in the alcohol (top) and amine (bottom) form, in a polarizable continuum solvent model.

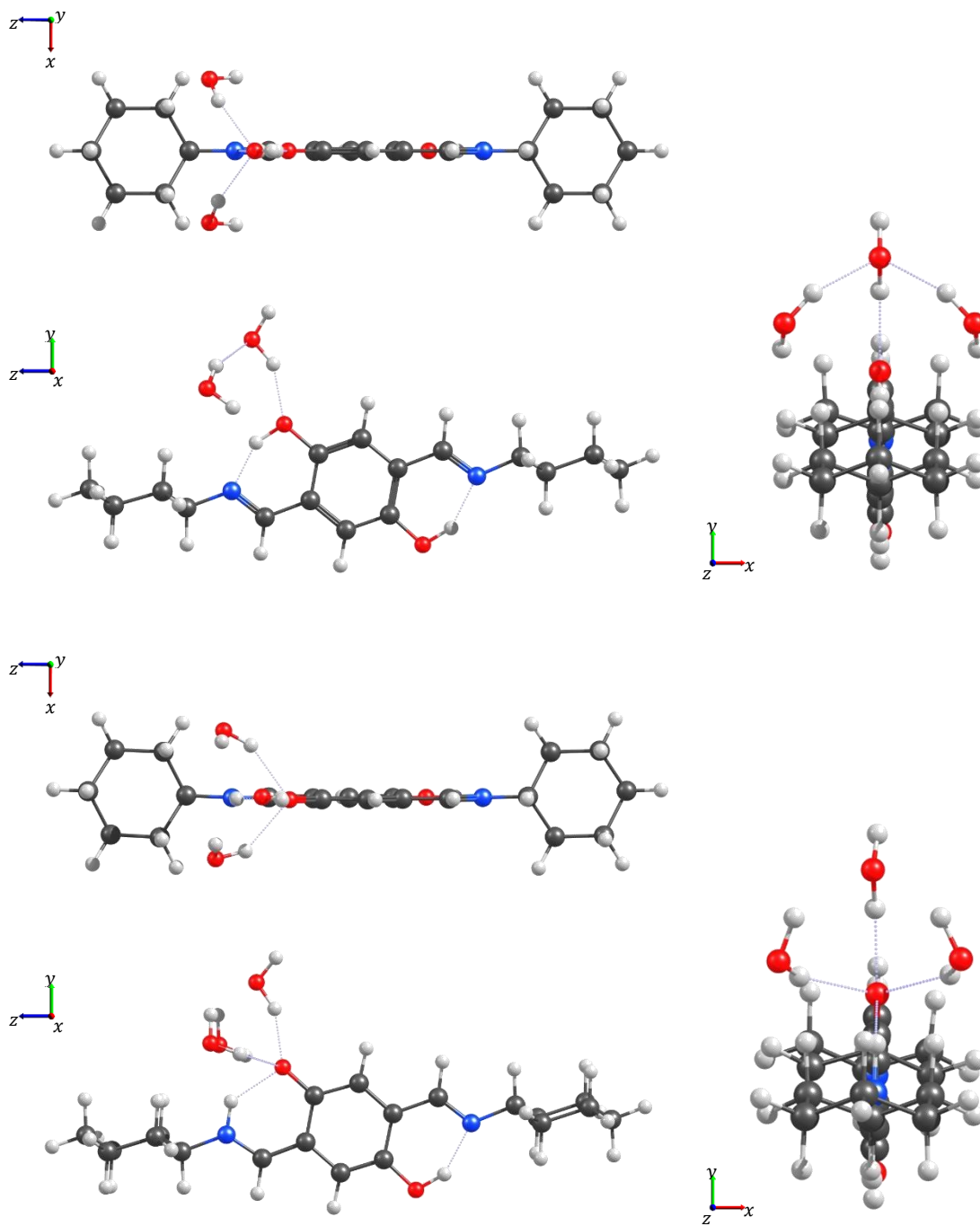


Figure 4-12: Trifurcated systems in the alcohol (top) and amine (bottom) form, optimised in the gas phase.

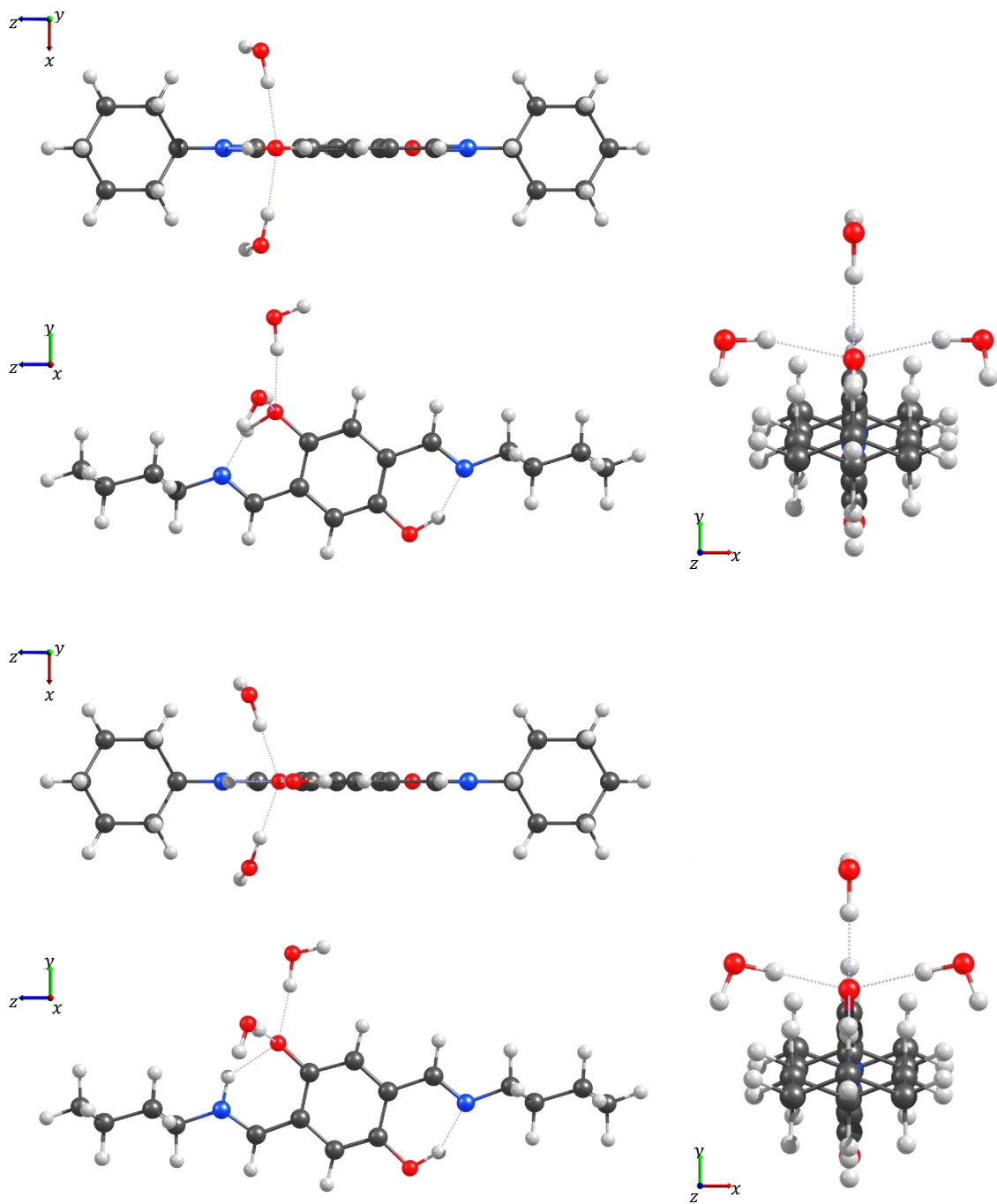


Figure 4-13: Trifurcated systems in the alcohol (top) and amine (bottom) form, in a polarizable continuum solvent model.

## 4.6 Discussion

The results above have established that the yellow-to-red colour conversion of trianlimine **1** upon exposure to humidity requires that an enolimine-ketoenamine transformation needs to take place. Although it is common for Schiff-base-like moieties to undergo this kind of transformation as a photochromic or thermochromic process, this system exhibits a unique combination of a hydro- and a sorptiochromic process resulting in the enolimine-ketoenamine transformation. The formation of a hydrogen bond with water significantly alters the preference for isomer **4** (Figure 4-7) relative to isomer **1**, resulting in the breaking and formation of bonds.

To bring this back to the crystal structure: the asymmetric unit consists of two trianlimine **1** molecules, each containing three chromophores. Out of the six chromophores only one is accessible via the channel (Figure 4-1) and will thus undergo the transformation. For this reason in the experimental spectrum (Figure 4-14) only a portion of the peak shifts to a higher wavelength and into the yellow region of the electromagnetic spectrum. Since more yellow light is absorbed the crystals will appear red. By combining one sixth the spectrum from structure **4**, which is the ketoenamine form, and five sixths of the spectrum from structure **1**, the enolimine form, the experimental spectrum can be reproduced fairly well (Figure 4-15).

## 4.7 Summary

In summary, it has been shown how a large periodic system can be reduced to a smaller isolated system in order to study intricate properties that would otherwise not be possible in the large periodic structure. How the larger system is reduced to a smaller one will always depend on what properties need to be studied, and one must ensure that a simplified model still contains all the information necessary to explain the relevant bulk material properties. By calculating the spectra of the possible isomers of trianlimine **1** the final form of the system was determined. Via elimination it was therefore established that the formation of the amine form of trianlimine **1** is responsible for the yellow-to-red colour change which is substantiated by literature.<sup>34,36,37</sup> Lastly it was shown that by introducing a water molecule to hydrogen bond to the OH group the difference in energy between the enolimine and ketoenamine state is reduced from 5.68 to 3.25 kcal/mol. Further addition of H<sub>2</sub>O molecules in the presence of a solvent environment causes the amine form to be lower in energy. With the addition of three H<sub>2</sub>O molecules and in the presence of a solvent environment the amine form becomes thermodynamically preferred with an energy difference of 4.4 kcal/mol.

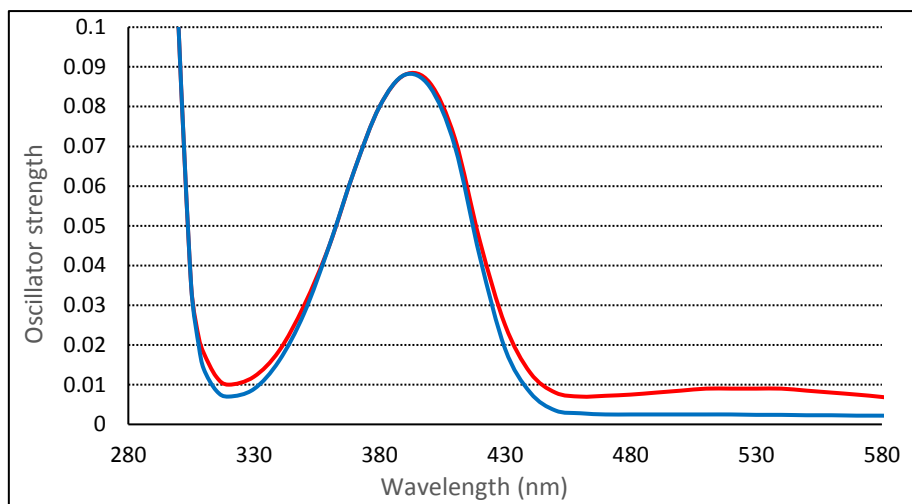


Figure 4-14: Experimental UV-Vis spectra of dry (blue) and wet (red) crystals of Trianglimine 1. For the dry crystals there is a peak at 404 nm, ranging over the violet to indigo part of the visible spectrum. For the wet crystals a broad peak occurs at about 530 nm, which is within the green part of the visible spectrum.

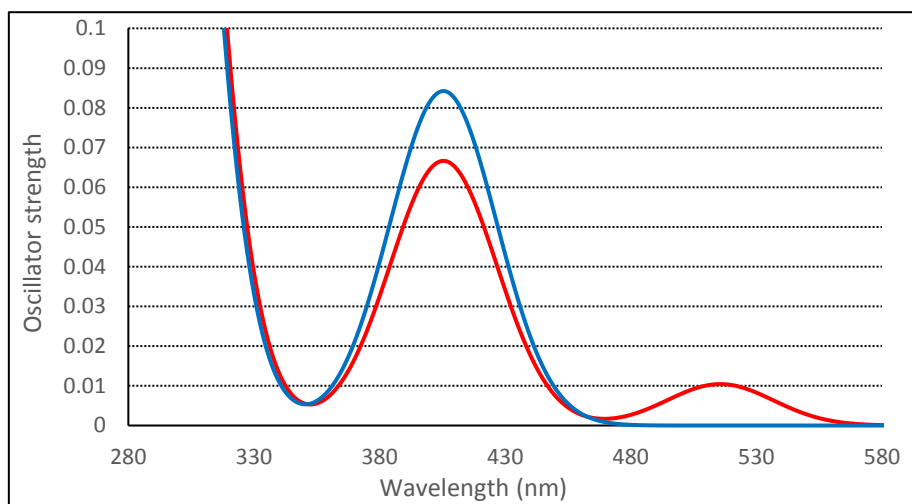


Figure 4-15: The blue curve is the predicted UV-Vis spectrum of structure 1 (Figure 4-7). By combining the predicted spectra from structures 1 and 4 (red curve) a spectrum can be generated that is similar to the experimental one (Figure 4-14).

## Chapter 5: Reversible phase transition of a photochromic diarylethene: perfluoro-cyclopentene-diyl-bis-propylthiophene-dipyridine

In 2014 Kobatake and Kitagawa described the polymorphism of the photochromic diarylethene, **DA-10** (Figure 5-1).<sup>50</sup> Two phases were described, the **DA-10-[o]- $\alpha$**  phase from acetone and the **DA-10-[o]- $\beta$**  phase from hexane with respective space groups  $P2_1/c$  and  $C2/c$ . Both forms exhibit photochromic behaviour in the crystalline state, undergoing a colourless-to-blue conversion upon irradiation with UV light and the reverse with visible light. Upon heating above 100 °C the **DA-10-[o]- $\alpha$**  phase is converted to the **DA-10-[o]- $\beta$**  phase, via a single-crystal-to-single-crystal transformation, while the **DA-10-[o]- $\beta$**  phase undergoes no change upon heating. Both phases melt at 160 °C.

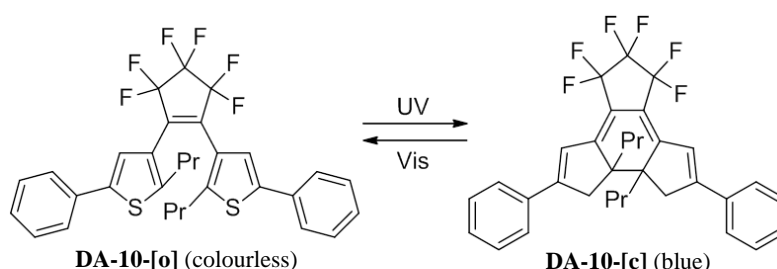


Figure 5-1: 1,2-bis(5-phenyl-2-propyl-3-thienyl)perfluorocyclopentene (left) and its ring-closed form (right). Molecules will be referred to by the labels **DA-10-[o]** and **DA-10-[c]**.

Although there are many intricacies in defining polymorphism in chemistry, McCrone's<sup>95,96</sup> working definition is still relevant today and sufficient for describing the phenomenon: "a solid crystalline phase of a given compound resulting from the possibility of at least two crystalline arrangements of the molecules of that compound in the solid state." As a result of polymorphism two different materials or crystals of exactly the same compound(s) can exhibit different chemical and physical properties depending on how the molecules pack in the crystalline phase. This allows for differentiation based upon properties such as conductivity,<sup>97</sup> magnetism,<sup>98</sup> luminescence<sup>99,100</sup> and photochromism,<sup>101,102</sup> which makes polymorphism an important field of study.

Photochromism is defined as a reversible transformation of a chemical species between two isomers having different absorption spectra, induced in one or both directions by photoirradiation.<sup>103</sup> This is accompanied by a change in physical properties of the material such as absorbance, luminescence, oxidation-reduction potentials and dielectric constants.<sup>50,104</sup> Such compounds have the potential to be used in applications such as optical switches,<sup>105</sup> optical memory chips,<sup>106</sup> photomechanical devices or actuators<sup>105,107</sup> and optoelectrical devices.<sup>108</sup>

Any of above-mentioned applications requires a high degree of control over the state that the system is in as well as resistance to degradation over time, which would render such a device unusable. Diarylethenes are a group of compounds that are potentially useful in applications owing to their thermal stability, high sensitivity, fatigue-resistance and rapid response to light.<sup>103</sup> Another property that makes diarylethenes promising is their reactivity in the solid state, which is essential if they are to be used in solid state media such as those previously mentioned. The polymorphism of diarylethenes adds another dimension to the tunability of the chemical and/or physical properties of a material.

A compound similar to **DA-10**, previously synthesised by a colleague (Dr D. Castell)<sup>60</sup> was studied during this project. This compound, labelled as **DA-1** (Figure 5-2), differs from **DA-10** having pyridyl rings substituted in the place of the phenyl rings. The presence of nitrogen atoms adds the possibility of coordination to metals or the formation of stronger interactions or hydrogen bonds with neighbouring molecules. This could result in a different packing arrangement to that found by Kobatake and Kitagawa, which would alter physical and chemical properties of the system.

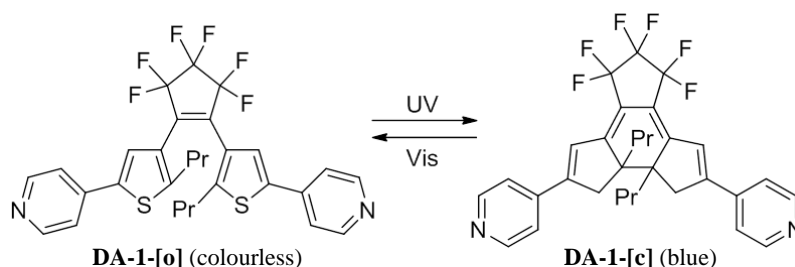


Figure 5-2: 1,2-bis(5-pyridyl-2-propyl-3-thienyl)perfluorocyclopentene (left) and its ring-closed form (right). Molecules will be referred to by their labels, **DA-1-[o]** and **DA-1-[c]**.

## 5.1 Aims and objectives

The first aim is to recrystallise **DA-1-[o]** and **DA-1-[c]** from a range of different solvents at ambient conditions to see what phases can be obtained. The crystal structures for the different forms will be determined using single-crystal X-ray diffraction. Different experimental and computational tools will then be used to study how the different phases behave under heating and whether they are interconvertible or not. We will determine which of the phases is thermodynamically preferred at ambient conditions and whether there are temperature-dependent phases that are only accessible by heating. The last aim is to compare our results to **DA-10** reported by Kobatake and Kitagawa in order to see how the introduction of pyridyl rings changes the packing of the system.

## 5.2 Methods

Crystals were grown from a range of solvents with different polarities using the method of crystallisation by evaporation. Crystallographic data were collected with single-crystal X-ray diffraction (SCXRD) and solved using X-Seed. The thermodynamics of each phase was studied using differential scanning calorimetry (DSC). The phase changes were studied using both variable temperature single crystal X-ray diffraction (VT-SCXRD) and variable temperature power X-ray diffraction (VT-PXRD) as well as hot-stage DSC for visualising crystals at elevated temperatures. Mercury was used for carrying out powder pattern predictions in order to relate crystal structures to the powder patterns and to study close contacts or strong interactions in the crystal system. Lastly the DMol<sup>3</sup> module in Materials Studio was used for calculating and comparing lattice energies for the different phases in order to differentiate between the thermodynamically and kinetically preferred phases.

## 5.3 Results

When recrystallised from acetone and hexane two different types of crystals were obtained, denoted as **DA-1-[o]- $\alpha$**  and **DA-1-[o]- $\beta$** , respectively (Figure 5-3). Crystallisation from cyclohexane resulted in **DA-1-[o]- $\beta$**  and crystallisation from dimethyl sulfoxide in **DA-1-[o]- $\alpha$** . Crystallisation from toluene, dichloromethane and chloroform resulted in very small crystals that could not be studied using X-ray diffraction. Since there was too little material, these crystals could also not be studied with PXRD but it was noted that the crystals looked similar

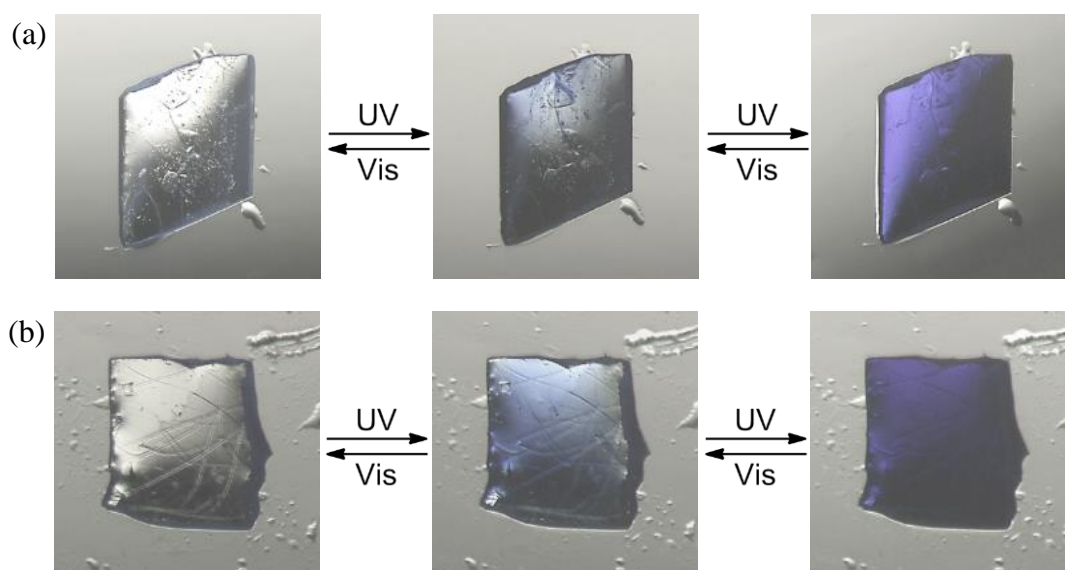


Figure 5-3: Photochromism of the (a) **DA-1-[o]- $\alpha$**  phase and of the (b) **DA-1-[o]- $\beta$**  phase.

to the plate-like crystals that grew from acetone. In acetone the **DA-1-[o]- $\alpha$**  crystals grow as large, thin plates that can be cut into smaller pieces, as shown in Figure 5-3 (a). In hexane the **DA-1-[o]- $\beta$**  crystals grow in plates that are slightly thicker than the plates of the **DA-1-[o]- $\alpha$**  crystals. Both the **DA-1-[o]- $\alpha$**  and the **DA-1-[o]- $\beta$**  crystals exhibit photochromic behaviour. Upon irradiation with UV light the crystals turn dark blue and upon irradiation with visible light they revert back to the colourless form.

The single crystal X-ray diffraction data were collected for both types of crystal at -173 °C; the crystallographic data are summarised in Table 5-1. The structures were also obtained at room temperature and except for a small amount of thermal expansion no differences were observed in the crystal packing. Both forms crystallised in the space group  $P\bar{1}$  in the monoclinic crystal system with two molecules in the asymmetric unit and four in the unit cell. The distances between the reactive carbon atoms in the two crystal structures were 3.660 Å and 3.793 Å for the **DA-1-[o]- $\alpha$**  phase and 3.677 Å and 3.680 Å for the **DA-1-[o]- $\beta$**  phase. These are short enough for the diarylethene molecules to undergo the photocyclisation reaction upon irradiation with UV light.<sup>15</sup> Molecular packing diagrams for both phases are illustrated in Figure 5-4.

Table 5-1: Crystallographic data for the **1a- $\alpha$** , **1a- $\beta$**  and **1a- $\gamma$**  phases.

	<b>DA-1-[o]-<math>\alpha</math></b>	<b>DA-1-[o]-<math>\beta</math></b>	<b>DA-1-[o]-<math>\gamma</math></b>
Formula	C <sub>58</sub> H <sub>48</sub> N <sub>4</sub> F <sub>12</sub> S <sub>4</sub>	C <sub>58</sub> H <sub>48</sub> N <sub>4</sub> F <sub>12</sub> S <sub>4</sub>	C <sub>29</sub> H <sub>24</sub> N <sub>2</sub> F <sub>6</sub> S <sub>2</sub>
Formula weight	1243.46	1243.46	578.64
T [°C]	-173	-173	100
Crystal system	Monoclinic	Monoclinic	Monoclinic
Space group	$P\bar{1}$	$P\bar{1}$	$C2/c$
$a$ [Å]	10.771(11)	10.9044(8)	20.8983(13)
$b$ [Å]	13.475(13)	12.7121(9)	12.5685(8)
$c$ [Å]	19.30(2)	20.1085(15)	11.4529(8)
$\alpha$ [°]	76.327(10)	97.522(2)	90
$\beta$ [°]	86.511(11)	98.045(2)	109.611(2)
$\gamma$ [°]	85.237(11)	102.198(2)	90
Volume [Å <sup>3</sup> ]	2710.53	2660.31	2833.72
Z	2	2	4
Density [g cm <sup>-3</sup> ]	1.5233	1.5521	1.3561

Differential scanning calorimetry (DSC) was used to study the thermodynamics of the two phases. Figure 5-5 shows the change in heat flow upon heating of the two different forms of the crystals. For the **DA-1-[o]- $\alpha$**  phase a broad endothermic peak occurs between about 70 °C and 100 °C with the maximum at 93 °C. Upon further heating another endothermic peak at 165 °C indicates the melting of the crystals. The **DA-1-[o]- $\beta$**  phase shows an endothermic

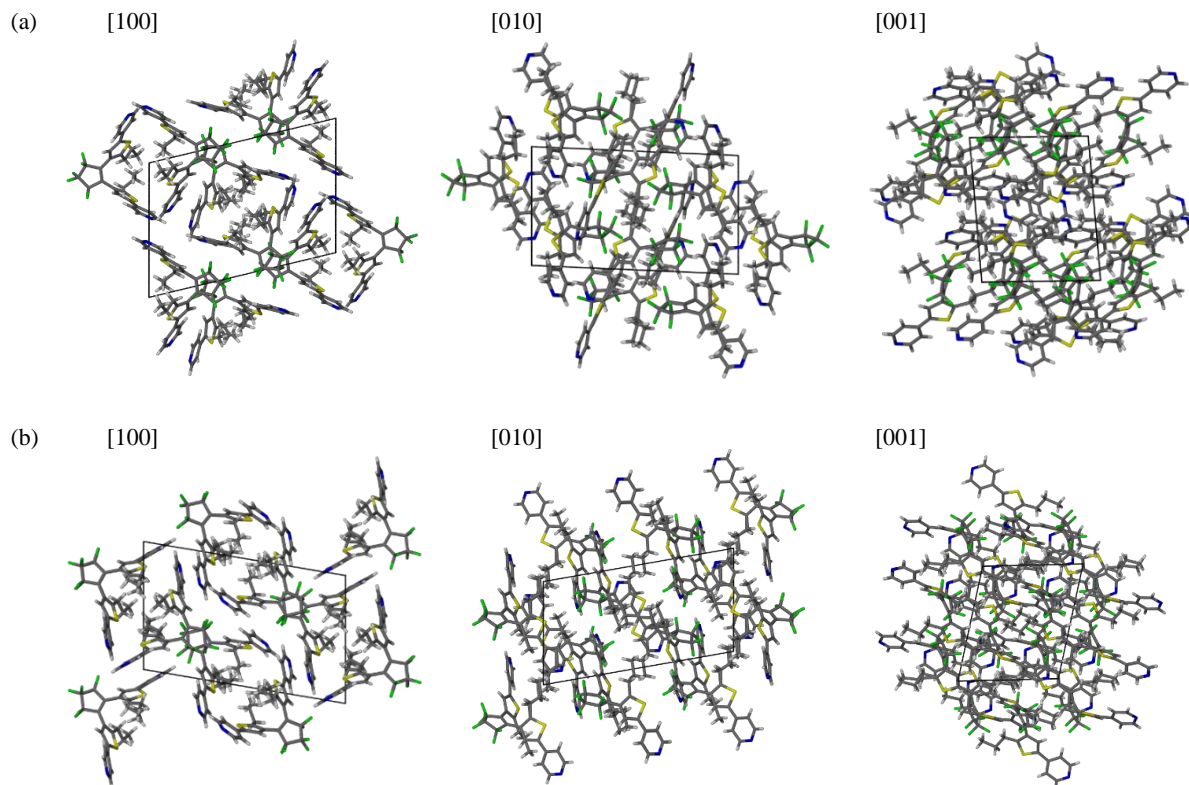


Figure 5-4: Molecular packing diagrams for the (a) **DA-1-[o]- $\alpha$**  phase and the (b) **DA-1-[o]- $\beta$**  phase

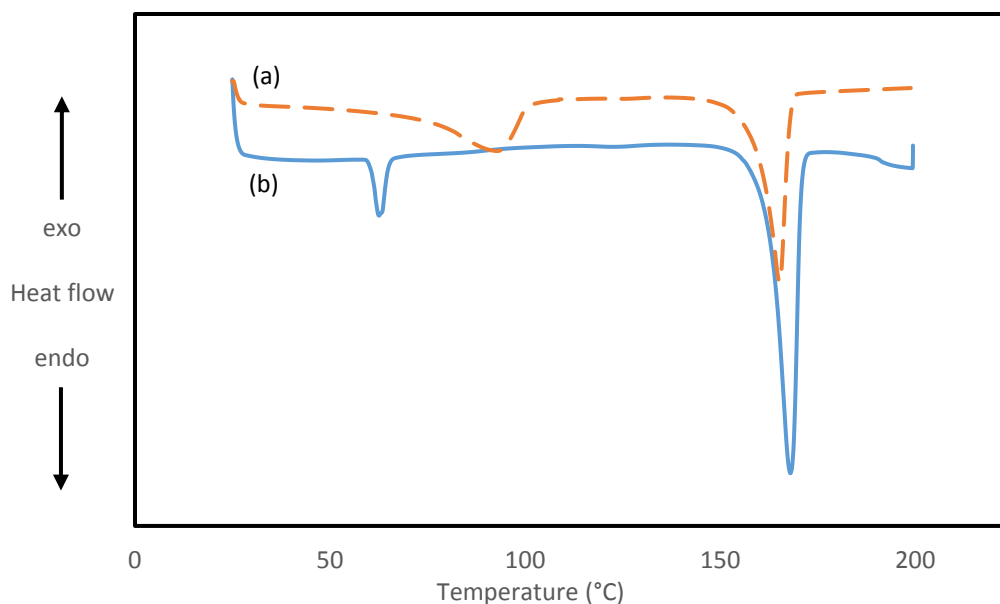


Figure 5-5: DSC for the (a) **DA-1-[o]- $\alpha$**  phase and the (b) **DA-1-[o]- $\beta$**  phase (only heating)

peak at 63 °C and another peak at 168 °C, which indicates the melting of the crystals. The similar melting points suggest that heating of both **DA-1-[o]- $\alpha$**  and **DA-1-[o]- $\beta$**  beyond their initial endothermic peaks result in the same phase.

The DSC experiment was repeated; however, instead of allowing the system to reach the melting point of the material, the temperature was cycled back after the first peak. This was done for the **DA-1-[o]- $\alpha$**  phase (Figure 5-6) as well as for the **DA-1-[o]- $\beta$**  phase (Figure 5-7). For the **DA-1-[o]- $\alpha$**  phase there is once again an endothermic peak at about 93 °C. Upon decreasing the temperature to room temperature there is an exothermic peak at 42 °C indicating another phase change. Increasing the temperature for the second cycle results in an endothermic

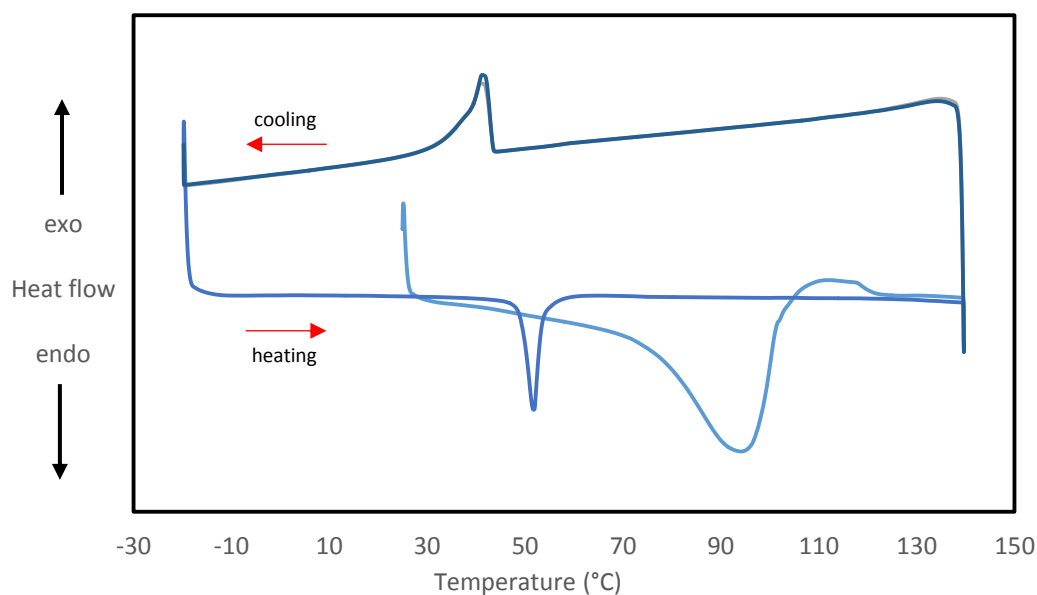


Figure 5-6: DSC for the **DA-1-[o]- $\alpha$**  phase (2 cycles of heating and cooling)

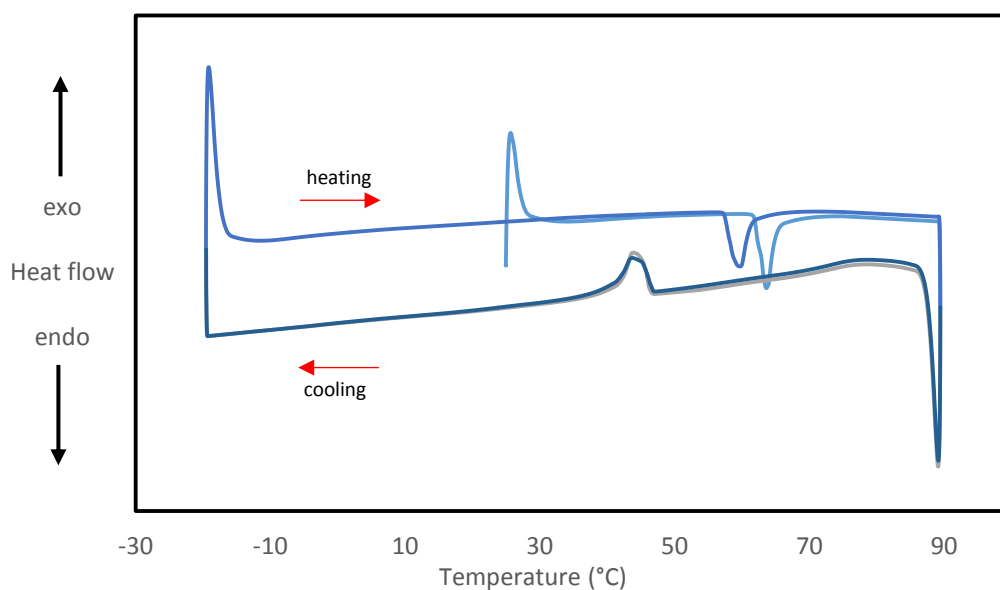


Figure 5-7: DSC for the **DA-1-[o]- $\beta$**  phase (2 cycles of heating and cooling)

peak at 52 °C, much earlier than the 93 °C from the first cycle. This suggests that the first cycle significantly altered the system, possibly inducing a phase change. Reducing the temperature to complete the second cycle once again results in an exothermic peak at 42 °C. The third cycle is indistinguishable from the second cycle and so it is assumed any recurring cycles will be the same.

For the **DA-1-[o]-β** phase the first peak once again appears at 63 °C. Upon cycling the temperature downwards, a peak appears at 45 °C. For the second cycle the first endothermic peak appears at 59 °C, slightly earlier than the 63 °C from the first cycle and upon return a peak once again appears at 45 °C. The fact that after the first cycle the **DA-1-[o]-α** phase behaves in much the same way as the **DA-1-[o]-β** phase suggests that it is converted to the **DA-1-[o]-β** phase after the first cycle. Furthermore since both showed similar melting points after undergoing the first phase change, this suggests the existence of a third phase that both **DA-1-[o]-α** and **DA-1-[o]-β** is converted to upon heating.

The phase changes were further investigated with variable temperature powder X-ray diffraction (VT-PXRD). For each phase the same cycle was followed as in the DSC (Figure 5-6 and Figure 5-7) while collecting powder patterns at particular points in the cycle. Starting from **DA-1-[o]-α** (Figure 5-9) three phases can be identified from the VT-PXRD experiment: The initial phase at the start of the experiment at room temperature undergoes a phase change at 120 °C indicated by the presence of a different powder pattern. This will be denoted as the **DA-1-[o]-γ** phase, since this is a different pattern from **DA-1-[o]-β** and thus has to be a new phase. The third identifiable phase is the **DA-1-[o]-β** phase, which occurs at room temperature after the first heating and cooling cycle. Upon heating again, the system returns to the **DA-1-[o]-γ** phase and after cooling once again returns to the **DA-1-[o]-β** phase. For **DA-1-[o]-β** (Figure 5-8) two phases could be identified; the **DA-1-[o]-β** phase at room temperature and the **DA-1-[o]-γ** phase at 70 °C, after the first endothermic peak. This phase change is repeated back and forth with further heating and cooling cycles.

The **DA-1-[o]-γ** crystals also show photochromic behaviour even at 120 °C (Figure 5-11). A **DA-1-[o]-β** crystal was placed on a hot-stage DSC and the temperature increased to 120 °C, far beyond the point at which the phase transition takes place. During this process a video was taken from which images were extracted. Upon reaching 120 °C the crystal was irradiated with UV light, at which point the crystal underwent a colourless-to-dark-blue conversion and under visible light reverted back to the colourless form. The structure of the **DA-1-[o]-γ** phase was elucidated by performing a variable temperature single crystal X-ray diffraction experiment. A crystal of **DA-1-[o]-β** was mounted on the X-ray diffractometer and

heated to 70 °C via the cryostat, at which point the **DA-1-[o]- $\gamma$**  diffraction data were collected. The temperature was decreased back to room temperature again, and the data recollected, confirming that the structure indeed evolves back to the **DA-1-[o]- $\beta$**  phase. The crystallographic data for the **DA-1-[o]- $\gamma$**  phase are summarised in Table 5-1 and the molecular packing diagram illustrated in Figure 5-10. Although there are still four molecules in the unit cell, the asymmetric unit now only consists of half a molecule. A similar experiment was attempted for a **DA-1-[o]- $\alpha$**  crystal by raising the temperature to 120 °C and collecting the

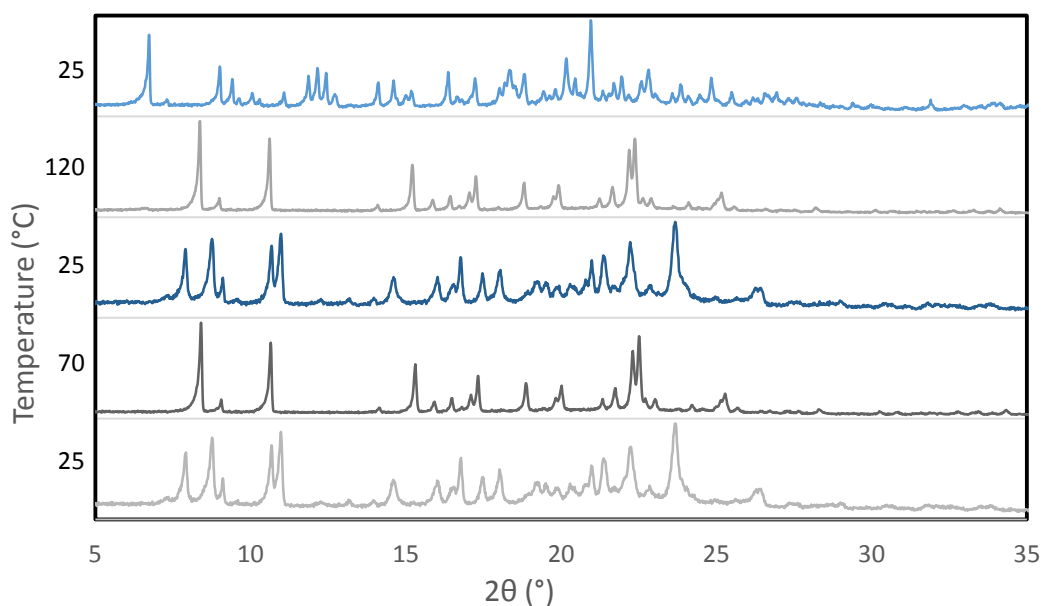


Figure 5-9: The temperature cycle is similar to Figure 5-6. Powder patterns were collected after each peak.

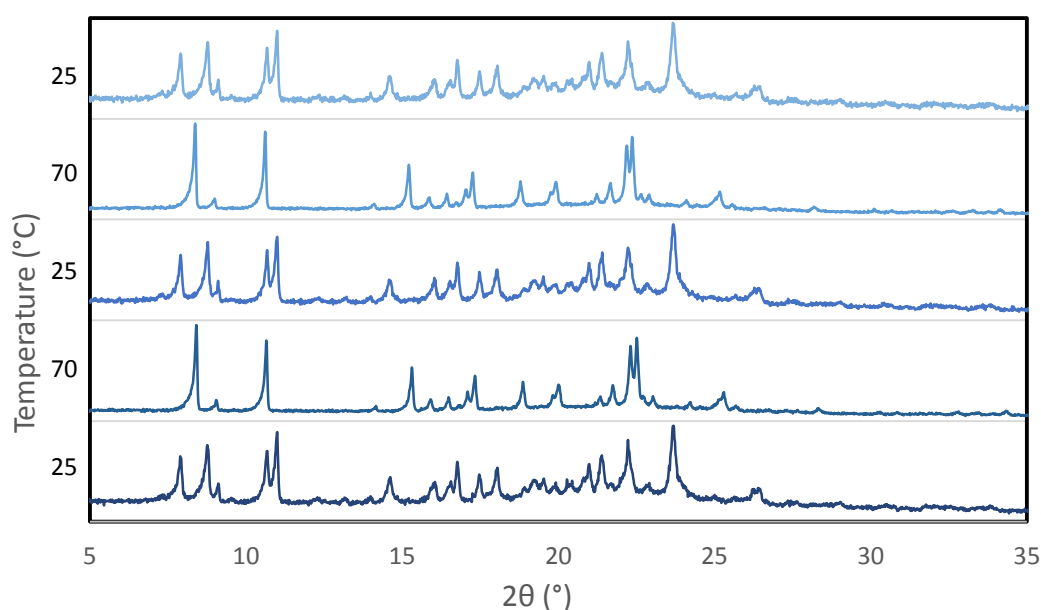
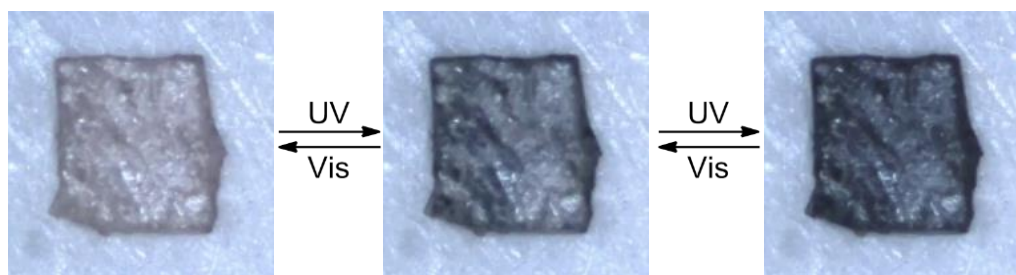
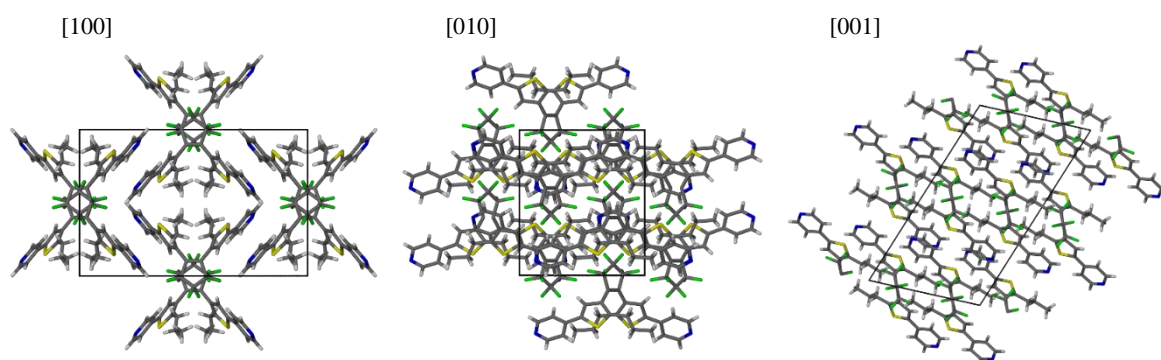


Figure 5-8: The temperature cycle is similar to Figure 5-7. Powder patterns were collected after each peak.

Figure 5-11: Photochromism of the **DA-1-[o]- $\gamma$**  phase at 120 °C.Figure 5-10: Molecular packing diagram for the **DA-1-[o]- $\gamma$**  phase.

X-ray diffraction data. However, it was not possible to solve the crystal structure, since the change undergone by the crystal was too large for the process to take place in a single-crystal-to-single-crystal fashion.

In order to confirm that the SCXRD data corresponds to the PXRD data, powder patterns were predicted from the crystal structures using Mercury (Figure 5-12). The predicted patterns for all three phases, **DA-1-[o]- $\alpha$** , **DA-1-[o]- $\beta$**  and **DA-1-[o]- $\gamma$** , are in very good agreement with the experimental powder patterns as shown in Figure 5-9 and Figure 5-8.

The thermodynamically preferred phase was established using both a computational and an experimental approach. The computational approach involved calculating the lattice energies for the two crystal structures. Lattice energies were calculated as follows:

$$E_{latt} = E_{cryst}/z - \sum_i E_{asu_i}$$

where  $E_{cryst}$  is the energy of the unit cell,  $z$  is number of asymmetric units in the unit cell and  $E_{asu_i}$  the energy of each molecule (for  $i = 1,2$ ) in the unit cell in vacuum.  $E_{latt}$  is the negative stabilisation energy per asymmetric unit, or, put differently, the increase in the negative potential energy as a result of the formation of the crystal structure. Energies were calculated with the DMol<sup>3</sup> module of Materials Studio using the PBE/PBE functional along with the DNP+ basis set (Double Numerical plus polarization, with the addition of diffuse functions). The

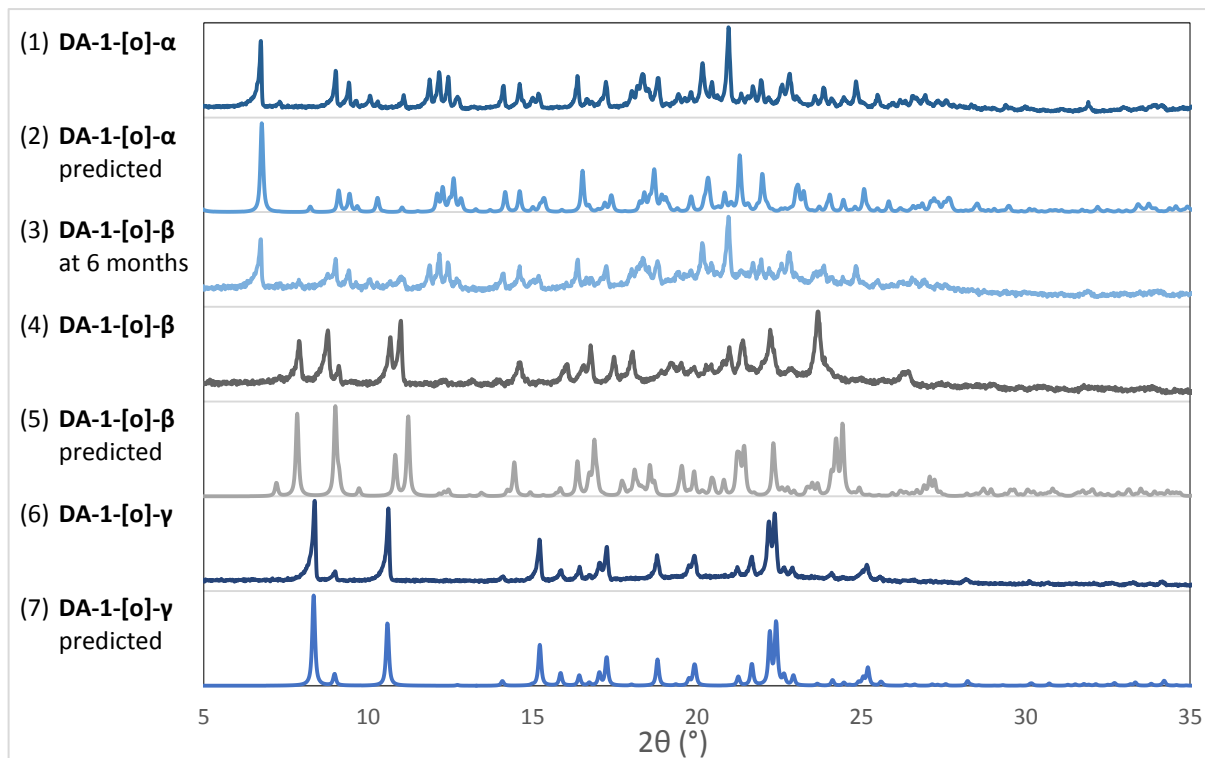


Figure 5-12: (1), (4) and (6): Experimental powder patterns of **DA-1-[o]- $\alpha$** , **DA-1-[o]- $\beta$**  and **DA-1-[o]- $\gamma$**  respectively. (2), (5) and (7) Predicted powder patterns of **DA-1-[o]- $\alpha$** , **DA-1-[o]- $\beta$**  and **DA-1-[o]- $\gamma$**  respectively, using Mercury. (3) was obtained by leaving a sample of **DA-1-[o]- $\beta$**  in a cupboard for a period of six months.

Tkatchenko-Scheffler (TS) method was used for the DFT dispersion correction. The  $E_{latt}$  values for both phases were calculated and the **DA-1-[o]- $\alpha$**  phase were found to be 36.71 kcal/mol, thus on average 18.36 kcal/mol per molecule, lower than that of the **DA-1-[o]- $\beta$**  phase. This suggests that the **DA-1-[o]- $\alpha$**  phase is the thermodynamically preferred phase. This was confirmed experimentally: A sample from each phase was left in a cupboard, at room temperature, for a period of six months after which a powder pattern was collected. The **DA-1-[o]- $\alpha$**  phase remained unchanged, with a powder pattern similar to that shown in Figure 5-12 (1) while the **DA-1-[o]- $\beta$**  phase converted to the **DA-1-[o]- $\alpha$**  phase, as is evident from the powder pattern in Figure 5-12 (3), confirming that **DA-1-[o]- $\alpha$**  is the thermodynamically preferred phase at ambient conditions.

## 5.4 Discussion

There is a large degree of similarity between the results obtained from this study and the study done by Kitagawa and Kobatake<sup>50</sup> on **DA-10**. Replacing the phenyl groups with pyridyl groups creates the possibility for the formation of much stronger interactions in the crystal as a nitrogen atom in a pyridyl ring has a lone pair of electrons and is more electronegative than a carbon atom from a phenyl ring.

The cell parameters and packing of the **DA-1-[o]- $\gamma$**  phase are very similar to the previously published **DA-10-[o]- $\beta$**  phase (Table 5-2 and Figure 5-13). This suggests that introducing the nitrogen atoms to the system results in strong interactions that alter the packing in such a manner as to adopt the **DA-1-[o]- $\beta$**  phase. Three close contacts that are shorter than the sum of the van der Waals radii of the respective atoms could be identified in **DA-1-[o]- $\beta$**  using the Close Contacts tool in Mercury. These include two N-H hydrogen bonds, which are 0.020 Å and 0.016 Å, shorter than the sum of the van der Waals radii of the atoms, as well as a nitrogen-fluorine close-contact, which is 0.021 Å shorter than the sum of the van der Waals radii. These interactions are not present in **DA-1-[o]- $\gamma$**  nor are there interactions involving the

Table 5-2: Crystallographic data for the **DA-10-[o]- $\alpha$**  and **DA-10-[o]- $\beta$**  phases.<sup>50</sup>

	<b>DA-10-[o]-<math>\alpha</math></b>	<b>DA-10-[o]-<math>\beta</math></b>
Formula	C <sub>31</sub> H <sub>26</sub> F <sub>6</sub> S <sub>2</sub>	C <sub>31</sub> H <sub>26</sub> F <sub>6</sub> S <sub>2</sub>
Formula weight	576.66	576.66
T [K]	303(2)	303(2)
Crystal system	Monoclinic	Monoclinic
Space group	<i>P</i> 2 <sub>1</sub> /c	<i>C</i> 2/c
<i>a</i> [Å]	11.765(5)	21.000(4)
<i>b</i> [Å]	19.985(7)	11.980(2)
<i>c</i> [Å]	13.298(6)	12.943(3)
$\alpha$ [°]	90	90
$\beta$ [°]	111.99(3)	115.058(4)
$\gamma$ [°]	90	90
Volume [Å <sup>3</sup> ]	2899(2)	2949.7(10)
Z	4	4
Density [g cm <sup>-3</sup> ]	1.321	1.298

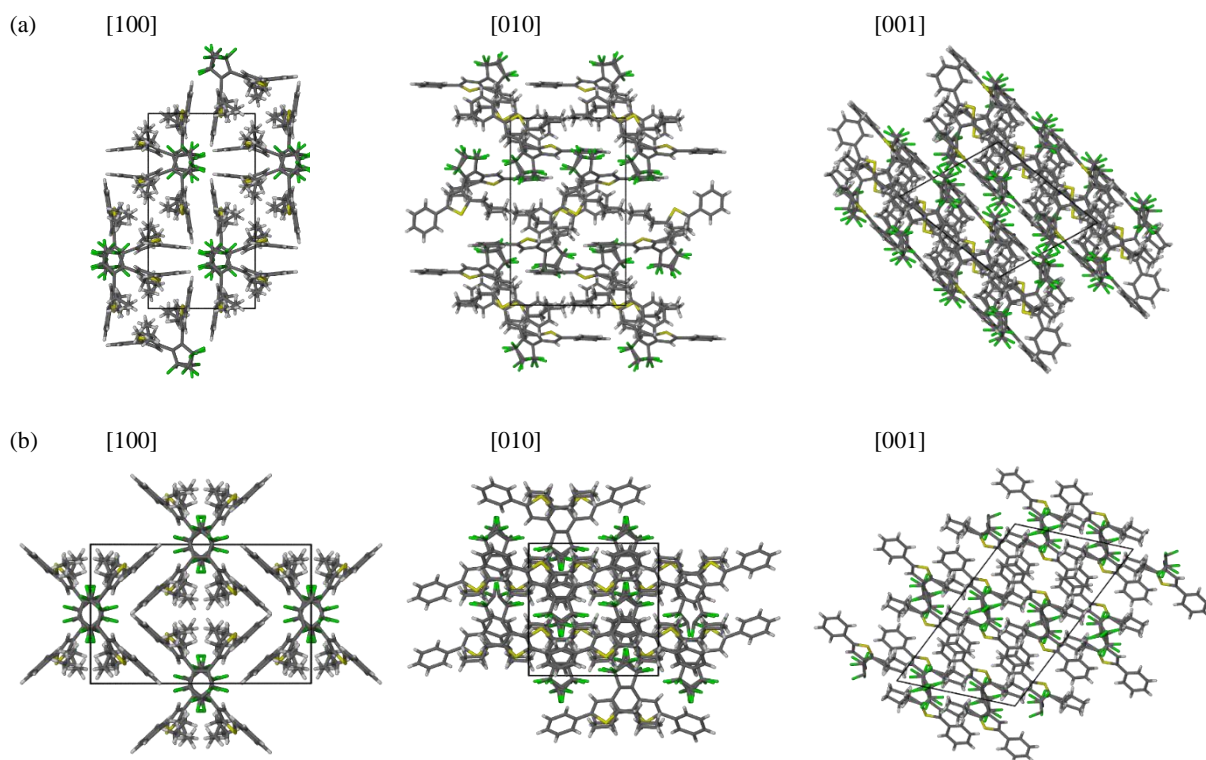


Figure 5-13: Molecular packing diagrams for the (a) **DA-10-[o]- $\alpha$**  and (b) **DA-10-[o]- $\beta$**  crystals from the study done on diarylethene **DA-10** (Figure 5-1).

corresponding carbon atoms in the **DA-10-[o]- $\beta$**  phase, suggesting that they play an important role in guiding the packing of the **DA-1-[o]- $\beta$**  phase. Nevertheless, these interactions are not strong enough to withstand the heating process. At 70 °C the interactions break, allowing a phase transition to take place leading to a packing arrangement that resembles that of the **DA-10-[o]- $\beta$**  phase, which does not exhibit these interactions.

## 5.5 Summary

The polymorphism of 1,2-bis(5-pyridyl-2-propyl-3-thienyl)perfluorocyclopentene (**DA-1-[o]**) was described using DSC, SCXRD and PXRD. Three phases were identified: one obtained from a polar solvent (**DA-1-[o]- $\alpha$** ), one from a non-polar solvent (**DA-1-[o]- $\beta$** ) and one that can be obtained by the heating of either of the other two phases until they undergo a phase transition. All polymorphic forms exhibit photochromic behaviour in the crystalline state as well as in powder form, undergoing a colour change upon irradiation with UV light. **DA-1-[o]- $\alpha$**  was identified as the thermodynamically preferred phase, which was confirmed both computationally and experimentally. The two phases are interconvertible: By fast heating above 120°C and cooling to room temperature the **DA-1-[o]- $\alpha$**  phase can be converted into the **DA-1-[o]- $\beta$**  phase whereas the **DA-1-[o]- $\beta$**  phase can be converted to the **DA-1-[o]- $\alpha$**  phase by leaving it in a cupboard at room temperature for a period of six months. The latter process is, however, too large to occur in a single-crystal-to-single-crystal fashion. The polymorphic behaviour is different to that of **DA-10-[o]**,<sup>50</sup> as the nitrogen atoms in the pyridyl rings were found to play a significant role in the packing of the **DA-1-[o]- $\beta$**  phase by introducing van der Waals interactions and hydrogen bonds to the system that are not present with the phenyl groups. These interactions are eliminated upon heating, allowing the system to evolve to the **DA-1-[o]- $\gamma$**  phase.

## Chapter 6: Photochromic behaviour of diarylethene crystals

During the study of the polymorphic phases of a diarylethene compound (Chapter 5), it was shown that diarylethenes also exhibit photochromic behaviour. Diarylethenes are a group of compounds of the form  $\text{Ar}-\text{C}=\text{C}-\text{Ar}$ ,<sup>29,41,42</sup> well known for undergoing a cyclisation reaction upon irradiation with UV light and the reverse under visible light. Since their discovery in 1967<sup>43</sup> these molecules have found interest in many fields due to their thermal irreversibility and resistance to fatigue, which are both indispensable properties in terms of application value.<sup>46</sup> Other properties that are important include sensitivity to external stimulus or light, response time and the reactivity in the crystalline or solid state.<sup>47-49</sup> In recent years diarylethene compounds have been identified that perform well in all of these categories.<sup>46</sup>

The photoisomerisation reaction can be illustrated as a reaction pathway similar to that shown in Figure 6-1, suggested by Robb et al.<sup>109</sup> The lower curve represents the ground state potential energy surface (PES) and has a high barrier with the transition state represented by  $\text{TS}_0$ . This barrier can, however, be overcome by moving to the excited state PES, represented by the upper curve, which has a smaller barrier that is easier to overcome,  $\text{TS}_1$ . The dotted arrows pointing from the lower to the upper curve represented the excitation of an electron from the ground to the excited state, while the dotted arrow pointing down represents the system returning to the ground state.

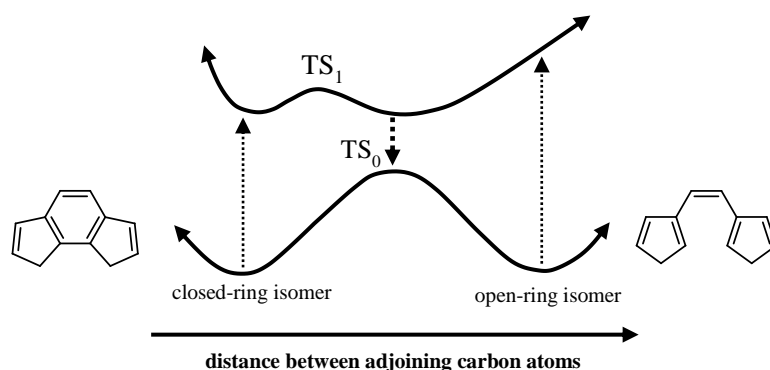


Figure 6-1: Reaction pathway for the photoisomerisation reaction of a typical diarylethene molecule.

Adapted from Robb et al.<sup>109</sup>

This reaction is, however, more complex than can be explained by a 1-dimensional drawing that does not provide information as to how the reaction will proceed mechanistically. Therefore, this study is aimed at providing a better understanding of the behaviour of the diarylethene molecule in the excited state. The thermal barrier in the excited state,  $\text{TS}_1$  (Figure 6-1), is explained as being a result of a conjugated  $\pi$  system extending over eight carbon atoms via the pentene bridge. This barrier slows down the reaction since additional energy is

required to reach the transition state and overcome the barrier. It can, however, be avoided if the system first undergoes a twisting action before the ring-opening proceeds.

Over the past 20 years a wide range of different diarylethene compounds have been synthesised and tested for their performance in the above-mentioned criteria. If a compound performs well it can be considered a good candidate for use in practical applications. Very little has been done, however, in terms of predicting how a specific molecule will perform in these categories. Therefore in this study a series of model compounds will be compared in order to study the effect that various structural modifications will have on the ring-opening or ring-closing reaction.

## 6.1 Aims and objectives

The aims of this study are twofold and the results will thus be presented in two sections. The aim within the first section is to develop a method for studying diarylethene compounds that allows for illustrating the photoisomerisation reaction in a single graphical illustration that is simple to understand. This will then be used to provide a fundamental explanation for the diarylethene photoisomerisation reaction. The aim of the second section is to use this method to illustrate and explain how various structural modifications will affect the diarylethene ring-closure or ring-opening ability.

## 6.2 Methods

The Gaussian 09 program was used for this study. Density Functional Theory (DFT) methods were used for carrying out optimisations, scans and calculating frequencies at the minimum energy structures. Time-Dependent DFT was used for calculating excited state energies.

In the first section a model compound, **DA-2** (Figure 6-2) is used to develop a new method for explaining the diarylethene ring-closure and ring-opening reactions. Different levels of theory were used at different steps in the process and will be given in the relevant sections. For the final calculation of excited state energies with TD-DFT, B3LYP-D3 along with the 6-311++G basis set was used. A Gaussian-type basis set was always selected in such a manner as to find the best balance between accuracy and computational cost.

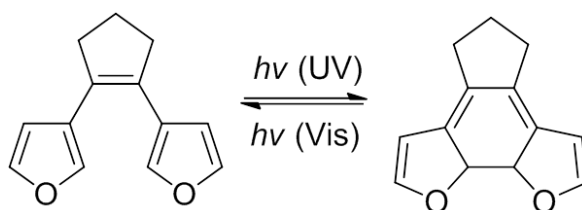


Figure 6-2: Difurylcyclopentene, **DA-2-[o]** (left), and its ring-closed form, **DA-2-[c]** (right).

The process involves a series of scans between a ring-opened and a ring-closed structure and thus as a convention all scans were initiated from the ring-closed structure and scanned in the direction of the ring-opened structure. The same results were obtained when the scan was done in the opposite direction.

Optimising geometries in the excited state using TD-DFT is computationally very expensive, to such a point as to make this procedure unfeasible. Therefore it was assumed that the excited state geometry of each step in a scan is ‘close enough’ to the triplet state geometry and a much better approximation to using the singlet ground state geometries. This can be rationalised by considering Figure 6-3. Since the ring-closure and ring-opening reactions is due to an excitation from the HOMO to the LUMO, the only difference between the triplet state and the singlet excited state is the spin of the electron in the LUMO.

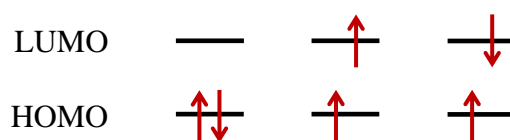


Figure 6-3: In order from left to right: Ground state, Triplet state, Singlet excited state

In the second section this same method was applied to a range of model compounds, of which the types of variations are illustrated in Figure 6-4, in order to study the effect that various structural modifications will have on the photoisomerisation reaction. The same level of theory as above was used throughout this study, except where mentioned otherwise.

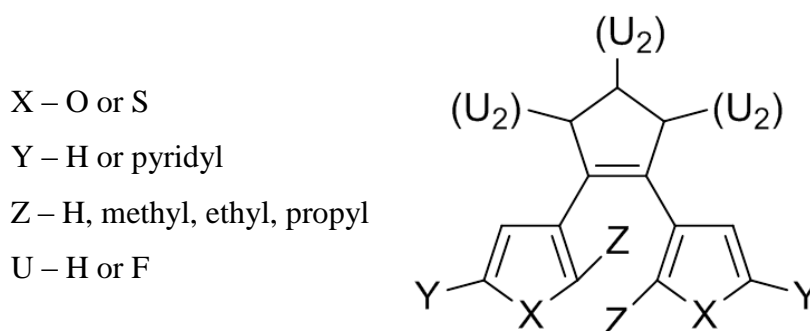


Figure 6-4: Various combinations of U, X, Y and Z were made in order to create model compounds. This series of molecules are also displayed in the overall methodology (section 3.1.2.2).

In this study a large number of input files were created for submission to the Gaussian 09 program. The relevant data were then extracted from the large number of log files that were generated so that they could be presented in a logical manner. Bash shell scripting was used within the Linux terminal for creating and extracting the data and the OriginPro program for creating graphical illustrations. Some of the most important shell scripts are included in the supplementary information.

### 6.3 The diarylethene photoisomerisation

As previously mentioned, **DA-2** was used as a model compound because it is simple, but still contains the basic carbon backbone essential for describing the ring-closure or ring-opening reaction. The mechanism for the reaction can be determined by identifying the lowest-energy pathway from the initial to the final structure. In this study this was done by carrying out scans of all bond distances, angles and dihedral angles for which there are significant differences between the structures of the reactant and product. Since a Lewis diagram does not illustrate the true sizes of angles, it is easy to disregard the importance of angles. A change in an angle or dihedral angle can, however, result in the breaking or formation of  $\pi$  bonds, which has a significant effect on the stabilisation energy of the system; thus angles and dihedral angles also need to be scanned in order to identify a reaction pathway.

#### 6.3.1 Identifying major parameter differences

Both the ring-closed and ring-opened structures were optimised in the ground state and in the gas phase at the B3LYP-D3/6-311++G(d,p) level of theory. Three major differences could be identified between the two structures. These are illustrated in Figure 6-5 and labelled as bond distance  $d_1$  varying from 1.494 Å to 3.400 Å, dihedral angle  $\theta_1$  (from 172.84° to 139.93°) and dihedral angle  $\theta_2$  (from 173.32° to 146.84°). Thus for the purpose of identifying a reaction pathway all three of these parameters were scanned.

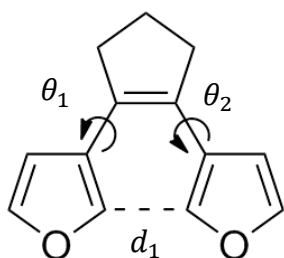


Figure 6-5: The parameters with significant differences between the ring-closed and ring-opened structures are labelled  $\theta_1$ ,  $\theta_2$  and  $d_1$ .

Table 3: Differences in bond distances and angles (see Figure 6-5)

Parameter	Ring-closed	Ring-opened
distance $d_1$	1.494 Å	3.400 Å
dihedral angle $\theta_1$	172.84°	139.93°
dihedral angle $\theta_2$	173.32°	146.84°

#### 6.3.2 Scanning all the major parameters

A scan over only the two dihedral angles was carried out, at the B3LYP/6-31G level of theory. Each angle was evenly divided into 32 scan points, starting and ending with their respective initial and final values, while keeping  $d_1$  fixed at a distance of 1.494 Å as this parameter will

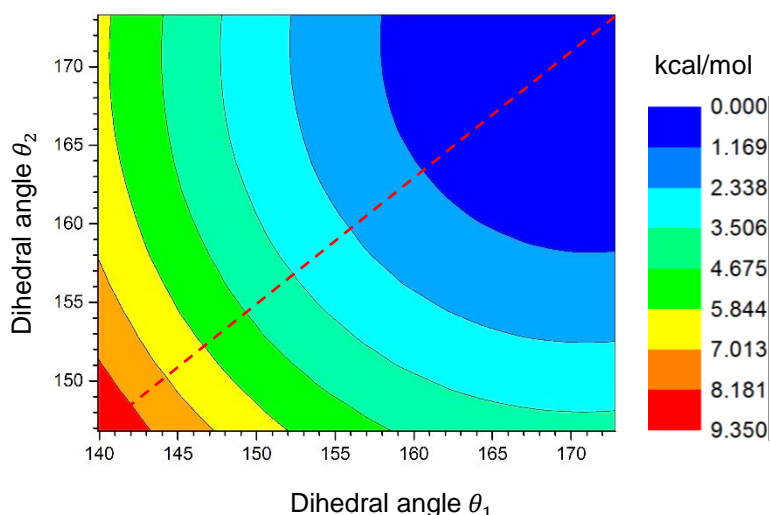


Figure 6-6: Dihedral angles scanned from the ring-closed (top-right) to the ring-opened (bottom-left) form with distance  $d_1$  fixed at the distance for the ring-closed form (1.494 Å). Energies in kcal/mol.

be scanned later. The energies for the 1024 scan points are illustrated in Figure 6-6, relative to the lowest energy point, which is the energy for the ring-closed structure. The line of steepest descent falls almost exactly on the diagonal of the graph, which suggests that the twisting of the two dihedral angles happen in a synchronous manner even though they start and finish at different values. This is very useful since it allows the three parameters describing the reaction coordinate to be reduced to two by considering the dihedral angles as a single parameter to be scanned.

In order to scan the distance  $d_1$  a set of 32 structures represented by the scan points on the diagonal of Figure 6-6 (the red-dotted line) were generated. Each structure, labelled 1 to 32, has two fixed dihedral angles, with angles  $\theta_1$  and  $\theta_2$  in structure 1 corresponding to the ring-closed structure and in 32 to the ring-opened structure. For each of these starting geometries the distance  $d_1$  was scanned from 1.494 Å to 3.400 Å with 32 scan steps. The dihedral angles were kept constant during this procedure. The scan was done in the triplet state using the UB3LYP-D3 functional with the 6-311++G basis set. In an initial scan in the singlet state the system underwent an unrealistic twisting action that did not result in the correct final product, hence the triplet state was used for the calculations. Once the 1024 geometries from the triplet state scan were obtained the singlet ground state energies were also calculated. These are illustrated in Figure 6-7 (a) and (b) respectively and combined in Figure 6-7 (c).

The bottom-left corners, of Figure 6-7 (a) and (b), represent the ring-closed structure while the top-right corners represent the ring-opened structure. The reaction pathway to be identified must, therefore, connect these two points. In the areas bounded by the blue dotted

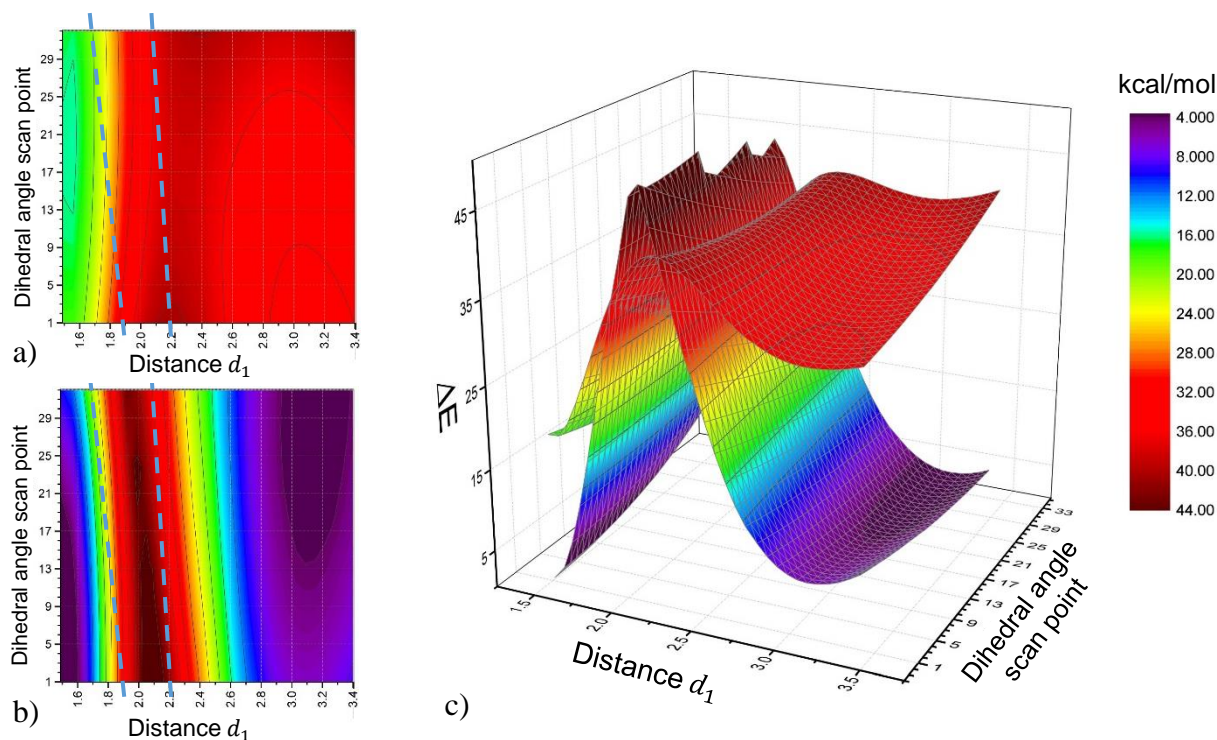


Figure 6-7: a) Triplet state, b) Singlet state and c) combined energies (kcal/mol) for each of the 1024 geometries.

lines the triplet state of the system is lower in energy than the singlet state. This allows the system to undergo a transition between **DA-2-[c]** and **DA-2-[o]** via a lowered thermal barrier whilst moving from the singlet to the triplet and back to the singlet state.

### 6.3.3 Excited state potential energy surfaces

The vertical excitation energies were calculated separately for each of the 1024 triplet state geometry points. This was done using TD-DFT at the B3LYP-D3/6-311++G level of theory. The desired excited state energies were then added to the singlet ground state energies previously calculated and combined to produce an excited state potential energy surface (PES) map. The results are illustrated in Figure 6-8 as the difference in energy.

The excited state energy map, indicated by **a<sub>2</sub>**, forms a cusp where it crosses over to the ground state energy map, indicated by **a<sub>1</sub>**. This point or line where the excited and ground states connect is called a conical intersection.<sup>110</sup> Moving beyond this point results in a crossing of states, which means that the electronic system changes its state (from singlet excited to ground state) as a result of vibronic coupling. Thus the excited state PES becomes the ground state PES and vice versa. The exact line where this crossing of states takes place is not shown since DFT is erroneous at calculating energies at these points of crossing and thus gives distorted energy values. This is because the Born–Oppenheimer approximation breaks down at conical

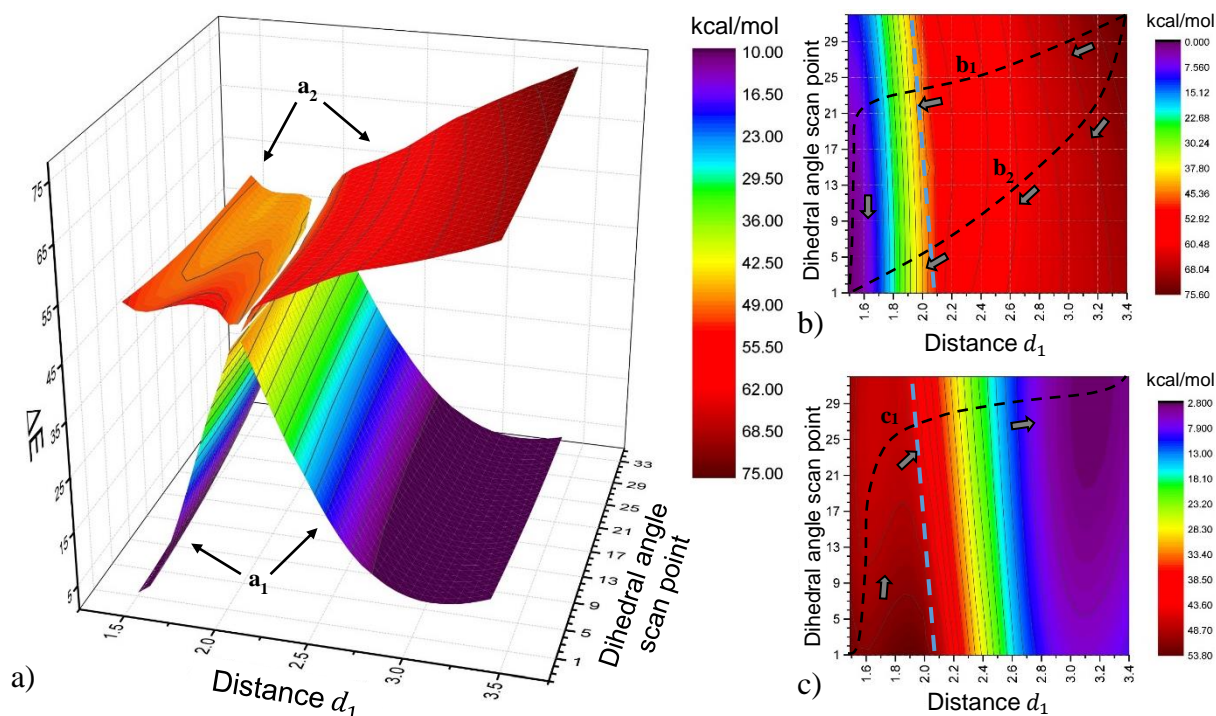


Figure 6-8: a) Both potential energy surfaces combined in a 3-D representation with  $\mathbf{a}_1$  as the ground state and  $\mathbf{a}_2$  the excited state. b) PES corresponding to the ring-closure reaction, c) PES corresponding to the ring-opening reaction,  $\mathbf{b}_1$ ,  $\mathbf{b}_2$  and  $\mathbf{c}_1$  represents possible reaction pathways. The blue dashed line represent the crossing of states. Energies in kcal/mol.

intersections since the coupling between electronic and nuclear motion becomes important. Thus there is a gap between the left and right side of the excited state PES ( $\mathbf{a}_2$ ). The two potential energy surfaces can now be separated by combining the left side of  $\mathbf{a}_2$  with the right side of  $\mathbf{a}_1$  and vice versa to produce Figure 6-8 (b) and (c). These two potential energy surfaces can be used to explain the diarylethene ring-closure and ring-opening reactions, respectively, as will be discussed in the subsequent sections.

### 6.3.4 Ring-closure reaction

The point at the top right-hand corner of Figure 6-8 (b) represents the energy of the ring-opened structure after excitation of an electron from the HOMO to the LUMO (Figure 6-9). There is a similarity between the excited state energies and that of the LUMO with the downward energy gradient always moving away from either the ring-opened or ring-closed structure and towards the conical intersection. Within Figure 6-8 (b) there is a

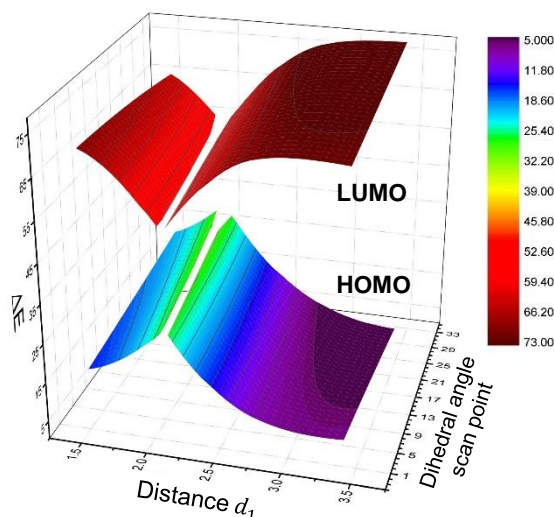


Figure 6-9: 3-dimensional representation of the HOMO and LUMO surfaces.

downward energy gradient towards the ring-closed structure (at the bottom left of the graph) with the gradient being steepest when moving to the left, following the estimated reaction path **b<sub>1</sub>** on Figure 6-8 (b). This steeper gradient suggests that the closing of the ring (decreasing distance  $d_1$ ) dominates the reaction at this point. At a distance of about 2.0 Å the system reaches the conical intersection, indicated by the blue dashed line, after which the system reverts back to the ground state. Once the closing of the ring is almost complete, the twisting of the dihedral angles becomes the dominant part of the reaction and proceeds until the reaction is completed. However, since there is no thermal barrier preventing the reaction from following a path similar to **b<sub>2</sub>**, the reaction might just as well proceed in such a manner depending on the rate of the two structural changes during the ring-closing reaction.

### 6.3.5 Ring-opening reaction

The point at the bottom left corner of Figure 6-8 (c) represents the energy of the ring-closed structure after excitation of an electron from the HOMO to the LUMO. The reaction path **c<sub>1</sub>** represents the likely direction in which the reaction will proceed with a downward energy gradient towards the ring-opened structure. Starting from the bottom left corner, upon increasing the distance  $d_1$  there is a thermal barrier of about 2 kcal/mol prohibiting the reaction from proceeding in that direction. Instead there is a downward energy gradient when moving upwards on the graph accompanied by the twisting of the dihedral angles. The thermal barrier decreases as the dihedral angles are twisted further until it is small enough to be overcome. At this point the system once again undergoes a crossing of states and returns to the ground state. The reaction now proceeds with an increase in distance  $d_1$  until the reaction is completed.

### 6.3.6 Conical intersection and the crossing of states

An essential part in understanding the mechanism of the diarylethene reaction involves modelling the conical intersection, since this is the point where an electron is allowed to move back to the ground state without having to emit light. Modelling the conical intersection, however, requires the system to be optimised in the excited state near and at the point of crossing, which cannot be done with TD-DFT and thus requires more involved methods such as CASSCF.<sup>109</sup> At the conical intersection the HOMO and LUMO also exchange, with the HOMO now becoming the LUMO and vice versa, similar to what is shown in Figure 6-8. If the system is not optimised in the excited state, however, the energies of the HOMO and LUMO are further away from one another leaving a gap between the ground and excited states, preventing the system from returning to the ground state due to vibronic coupling.

To further emphasise the importance of modelling the system in the excited state, each of the 1024 geometries were optimised in the singlet ground state using the same level of theory as before, whilst constraining the dihedral angles  $\theta_1$  and  $\theta_2$  and the distance  $d_1$  at each geometry point. Thereafter the excitation energies were calculated, added to the ground state energies and combined to form an excited state PES map. The results are illustrated in Figure 6-10 relative to the lowest calculated energy and labelled as (a) the excited state PES of the geometries that were optimised in the singlet state, (b) the excited state PES of the geometries that were optimised in the triplet state, (c) the ground state PES of the geometries that were optimised in the triplet state and (d) the ground state PES of the geometries that were optimised in the singlet state.

During the optimisation in the singlet state, small but cumulative changes within the molecule result in the separation of the ground and excited state potential energy surfaces (Figure 6-10). The excited state PES shifts to higher (a) and the ground state PES to lower (d) energies. After the optimisation in the singlet state the conical intersection is not present anymore since there is a separation between the excited and ground state. Thus if the system were to adopt this set of geometries it will not be able to evolve from the excited to the ground

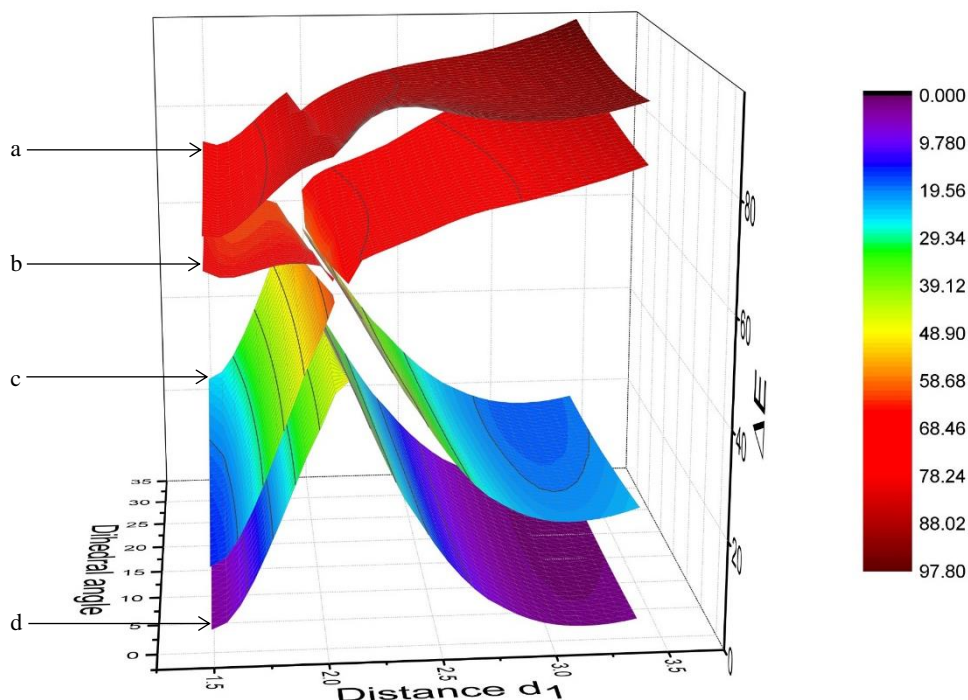


Figure 6-10: a) Excited state and d) ground state energies for geometries that were optimised in the singlet state.

b) Excited state and c) ground state energies for geometries that were optimised in the triplet state.

state, due to vibronic coupling, since the energy gap is too large. For the geometries optimised in the triplet state, however, the ground (c) and excited (b) states meet at the conical intersection. Thus for this set of geometries the system will be able to evolve from the excited to the ground state, at the point of intersection, due to vibronic coupling. Therefore (b) provides a better description than (a) of how the system will behave in the excited state since the energies at the conical intersection are low enough and the gap between (b) and (c) small enough for the system to undergo a change in state. Furthermore (c) provides a better description of the system at the conical intersection since the energies are high enough to intersect with (b), however, once the system has reached the singlet ground state, it will adopt a singlet ground state geometry, which is represented by potential energy surface (d).

## 6.4 Influence of structural modifications on photoisomerisation

A series of model diarylethene compounds were studied (Figure 6-11) to determine the effect of various structural modifications on the ring-closure and ring-opening reactions. For simplicity only the ring-opened forms of the compounds are displayed in Figure 6-11 to Figure 6-20. In order to understand what effect a specific structural variation will have on the photoisomerisation reaction, the rest of the system was kept constant while only making that specific variation on the system. Thus a set of compounds was selected in such a way as to study five types of structural modifications. Within Figure 6-11 an arrow represents an opportunity for making a comparison between two structures and the letters **a** to **e** refer to a specific type of structural modification. Thus, for example, in order to understand how the

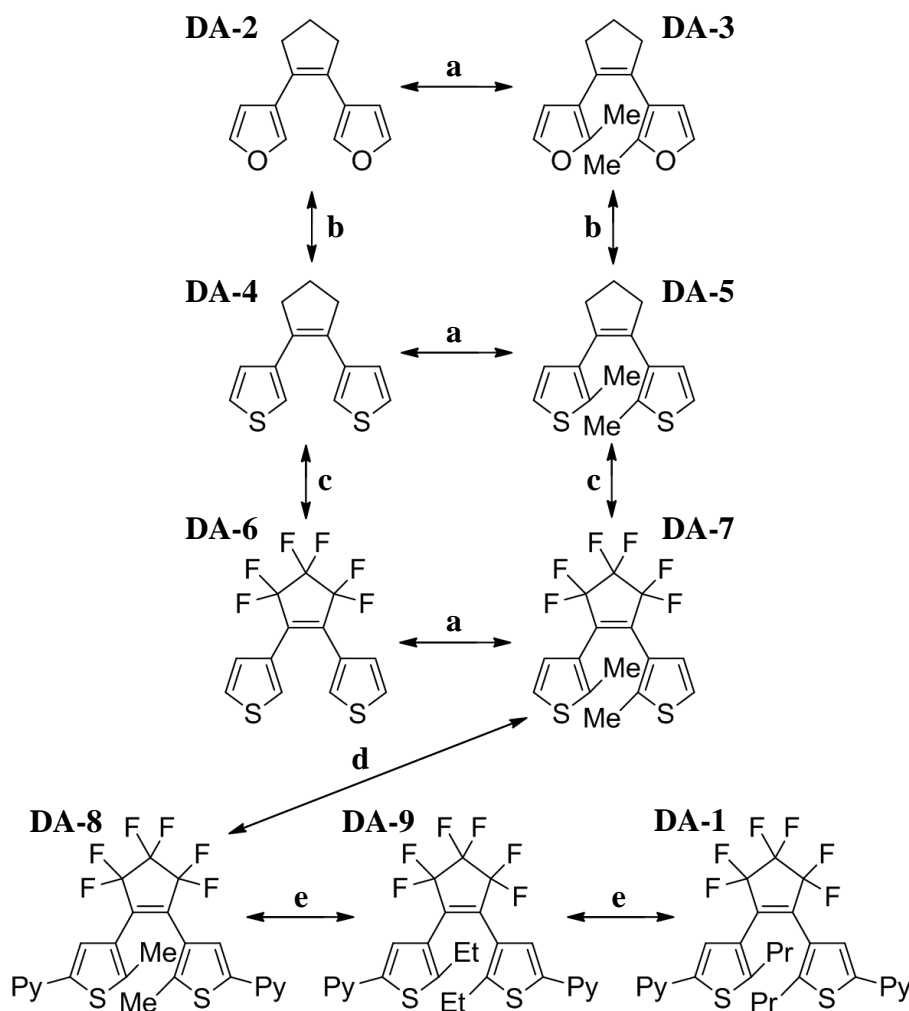


Figure 6-11: Model compounds that were studied with the method used in Sections 6.3.2 and 6.3.3. Arrows **a** to **e** refers to a specific type of structural modification with **a** referring to the addition of methyl groups, **b** to the replacement of oxygen atoms with sulphur atoms, **c** to the addition of fluorine atoms on the cyclopentene ring, **d** to the addition of pyridyl rings and **e** to an increase in the hydrocarbon chain.

introduction of methyl groups will affect the reaction one must consider arrows marked with **a**. Similarly **b** refers to the replacement of oxygen atoms with sulphur atoms, **c** to the addition of fluorine atoms on the cyclopentene ring, **d** to the addition of pyridyl rings and **e** to an increase in the hydrocarbon chain length.

Crystal structures of a few of these compounds have been published and are available in the CSD. The initial geometries for the first optimisation step of the ring-opened and ring-closed forms were therefore either taken from experimental data or adapted from the nearest counterpart for those compounds for which structural data was not available in the CSD. The structure of the final compound in the series, **DA-1**, was presented in Chapter 5.

The same procedure that was followed in Sections 6.3.2 and 6.3.3 was applied to the series of compounds in Figure 6-11. The results are illustrated in Figures 6-12 to 6-20 as well as in Table 6-4, which contains some of the most important values extracted from the calculations. The comparison will be done while taking into consideration the five requirements that photochromic molecules need to fulfil in order to be considered of practical value:<sup>103</sup> 1) thermal stability of both isomers, 2) fatigue resistance, 3) high sensitivity to external stimulus, 4) rapid response to stimulus and 5) reactivity in the solid state. This study, however, only provides some information as to the thermal stability and response to stimulus with the other factors (2, 3 and 5) being much harder to predict computationally.

Table 6-4: Energies extracted from Figures 6-12 to Figures 6-20 for the series of compounds. <sup>a</sup> $\Delta E$  (kcal/mol) between ring-closed and ring-opened structures. <sup>b</sup>Size of initial energy barrier that needs to be overcome by twisting the dihedral angles. <sup>c</sup>Excitation energy (nm) for ring-opened form. <sup>d</sup>Excitation energy (nm) for ring-closed form. Calculations done at the B3LYP-D3/6-311++G level of theory.

Compound	$\Delta E$ (kcal/mol) <sup>a</sup>	Barrier height <sup>b</sup>	[o] excitation energy <sup>c</sup>	[c] excitation energy <sup>d</sup>
<b>DA-2</b>	6.0	2.21	297	414
<b>DA-3</b>	13.1	4.61	268	433
<b>DA-4</b>	6.7	7.05	312	454
<b>DA-5</b>	14.6	11.49	287	492
<b>DA-6</b>	8.6	7.41	329	490
<b>DA-7</b>	16.6	11.66	321	539
<b>DA-8</b>	15.3	15.55	347	635
<b>DA-9</b>	18.3	13.31	347	678
<b>DA-1</b>	19.3	13.11*	348	680

\* Calculated using the 6-311G basis set.

The energy difference between the ring-closed and ring-opened structures (Table 6-4) provides a measure of thermal stability, with a larger positive difference suggesting that the closed form is thermodynamically less preferred. There are two factors that influence the response to external stimulus. The first is the energy difference between the ring-closed and ring-opened forms, which is important because once the system reaches the conical intersection and returns to the ground state it can move in the direction of either the ring-closed or ring-opened forms. If one state is, however, thermodynamically preferred, the reaction tends towards that state. Therefore the reaction is favoured in one direction and disfavoured in the other. The other factor is the barrier height. It was shown in the previous section that in order for the ring-opening to occur a thermal barrier in the excited state needs to be overcome. This is achieved by the twisting of the dihedral angles to bypass the thermal barrier allowing the ring-opening reaction to proceed. This can be seen in Figures 6-12 (b) to 6-20 (b). The size of the barrier is determined by measuring the maximum energy difference when starting at the bottom-left of the illustration, and moving in right direction, thus keeping the dihedral angles constant, and only increasing the distance  $d_1$ . These two factors thus influence the response to external stimulus.

The excitation energies for both the open form [**o**] (resulting in ring closure) and the closed form [**c**] (resulting in ring opening) are also listed in Table 6-4. A larger separation between these two values also provides better control over which state the system is in since this allows the reaction to be driven forward in one direction, with the given wavelength of light, without influencing the reverse reaction. All the changes that were introduced resulted in a larger separation between the excitation energy required for the ring-opened and ring-closed forms.

The introduction of two methyl groups resulted in an increase in the energy difference between the ring-closed and ring-opened forms (Table 6-2) from 6.0 to 13.1, 6.7 to 14.6 and from 8.6 to 16.6 kcal/mol upon going from compounds **DA-2** to **DA-3**, **DA-4** to **DA-5** and from **DA-6** to **DA-7** respectively. This suggests that the methyl groups decrease the thermal stability of the ring-closed form making the ring-opened form more preferred. This implies that the inclusion of a methyl substituent leads to a better response to stimulus for the ring-opening reaction since the ring-opened form is thermally preferred. However, the initial barrier to ring-opening also increases from 2.21 to 4.61, from 7.05 to 11.49 and from 7.41 to 11.66 kcal/mol. This suggests the opposite from what was just mentioned, that the ring-opening reaction will have a slower response to stimulus. The response to stimulus can be increased by heating which would aid in the overcoming of the thermal barrier in the excited state.

Upon considering graphs shown in Figures 6-12 (a) to 6-17 (a), one can see that the introduction of the methyl groups increases the asynchronicity of the ring-closure reaction. Consider for example Figures 6-16 and 6-17 for compounds **DA-6** and **DA-7**, respectively. Starting from the ring-opened structure of **DA-6**, upon twisting the dihedral angles, whilst keeping the distance  $d_1$  constant, a decrease in energy is observed ( $b_2$  from Figure 6-16). Doing the same for **DA-7**, however, results in an increase in energy ( $b_2$  from Figure 6-17). Thus the system is forced to first shorten the distance  $d_1$ , until it reaches the conical intersection, at which point the dihedral angles can twist more until the completion of the reaction. The introduction of the methyl groups is also crucial to the fatigue resistance of the compound since dihydrogen elimination could readily take place if the methyl groups were not present.

In order to study the effect of replacing the furyl groups with thienyl groups we consider the compounds related by change **b** in Figure 6-11. The difference in energy between the ring-closed and ring-opened structures increases from 6.0 to 6.7 and from 13.1 to 14.6 kcal/mol upon going from compounds **DA-2** to **DA-4** and from **DA-3** to **DA-5** respectively, suggesting only a slight decrease in the preference for the ring-closed structure. The initial barrier to ring-opening increases from 2.21 to 7.05 and from 4.61 to 11.49 kcal/mol suggesting that the ring-closed form will be less responsive to light since there is a larger thermal barrier that needs to be overcome for the ring-opening reaction to proceed.

We consider the changes indicated by **c** in Figure 6-11 to study the effect of adding fluorine atoms onto the pentene ring. The energy difference between the ring-closed and ring-opened forms increases from 6.7 to 8.6 and from 14.6 to 16.6 kcal/mol upon going from compounds **DA-4** to **DA-6** and from **DA-5** to **DA-7**, suggesting a decrease in the stability of the ring-closed form with the ring-opened form being more thermodynamically preferred. The initial barrier to ring-opening increases slightly in both cases from 7.05 to 7.41 and from 11.49 to 11.66 kcal/mol suggesting that the fluorine atoms does not affect the ring-opening ability.

Next we will consider the changes indicated by **d** in Figure 6-11 in order to investigate the effect of a pyridyl group. Upon going from compound **DA-7** to **DA-8** there is a slight decrease in the energy difference between the ring-closed and ring-opened structures, from 16.6 to 15.3 kcal/mol. The initial barrier to ring-opening increases greatly from 11.66 to 15.55 kcal/mol. The pyridyl ring adds more p-electrons to the conjugated  $\pi$ -system, which stabilises the ring-closed form. This also results in a higher thermal barrier in the excited state due to the increased stability of the conjugated  $\pi$ -system. Considering Figure 6-19 (compound **DA-8**), however, one can observe that even though there is a higher initial barrier, the barrier falls off faster than for **DA-7** in Figure 6-18. Thus even though there is a larger

initial barrier to ring-opening, a similar amount of twisting is required to overcome the barrier and so the ring-opening will proceed in a similar manner as to **DA-7**.

Lastly, changes indicated by **e** represents an increasing the length of the hydrocarbon chain on carbon atoms 2 and 5 of the thiophene rings. Upon going from **DA-8** to **DA-9** to **DA-1** there is an increase in the energy difference between the ring-closed and ring-opened forms, from 15.3 to 18.3 to 19.3 kcal/mol. This suggests that a longer hydrocarbon chain length results in a more destabilised ring-closed form, which could be due to steric hindrance. The initial barrier to ring-closure decreases from 15.55 to 13.31 to 13.11 kcal/mol suggesting better reactivity to external stimulus.

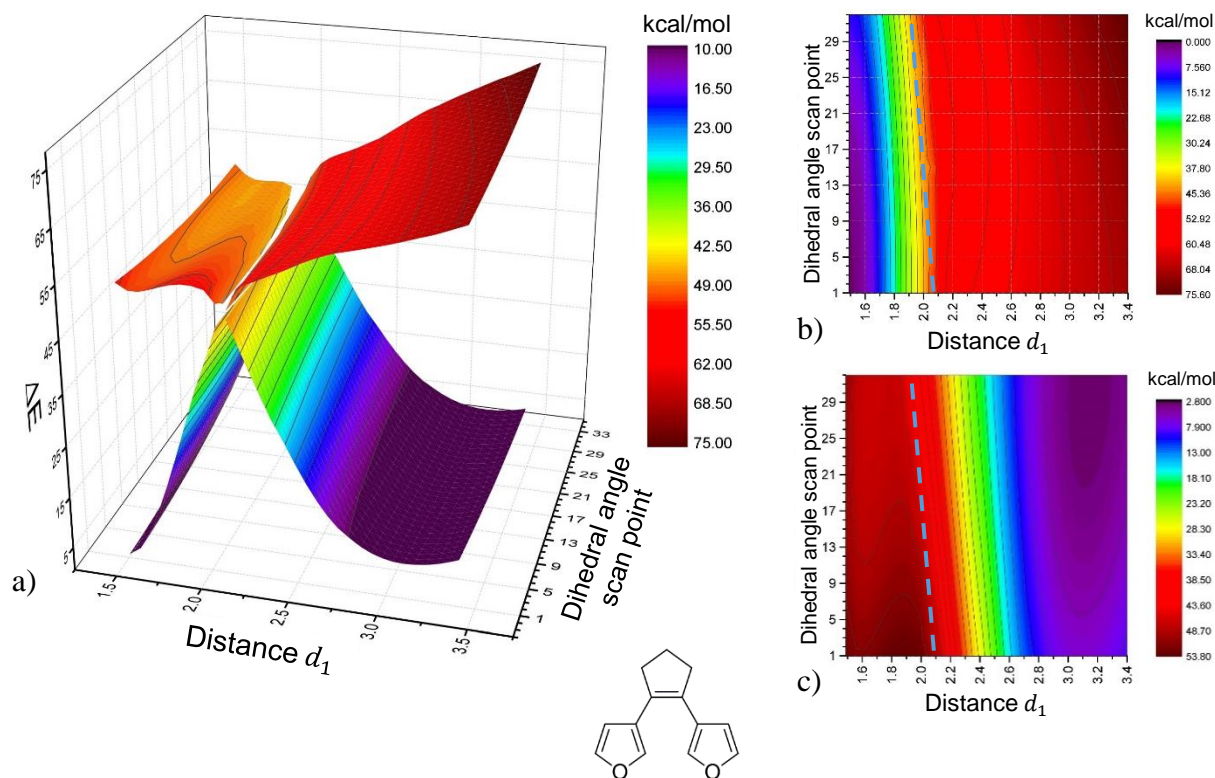


Figure 6-12: Diarylethene DA-2 a) Both potential energy surfaces combined in a 3-D representation. b) PES corresponding to the ring-closure reaction and the c) ring-opening reaction. Blue dashed line indicates the conical intersection.

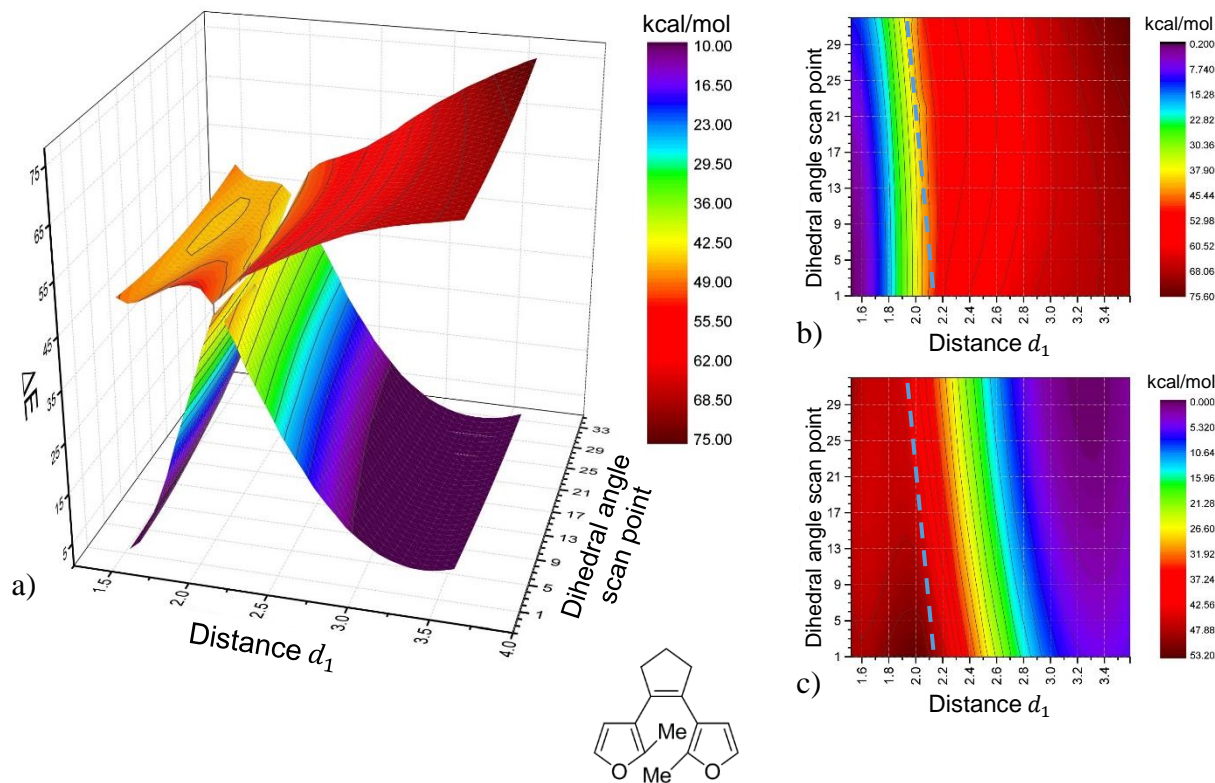


Figure 6-13: Diarylethene DA-3 a) Both potential energy surfaces combined in a 3-D representation. b) PES corresponding to the ring-closure reaction and the c) ring-opening reaction. Blue dashed line indicates the conical intersection.

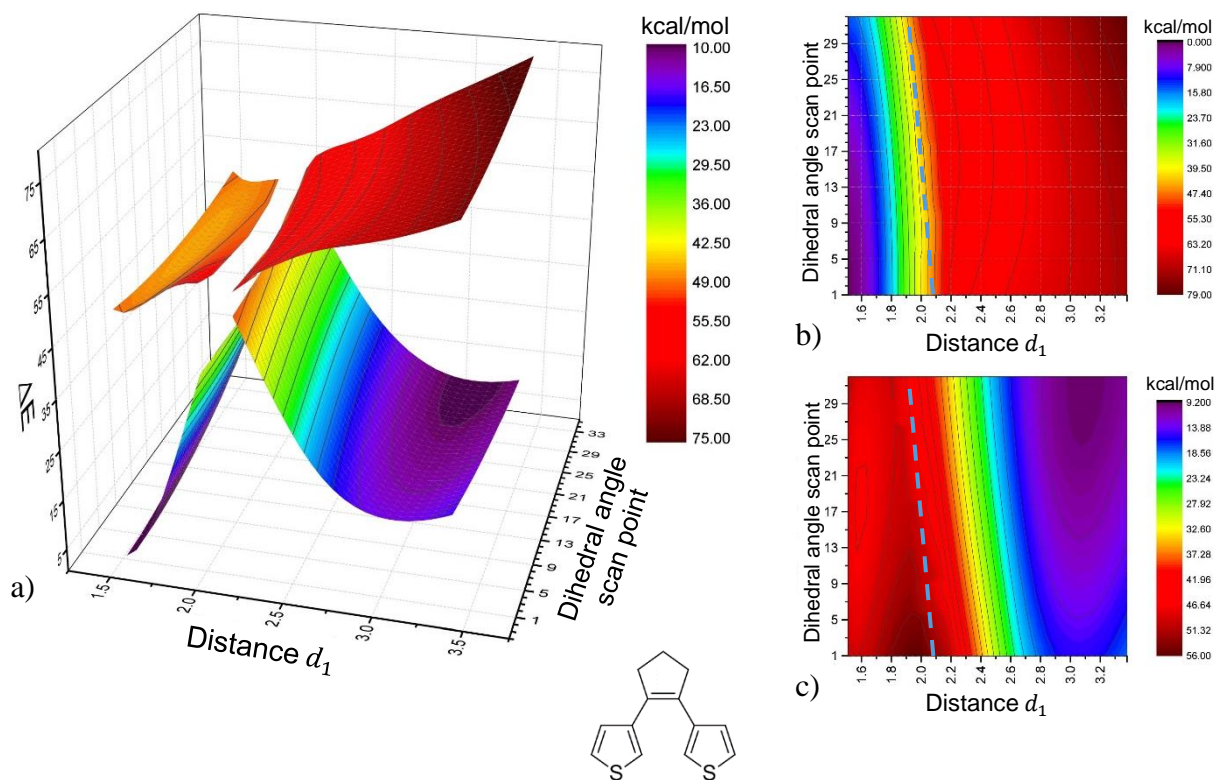


Figure 6-14: Diarylethene **DA-4** a) Both potential energy surfaces combined in a 3-D representation. b) PES corresponding to the ring-closure reaction and the c) ring-opening reaction. Blue dashed line indicates the conical intersection.

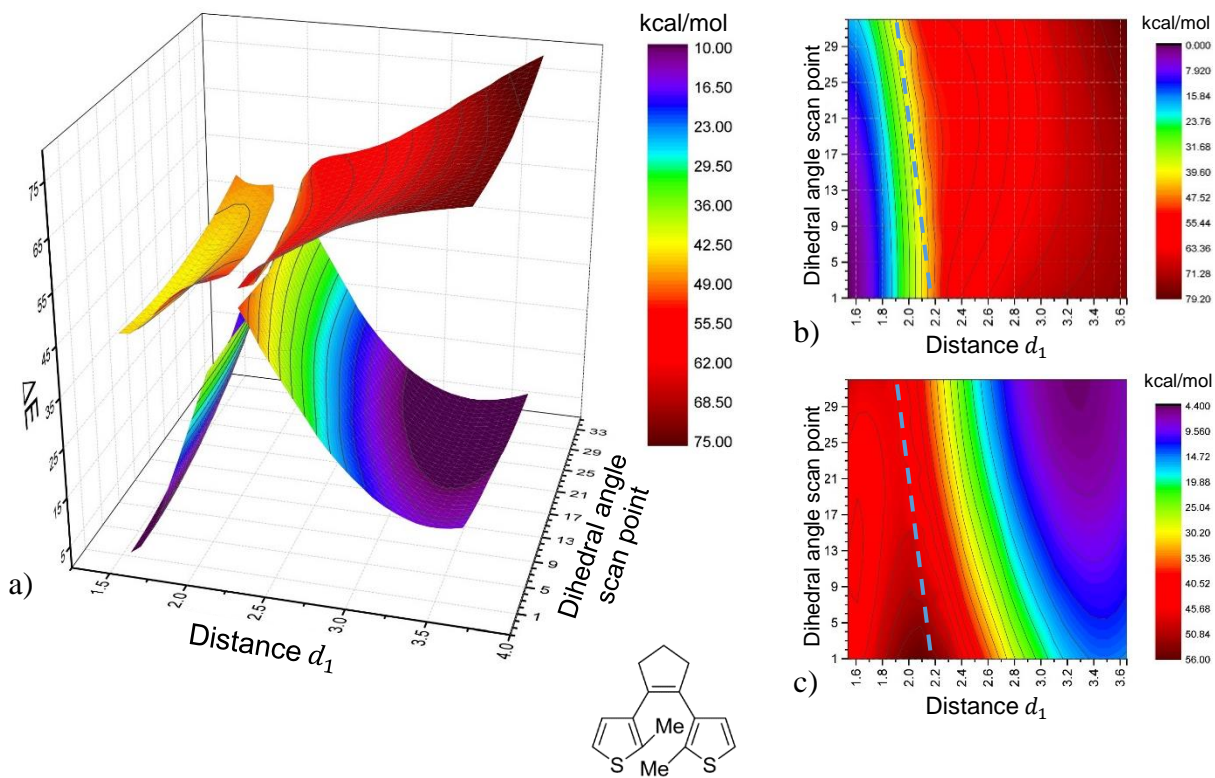


Figure 6-15: Diarylethene **DA-5** a) Both potential energy surfaces combined in a 3-D representation. b) PES corresponding to the ring-closure reaction and the c) ring-opening reaction. Blue dashed line indicates the conical intersection.

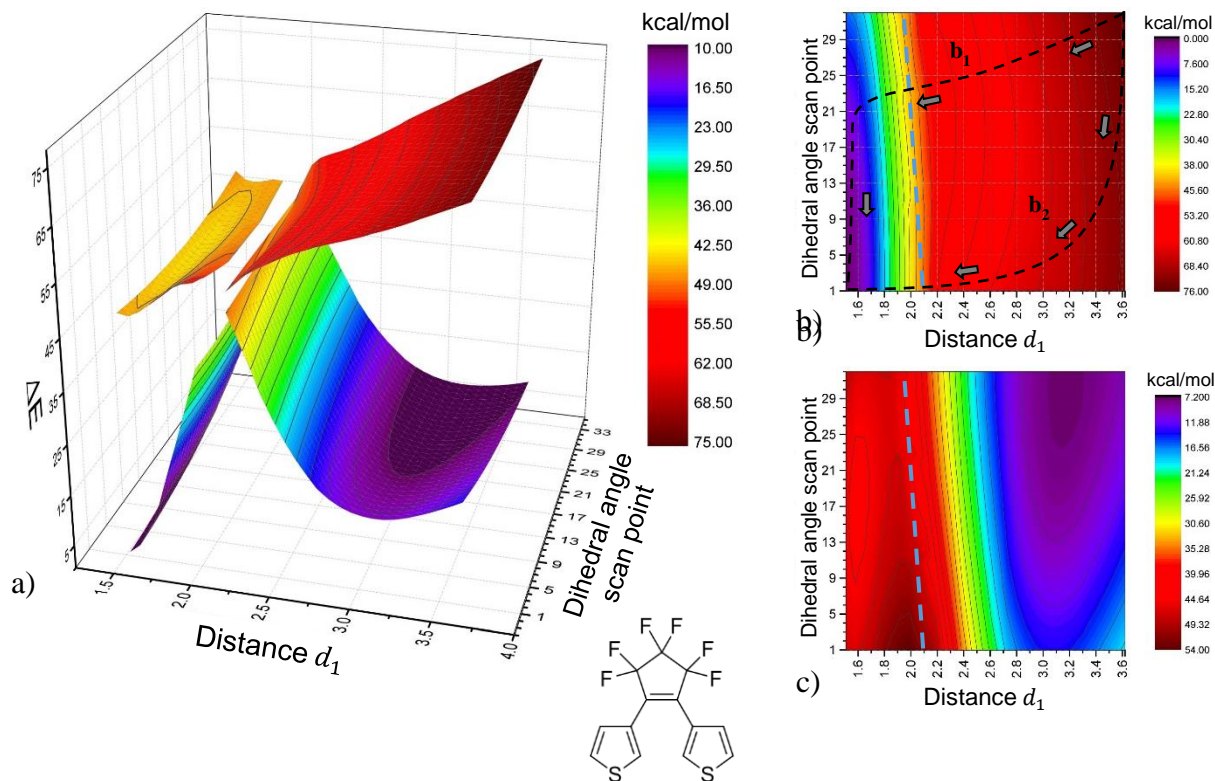


Figure 6-16: Diarylethene DA-6 a) Both potential energy surfaces combined in a 3-D representation. b) PES corresponding to the ring-closure reaction and the c) ring-opening reaction. Blue dashed line indicates the conical intersection.

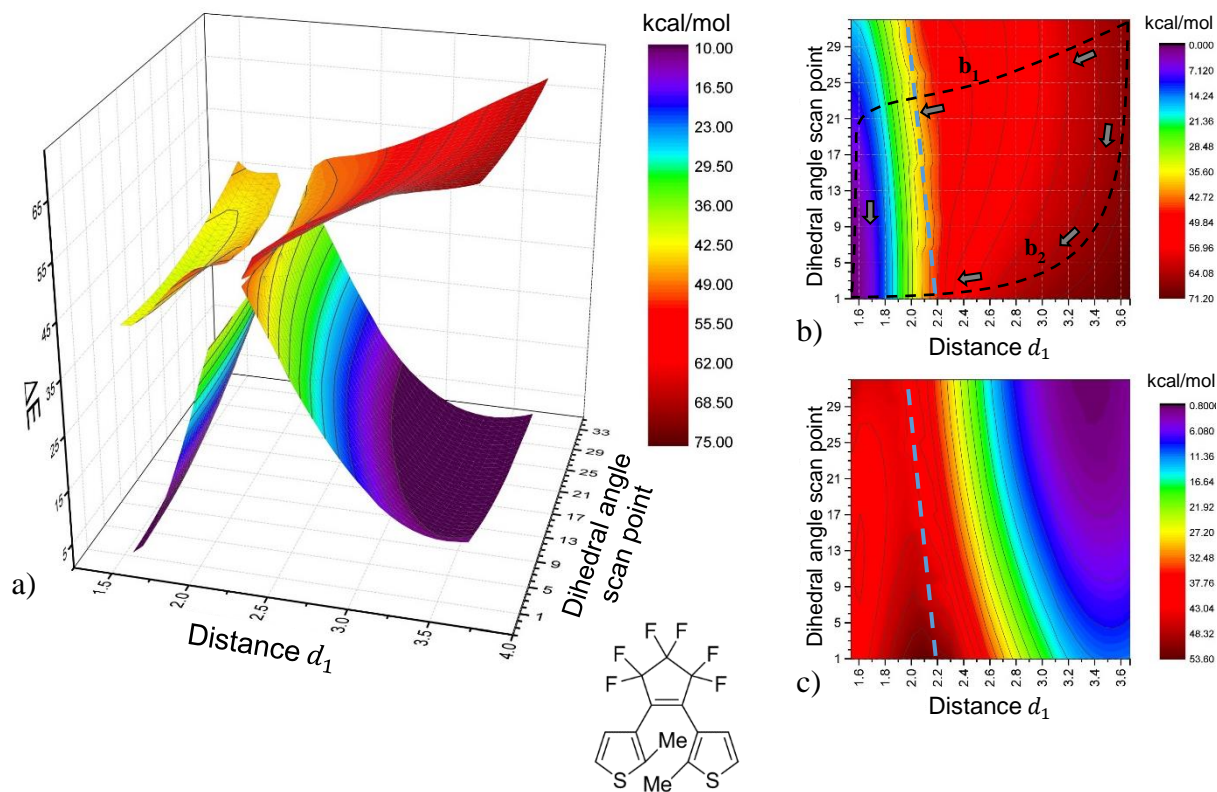


Figure 6-17: Diarylethene DA-7 a) Both potential energy surfaces combined in a 3-D representation. b) PES corresponding to the ring-closure reaction and the c) ring-opening reaction. Blue dashed line indicates the conical intersection.

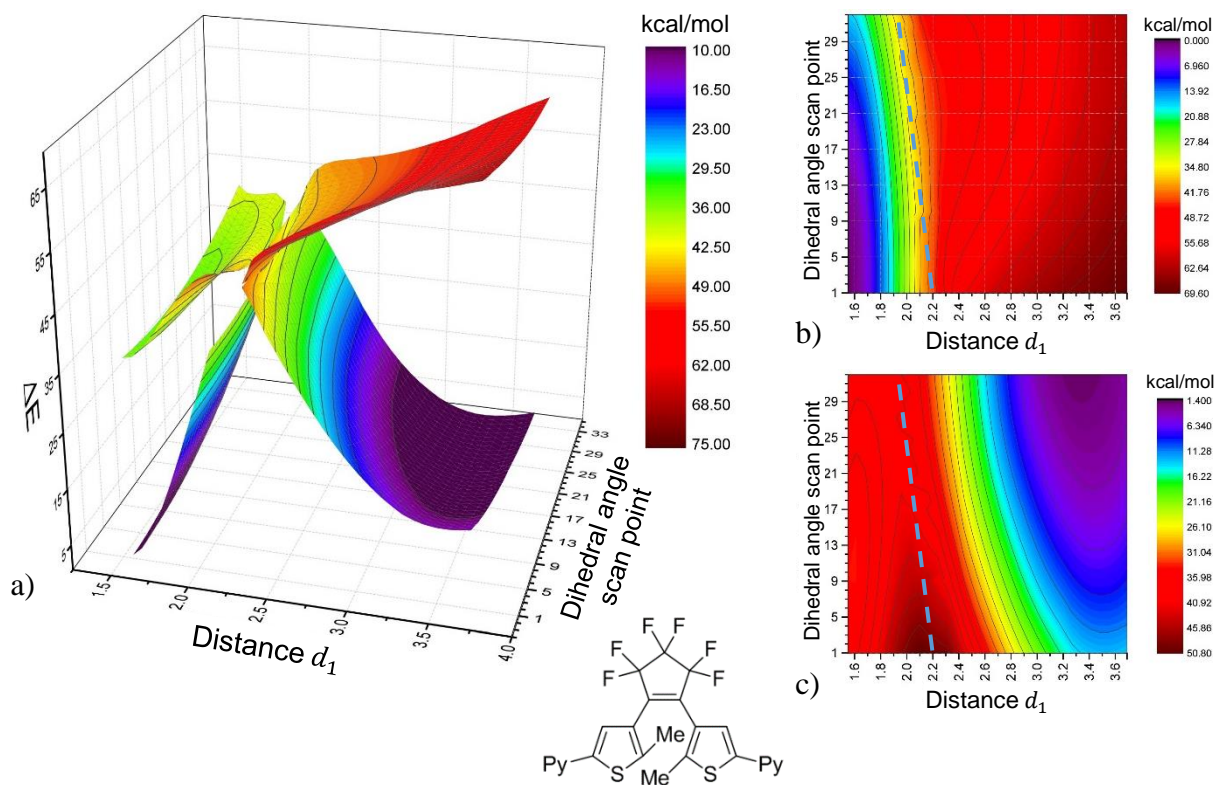


Figure 6-18: Diarylethene **DA-8** a) Both potential energy surfaces combined in a 3-D representation. b) PES corresponding to the ring-closure reaction and the c) ring-opening reaction. Blue dashed line indicates the conical intersection.

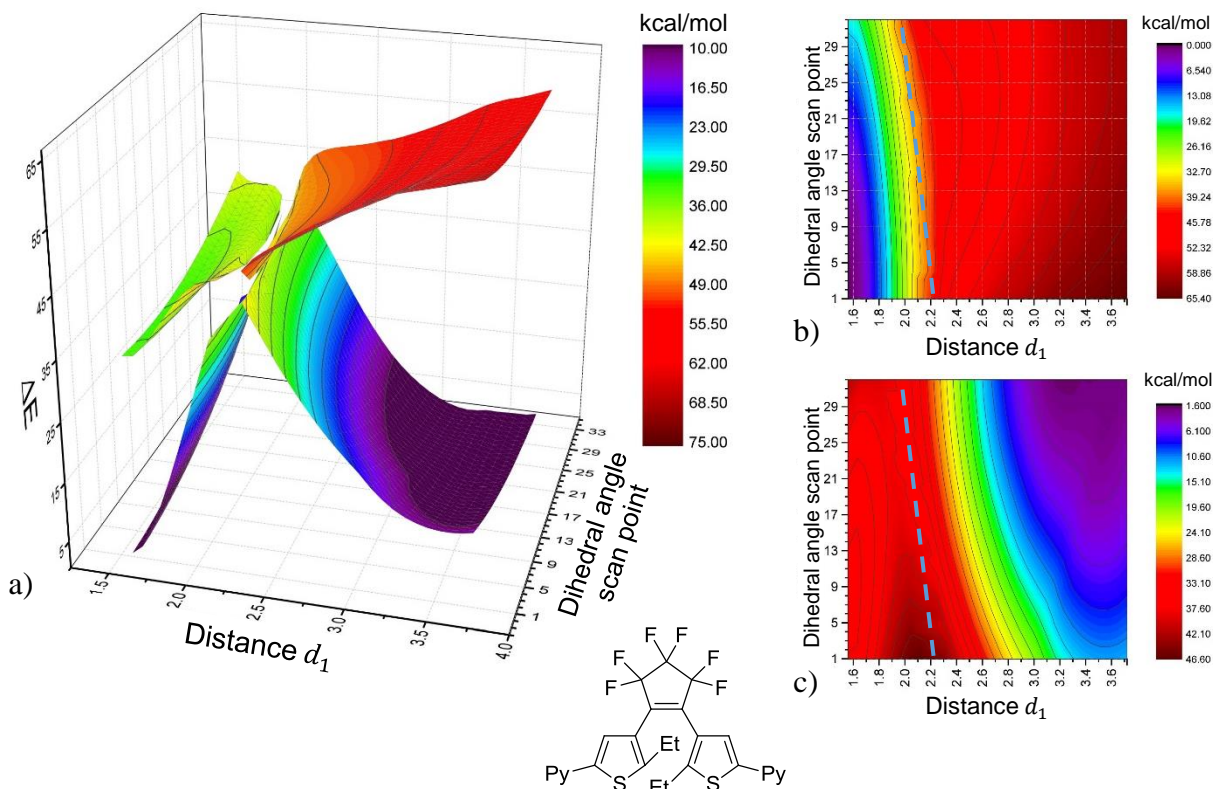


Figure 6-19: Diarylethene **DA-9** a) Both potential energy surfaces combined in a 3-D representation. b) PES corresponding to the ring-closure reaction and the c) ring-opening reaction. Blue dashed line indicates the conical intersection.

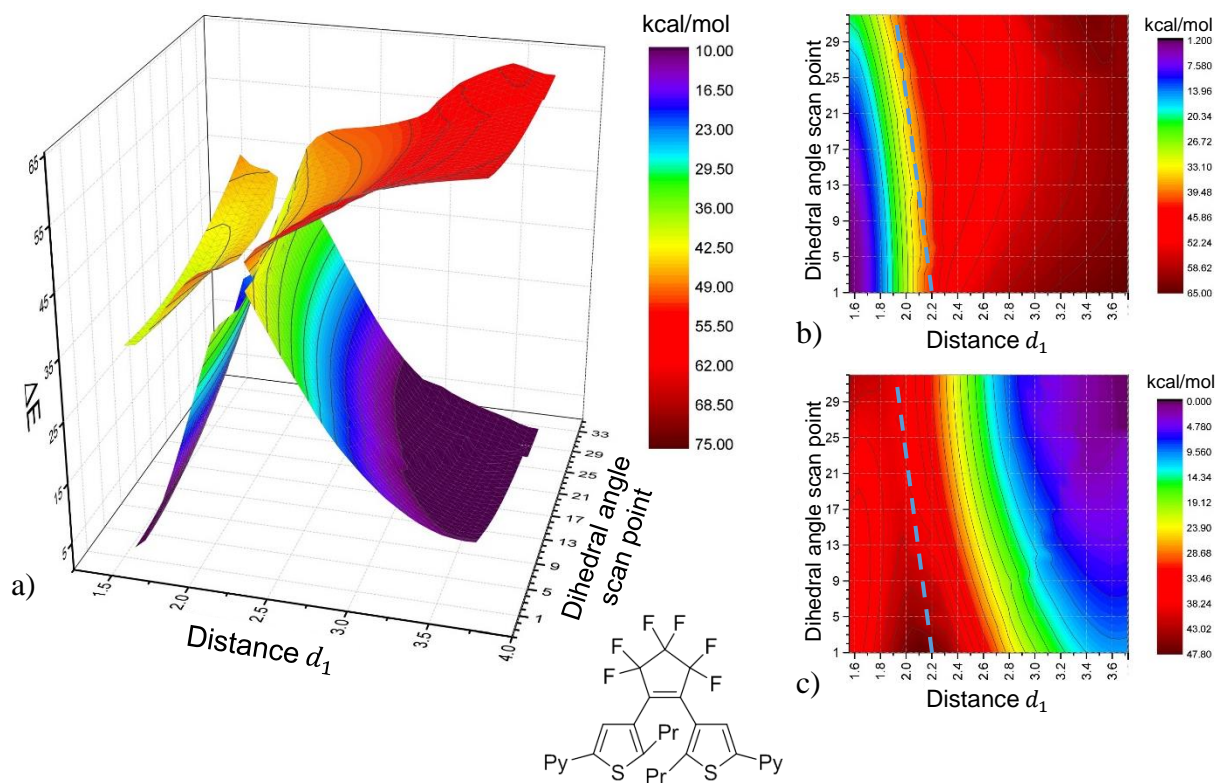


Figure 6-20: Diarylethene **DA-1** a) Both potential energy surfaces combined in a 3-D representation. b) PES corresponding to the ring-closure reaction and the c) ring-opening reaction. Blue dashed line indicates the conical intersection. Calculations carried out on this compound was done using the 6-311G basis set.

## 6.5 Discussion

A method was developed for explaining the photochromic behaviour of diarylethenes, such as that presented in Chapter 5, on a fundamental level. This method involved identifying and scanning all the major differences, in bond distances and angles, between the ring-closed and ring-opened forms. Three parameters were identified but reduced to two in order to make the whole process feasible. This was done by assuming that the dihedral angles,  $\theta_1$  and  $\theta_2$ , twist in a synchronous manner, which was proven by scanning them simultaneously whilst keeping the distance  $d_1$  constant. In the next step the distance  $d_1$ , which is the distance between the two adjoining carbon atoms, was scanned. Thereafter the excited state PES was calculated and presented along with the ground state PES.

The ring-closure can be ascribed to the formation of an electron hole after excitation of an electron. This results in a downward energy gradient and an attractive force between carbon atoms 2 and 5 of the two respective aryl rings. The reaction proceeds in the excited state until it reaches the conical intersection at which point a crossing of states takes place, the system returns to the ground state and the reaction proceeds to completion. For the ring-opening it was shown that there is a thermal barrier in the excited state that needs to be overcome in order for the reaction to proceed. This can be done by first twisting the dihedral angles in order to avoid the energy barrier. Thus the reaction is forced to take place in an asynchronous manner.

The importance of optimising a system in the excited state in order to study excited state properties was also illustrated. If this is not done there can be a large gap between the excited state and ground state PESs where the conical intersection needs to be. The logical conclusion of such an illustration is that the reaction requires some form of luminescence in order for the system to evolve back to the ground state. This is not the case since this was not observed experimentally. Thus in order to do a mechanistic study of a reaction that takes place in the excited state, it is essential to optimise the system in the excited state or in a near approximation to the excited state.

In the last section it was illustrated how various structural modifications affect the photoisomerisation reaction. This was done by applying the above-mentioned method to a range of model compounds. The results were illustrated in Figures 6-13 to 6-21. These graphical illustrations provide a clear and visual picture of how the photoisomerisation reaction will differ between different compounds. Some conclusions were drawn as to how different modifications will affect the response to external stimulus and the thermal stability of both forms.

## 6.6 Summary

A method for explaining the photochromic behaviour of diarylethenes was developed and used to explain on a fundamental level how diarylethenes respond to light. It was shown that a triplet transition state (Figure 6-3) exists and is the preferred route for a thermal conversion between the ring-opened and ring-closed forms. Both the ring-opening and ring-closure reactions were shown to be asynchronous processes although the ring-opening is much more so due to a thermal barrier in the excited state guiding the direction in which the reaction proceeds.

The importance of optimising a system in the excited state for studying excited state properties were illustrated. This was done by calculating and comparing the excited state PESs for geometries optimised in the triplet state and singlet ground state, with the triplet state resembling the excited state. For the singlet state geometries there is no conical intersection, while for the triplet state geometries there is a conical intersection that allows a photoisomerisation reaction to proceed via a radiationless process.

Lastly the same method was applied to a series of model compounds in order to illustrate the effect that various structural modifications will have on the photoisomerisation reaction. Placing a methyl or other group on the adjoining carbon atoms increases the asynchronicity of the ring-closure reaction and makes the closed form less responsive to light. Replacing the furyl rings with thiophene rings result in the ring-closed form being less reactive to light due to a larger thermal barrier in the excited state. An increasing the length of the hydrocarbon chain on the adjoining carbon atoms makes the ring-closed form thermodynamically less preferred and thus more unstable.

## Chapter 7: Conclusion and Future work

This chapter will conclude this dissertation. The three results chapters will be discussed consecutively in both the Conclusion and Future work sections.

### 7.1 Conclusion

Under specific conditions trianglimine **1** crystallises in the space group  $R3$ , with 11 Å wide one-dimensional channels. These crystals undergo a yellow-to-red colour conversion above a humidity of 55%. In Chapter 4 the cause of this yellow-to-red colour change was rationalised via a computational investigation. It was first shown that the chromophore of the system can be isolated and studied separately as a model compound in order to obtain information about the colour properties of the larger periodic system. By a process of elimination it was established that the colour change is due to an enolimine-ketoenamine transformation. Using Time-Dependent Density Functional Theory it was shown that this transformation results in a small peak appearing at 530 nm in the UV-Vis spectrum while the peak at 404 nm decreases slightly, thus also agreeing with the experimental spectra. This type of enolimine-ketoenamine transformation often occurs within a Schiff base as an iono-, solvato-, thermo- or photochromic process. In the trianglimine this transformation occurs due to the combination of a sorptiochromic and a hydrochromic process, which are both considered subcategories of solvatochromism.

In order to explain how water can result in this transformation an increasing number of water molecules were placed so that they formed hydrogen bonds with the oxygen of either the alcohol group or the keto group on the model compound, both with and without a surrounding solvent model. Before the addition of water molecules the enolimine state is 5.68 kcal/mol lower in energy than the ketoenamine state, making it the thermodynamically preferred state. As more H<sub>2</sub>O molecules are added the difference in energy becomes smaller until the preference is reversed. In the presence of three H<sub>2</sub>O molecules and a solvent model the enolimine state is 4.44 kcal/mol higher in energy, resulting in the ketoenamine state being thermodynamically preferred.

In Chapter 5 it was shown that a diarylethene molecule, **DA-2-[o]**, crystallises in the **DA-2-[o]- $\alpha$**  phase from the polar solvent acetone and in the **DA-2-[o]- $\beta$**  phase from non-polar solvent hexane. The compound exhibits photochromic behaviour in both crystalline phases, turning colourless to blue upon irradiation with UV light and back to colourless upon irradiation with visible light. These two phases are both in the space group  $P\bar{1}$  and are

polymorphs of each other. Using Differential Scanning Calorimetry (DSC) it was found that both phases undergo a phase transition upon heating to yield a third phase, **DA-2-[o]- $\gamma$** . This phase also displays photochromic behaviour even at 70 °C, becoming very dark blue under UV light and turning colourless again under visible light. Variable temperature powder X-ray diffraction (VT-PXRD) was used to confirm that this is indeed a third phase.

The DSC thermogram for **DA-2-[o]- $\beta$**  shows an endothermic peak at 63 °C for the first cycle and an endothermic peak at 59 °C for the second and third cycles. The DSC thermogram for the **DA-2-[o]- $\alpha$**  phase shows a broad endothermic peak between 70 °C and a 100 °C with a maximum at 93 °C for the first cycle. For the second cycle the endothermic peak shifts to 53 °C, a similar position to the **DA-2-[o]- $\beta$**  phase, suggesting that the **DA-2-[o]- $\alpha$**  phase has been converted to the **DA-2-[o]- $\beta$**  phase after the first heating-cooling cycle. This phase change was also confirmed with VT-PXRD. The crystal structure of the **DA-2-[o]- $\gamma$**  phase was determined by SCXRD by heating a crystal of the **DA-2-[o]- $\beta$**  phase to 70 °C with the cryostat. Mercury was used to predict the powder patterns of the three phases from the SCXRD-derived crystal structures in order to relate the three crystal structures to the DSC and VT-PXRD results.

It was also shown that **DA-2-[o]- $\beta$**  can be converted back to **DA-2-[o]- $\alpha$** ; leaving **DA-2-[o]- $\beta$**  in a cupboard at room temperature for six months causes it to completely convert into the **DA-2-[o]- $\alpha$**  phase. This suggests that **DA-2-[o]- $\alpha$**  is the thermodynamically preferred phase, which was confirmed by calculating the lattice energies for the **DA-2-[o]- $\alpha$**  and **DA-2-[o]- $\beta$**  phases. Per asymmetric unit the **DA-2-[o]- $\alpha$**  phase was 36.71 kcal/mol lower in energy than the **DA-2-[o]- $\beta$**  phase, which equates to an average of 18.4 kcal/mol per diarylethene molecule.

In Chapter 6 the photochromic behaviour of the diarylethene crystals was explained on a fundamental level by studying a model compound via computational means. A method was developed for studying diarylethene molecules, which involves scanning all the major differences in bond distances and angles between the ring-closed and ring-opened forms. This is followed by the calculation of the excited state potential energy surface for the space that was scanned. Furthermore, each scan point was optimised in the triplet state, rather than in the singlet state, since this results in geometries “closer” to the true geometry that the molecule adopts in the excited state.

The ring-closure reaction can be ascribed to the formation of an electron hole after the excitation of an electron from the HOMO to the LUMO. This results in a downward energy gradient towards the ring-closed structure and an attractive force between the adjoining carbon atoms, driving forward the ring-closure reaction. A similar scenario occurs for the reverse

reaction: After the excitation of an electron there is once again a downward gradient towards the ring-opened structure. This time, however, there is a thermal barrier in the excited state that has to be overcome in order to reach the downward gradient. This forces the dihedral angles to twist first, which results in the breaking of the conjugated  $\pi$ -system, before the ring opening can take place. This process can be described as being asynchronous, as can be clearly illustrated, as shown in Figure 6-8.

For the last part of Chapter 6 the same method for studying diarylethenes was applied to a range of molecules in order to study the influence that various structural modifications have on the ring-closing or ring-opening ability of a compound. Placing methyl groups on the two adjoining carbon atoms causes the ring-closure to take place in a much more asynchronous manner. This also results in an increase in the energy difference between the ring-closed and ring-opened forms while increasing the initial barrier to ring-closure. This suggests that the ring-closed form is thermodynamically less preferred and also less responsive to light. Replacing the furyl rings with thiophene rings results in the ring-closed form being less responsive to light due to a larger thermal barrier in the excited state. Increasing the length of the hydrocarbon chain on the adjoining carbon atoms makes the ring-closed form thermodynamically less preferred and thus more unstable.

In this project various types of chromic phenomena were introduced and explained and the polymorphism of a chromic diarylethene compound was elucidated. Chromic phenomena remains a hot topic and a keen field of interest owing to not only the fact that it is a beautiful display of how the laws of nature are at play at a fundamental level but also due to the many practical applications that arise as our understanding of chromic systems improves. This study adds to our fundamental understanding of how chromic systems in the solid or crystalline state work and opens the door to even more cutting edge research into this phenomenal field of chemistry.

## 7.2 Future Work

To end this dissertation I wish to summarise some ideas that were just outside the scope or the aims of this project, yet relevant and thus deserve being mentioned as work that could be done in the future.

In Chapter 4 it was shown that the ketoenamine form is responsible for the red colour. When studying the model compound (Section 4.4) it was observed that the amine adopts a planar state. The question remains as to what the hybridisation state of the nitrogen atom is and what the driving force behind the adoption of the planar form is. In Section 4.5 a trifurcated

hydrogen-bonding system resulted in the ketoenamine being 4.44 kcal/mol lower in energy than the enolimine form, which is the largest difference we could achieve by randomly placing water molecules around the enol/keto oxygen atom. This result is, however, dependent on the initial geometry that was selected for the H<sub>2</sub>O molecules and the question still needs to be answered as to how far this reaction can be driven forward by water. In other words, what geometry needs to be adopted in order to reach a maximum difference between the ketoenamine and enolimine forms, thus driving this reaction forward, and how large a difference can be achieved?

In Chapter 5 a crystal structure of **DA-1-[c]** (the closed form of **DA-1**) could not be obtained despite numerous attempts. Determining this structure or finding an adequate explanation for why it cannot be obtained would thus be a reasonable goal. It was also shown that **DA-1-[o]-β** converts to **DA-1-[c]-α** over a period of six months. This time could, however, be much shorter and a time evolution experiment needs to be done to see exactly how this transition occurs. It might also be possible to calculate the structure of the transition state for this phase conversion. This would provide us with the energy required for such a transition to take place and/or explain why this phase transition occurs spontaneously at ambient conditions.

For Chapter 6 the two main aims can be summarised as follows: firstly explain the diarylethene photoisomerisation reaction on a fundamental level and secondly make predictions regarding the properties of diarylethenes based on theoretical calculations. Considering the former aim, using CASSCF for calculating potential energy surfaces could be a better approach to modelling the photochemical diarylethene reaction. CASSCF allows for the specification of an active space of filled and empty molecular orbitals. Multiple electron configurations can be specified in a much more controlled fashion, as compared to using TD-DFT, and could aid in finding the true excited state geometries. CASSCF is also a good approach to finding conical intersections,<sup>109</sup> while this is a difficult task when using DFT and TD-DFT. Considering the latter aim, it would be helpful if one could accurately predict the behaviour of a diarylethene molecule using computational means. This could possibly be achieved by making a comparison between available experimental data and computational data. Also it must be considered carefully as to what theoretical parameters are related to which physical properties. In other words if one were to, for example, attempt to predict the fatigue resistance of a compound, the question lies as to what theoretical parameters are related to that property. This is an interesting aspect that deserves further investigation in the future.

## References

- 1 R. L. Allen, *Colour Chemistry*, Springer US, New York, 2013.
- 2 P. Bamfield, *Chromic Phenomena: Technological Applications of Colour Chemistry*, Royal Society of Chemistry, 2010.
- 3 R. Christie, *Colour Chemistry*, Royal Society of Chemistry, 2015.
- 4 A. S. Travis, *Technol. Cult.*, 1990, **31**, 51–82.
- 5 P. F. Gordon and P. Gregory, *Organic Chemistry in Colour*, Springer Berlin Heidelberg, 2012.
- 6 E. Steingruber, *Ullmann's Encycl. Ind. Chem.*, 2004.
- 7 R. M. Hoffman, *Nat. Rev. Cancer*, 2005, **5**, 796.
- 8 C. Larson, B. Peele, S. Li, S. Robinson, M. Totaro, L. Beccai, B. Mazzolai and R. Shepherd, *Science.*, 2016, **351**, 1071–1074.
- 9 R. Eelkema and B. L. Feringa, *Org. Biomol. Chem.*, 2006, **4**, 3729–3745.
- 10 B. L. Feringa and W. R. Browne, *Molecular switches*, Wiley Online Library, 2001, vol. 42.
- 11 B. L. Feringa, *J. Org. Chem*, 2007, **72**, 6635–6652.
- 12 B. L. Feringa, *Angew. Chemie Int. Ed.*, 2017.
- 13 H. Li and D.-H. Qu, *Sci. China Chem.*, 2015, **58**, 916–921.
- 14 D. Bléger and S. Hecht, *Angew. Chemie Int. Ed.*, 2015, **54**, 11338–11349.
- 15 S. Kobatake, K. Uchida, E. Tsuchida and M. Irie, *Chem. Commun.*, 2002, 2804–2805.
- 16 Y. Liu, A. H. Flood, P. A. Bonvallet, S. A. Vignon, B. H. Northrop, H.-R. Tseng, J. O. Jeppesen, T. J. Huang, B. Brough and M. Baller, *J. Am. Chem. Soc.*, 2005, **127**, 9745–9759.
- 17 B. Gui, Y. Meng, Y. Xie, K. Du, A. C. Sue and C. Wang, *Macromol. Rapid Commun.*, 2017.
- 18 N. Fuentes, A. Martín-Lasanta, L. Á. de Cienfuegos, M. Ribagorda, A. Parra and J. M. Cuerva, *Nanoscale*, 2011, **3**, 4003–4014.
- 19 P. A. Gale and J. W. Steed, *Supramolecular chemistry: from molecules to nanomaterials*, Wiley Online Library, 2012.
- 20 L. J. Barbour, D. Das, T. Jacobs, G. O. Lloyd and V. J. Smith, *Supramol. Chem. From Mol. to Nanomater.*, 2012.
- 21 D. Young, *Computational chemistry: a practical guide for applying techniques to real world problems*, John Wiley & Sons, 2004.

- 22 F. Jensen, *West Sussex, Engl. John Wiley Sons Ltd*, 30–34.
- 23 M. J. Frisch, G. W. Trucks, H. B. Schlegel, G. E. Scuseria, M. A. Robb, J. R. Cheeseman, G. Scalmani, V. Barone, G. A. Petersson, H. Nakatsuji, X. Li, M. Caricato, A. V. Marenich, J. Bloino, B. G. Janesko, R. Gomperts, B. Mennucci, H. P. Hratchian, J. V. Ortiz, A. F. Izmaylov, J. L. Sonnenberg, Williams, F. Ding, F. Lipparini, F. Egidi, J. Goings, B. Peng, A. Petrone, T. Henderson, D. Ranasinghe, V. G. Zakrzewski, J. Gao, N. Rega, G. Zheng, W. Liang, M. Hada, M. Ehara, K. Toyota, R. Fukuda, J. Hasegawa, M. Ishida, T. Nakajima, Y. Honda, O. Kitao, H. Nakai, T. Vreven, K. Throssell, J. A. Montgomery Jr., J. E. Peralta, F. Ogliaro, M. J. Bearpark, J. J. Heyd, E. N. Brothers, K. N. Kudin, V. N. Staroverov, T. A. Keith, R. Kobayashi, J. Normand, K. Raghavachari, A. P. Rendell, J. C. Burant, S. S. Iyengar, J. Tomasi, M. Cossi, J. M. Millam, M. Klene, C. Adamo, R. Cammi, J. W. Ochterski, R. L. Martin, K. Morokuma, O. Farkas, J. B. Foresman and D. J. Fox, *Gaussian 09, Inc. Wallingford CT*, 2016.
- 24 Y. Ishibashi, M. Fujiwara, T. Umesato, H. Saito, S. Kobatake, M. Irie and H. Miyasaka, *J. Phys. Chem. C*, 2011, **115**, 4265–4272.
- 25 K. Matsuda and M. Irie, *J. Photochem. Photobiol. C Photochem. Rev.*, 2004, **5**, 169–182.
- 26 M. Kwit, A. Plutecka, U. Rychlewska, J. Gawroński, A. F. Khlebnikov, S. I. Kozhushkov, K. Rauch and A. de Meijere, *Chem. Eur. J.*, 2007, **13**, 8688–8695.
- 27 A. Janiak, M. Bardziński, J. Gawroński and U. Rychlewska, *Cryst. Growth Des.*, 2016, **16**, 2779–2788.
- 28 J. Gawronski, K. Gawronska, J. Grajewski, M. Kwit, A. Plutecka and U. Rychlewska, *Chem. Eur. J.*, 2006, **12**, 1807–1817.
- 29 G. Book, *Int. Union Pure Appl. Chem.*, 2014, 528.
- 30 P. A. Vigato, S. Tamburini and L. Bertolo, *Coord. Chem. Rev.*, 2007, **251**, 1311–1492.
- 31 A. D. Garnovskii and I. S. Vasil'chenko, *Russ. Chem. Rev.*, 2002, **71**, 943–968.
- 32 A. D. Garnovskii, A. L. Nivorozhkin and V. I. Minkin, *Coord. Chem. Rev.*, 1993, **126**, 1–69.
- 33 A. K. Padhy, A. K. Mishra, M. Mohapatra, A. K. Pati and S. Mishra, *RSC Adv.*, 2014, **4**, 8044–8049.
- 34 V. I. Minkin, A. V Tsukanov, A. D. Dubonosov and V. A. Bren, *J. Mol. Struct.*, 2011, **998**, 179–191.
- 35 A. Jiménez-Sánchez, M. Rodríguez, R. Métivier, G. Ramos-Ortíz, J. L. Maldonado, N. Réboles, N. Farfán, K. Nakatani and R. Santillan, *New J. Chem.*, 2014, **38**, 730–738.
- 36 E. Hadjoudis and I. M. Mavridis, *Chem. Soc. Rev.*, 2004, **33**, 579–588.

- 37 E. Hadjoudis, M. Vittorakis and I. Moustakali-Mavridis, *Tetrahedron*, 1987, **43**, 1345–1360.
- 38 A. Chattopadhyay, M. Meier, S. Ivaninskii, P. Burkhard, F. Speroni, B. Campanini, S. Bettati, A. Mozzarelli, W. M. Rabeh and L. Li, *Biochemistry*, 2007, **46**, 8315–8330.
- 39 M. Tümer, H. Köksal, S. Serin and M. Dig, *Transit. Met. Chem.*, 1999, **24**, 13–17.
- 40 Z. Liang, Z. Liu and Y. Gao, *Tetrahedron Lett.*, 2007, **48**, 3587–3590.
- 41 F. B. Mallory, C. S. Wood and J. T. Gordon, *J. Am. Chem. Soc.*, 1964, **86**, 3094–3102.
- 42 F. B. Mallory and C. W. Mallory, *Org. React.*, 1984.
- 43 R. M. Kellogg, M. B. Groen and H. Wynberg, *J. Org. Chem.*, 1967, **32**, 3093–3100.
- 44 S. Nakamura and M. Irie, *J. Org. Chem.*, 1988, **53**, 6136–6138.
- 45 M. Irie and M. Mohri, *J. Org. Chem.*, 1988, **53**, 803–808.
- 46 M. Irie, T. Fukaminato, K. Matsuda and S. Kobatake, *Chem. Rev.*, 2014, **114**, 12174–12277.
- 47 M. Morimoto and M. Irie, *Chem. Commun.*, 2005, 3895–3905.
- 48 S. Kobatake and M. Irie, *Bull. Chem. Soc. Jpn.*, 2004, **77**, 195–210.
- 49 M. Irie, K. Uchida, T. Eriguchi and H. Tsuzuki, *Chem. Lett.*, 1995, **24**, 899–900.
- 50 D. Kitagawa and S. Kobatake, *Chem. Asian J.*, 2014, **9**, 289–293.
- 51 C. A. Ullrich, *Time-Dependent Density-Functional Theory: Concepts and Applications*, OUP Oxford, 2011.
- 52 W. Koch and M. C. Holthausen, *A Chemist's Guide to Density Functional Theory*, Wiley, 2015.
- 53 R. P. Feynman, A. R. Hibbs and D. F. Styer, *Quantum Mechanics and Path Integrals*, Dover Publications, 2010.
- 54 I. N. Levine, *Quantum chemistry 5th ed*, Prentice-Hall Inc.: New Jersey, New York, 1991.
- 55 P. W. Atkins, *Physical Chemistry*, Oxford University Press, 1998.
- 56 H. Smith, *Introduction to Quantum Mechanics*, World Scientific, 1991.
- 57 C. J. Cramer, *Essentials of Computational Chemistry: Theories and Models*, Wiley, 2005.
- 58 G. A. Zhurko, Graph. Progr. Vis. quantum Chem. Comput. <https://chemcraftprog.com>.
- 59 L. J. Barbour, *J. Supramol. Chem.*, 2001, **189**.
- 60 D. Castell, unpublished results
- 61 APEX3, S., and SADABS; Bruker AXS Inc.: Madison, WI; 2016.
- 62 G. M. Sheldrick, *Acta Cryst. A64*, 2008, **112**.

- 63 C. R. Groom, I. J. Bruno, M. P. Lightfoot and S. C. Ward, *Acta Crystallogr. Sect. B Struct. Sci. Cryst. Eng. Mater.*, 2016, **72**, 171–179.
- 64 I. J. Bruno, J. C. Cole, P. R. Edgington, M. Kessler, C. F. Macrae, P. McCabe, J. Pearson and R. Taylor, *Acta Crystallogr. Sect. B Struct. Sci.*, 2002, **58**, 389–397.
- 65 C. F. Macrae, P. R. Edgington, P. McCabe, E. Pidcock, G. P. Shields, R. Taylor, M. Towler and J. van de Streek, *J. Appl. Crystallogr.*, 2006, **39**, 453–457.
- 66 J. A. Pople, *J. Comput. Chem.*, 2004, **25**, v–viii.
- 67 W. J. Hehre, R. F. Stewart and J. A. Pople, *J. Chem. Phys.*, 1969, **51**, 2657–2664.
- 68 M. D. Newton, *J. Chem. Phys.*, 1969, **51**, 3917–3926.
- 69 M. D. Newton, W. A. Lathan, W. J. Hehre and J. A. Pople, *J. Chem. Phys.*, 1970, **52**, 4064.
- 70 R. Ditchfield, W. J. Hehre and J. A. Pople, *J. Chem. Phys.*, 1970, **52**, 5001–5007.
- 71 Dassault Systèmes BIOVIA, Mater. Stud. 2016, 16.1.0.21, San Diego Dassault Systèmes, 2016.
- 72 B. Delley, *J. Chem. Phys.*, 2000, **113**, 7756–7764.
- 73 B. Delley, *J. Chem. Phys.*, 1990, **92**, 508–517.
- 74 R. Dennington, T. Keith and J. Millam, Gaussview, Version 5, Semichem Inc. Shawnee Mission. KS, 2009.
- 75 M. D. Hanwell, D. E. Curtis, D. C. Lonie, T. Vandermeersch, E. Zurek and G. R. Hutchison, *J. Cheminform.*, 2012, **4**, 17.
- 76 S. Grimme, S. Ehrlich and L. Goerigk, *J. Comput. Chem.*, 2011, **32**, 1456–1465.
- 77 S. Grimme, *J. Comput. Chem.*, 2006, **27**, 1787–1799.
- 78 H. L. Schmider and A. D. Becke, *J. Chem. Phys.*, 1998, **108**, 9624–9631.
- 79 J. P. Perdew, K. Burke and M. Ernzerhof, *Phys. Rev. Lett.*, 1996, **77**, 3865.
- 80 K. Burke, J. P. Perdew and M. Ernzerhof, *Phys. Rev. Lett.*, 1997, **78**, 1396.
- 81 A. D. Becke, *J. Chem. Phys.*, 1993, **98**, 5648–5652.
- 82 Y. Zhao and D. G. Truhlar, *Theor. Chem. Accounts Theory, Comput. Model. (Theoretica Chim. Acta)*, 2008, **120**, 215–241.
- 83 T. Yanai, D. P. Tew and N. C. Handy, *Chem. Phys. Lett.*, 2004, **393**, 51–57.
- 84 J.-D. Chai and M. Head-Gordon, *Phys. Chem. Chem. Phys.*, 2008, **10**, 6615–6620.
- 85 S. Grimme, J. Antony, S. Ehrlich and H. Krieg, *J. Chem. Phys.*, 2010, **132**, 154104.
- 86 S. Grimme, *J. Comput. Chem.*, 2004, **25**, 1463–1473.
- 87 R. Krishnan, J. S. Binkley, R. Seeger and J. A. Pople, *J. Chem. Phys.*, 1980, **72**, 650–654.

- 88 A. D. McLean and G. S. Chandler, *J. Chem. Phys.*, 1980, **72**, 5639–5648.
- 89 M. J. Frisch, J. A. Pople and J. S. Binkley, *J. Chem. Phys.*, 1984, **80**, 3265–3269.
- 90 T. Clark, J. Chandrasekhar, G. W. Spitznagel and P. V. R. Schleyer, *J. Comput. Chem.*, 1983, **4**, 294–301.
- 91 H. B. Schlegel, *Wiley Interdiscip. Rev. Comput. Mol. Sci.*, 2011, **1**, 790–809.
- 92 M. W. Wong, K. B. Wiberg and M. J. Frisch, *J. Am. Chem. Soc.*, 1992, **114**, 1645–1652.
- 93 L. J. Barbour, *Chem. Commun.*, 2006, 1163–1168.
- 94 A. Janiak, M. du Plessis, D. C. Myburgh, C. Esterhuysen, L. J. Barbour, *Nat. Chem.* in preparation
- 95 W. C. McCrone, *Phys. Chem. Org. solid state*, 1965, **2**, 725–767.
- 96 J. Bernstein, *Polymorphism in molecular crystals*, Oxford University Press, 2002, vol. 14.
- 97 T. Mori, *Chem. Rev.*, 2004, **104**, 4947–4970.
- 98 M. Sorai, M. Nakano and Y. Miyazaki, *Chem. Rev.*, 2006, **106**, 976–1031.
- 99 T. Mutai, H. Tomoda, T. Ohkawa, Y. Yabe and K. Araki, *Angew. Chemie Int. Ed.*, 2008, **47**, 9522–9524.
- 100 G. Zhang, J. Lu, M. Sabat and C. L. Fraser, *J. Am. Chem. Soc.*, 2010, **132**, 2160–2162.
- 101 S. Yamamoto, K. Matsuda and M. Irie, *Org. Lett.*, 2003, **5**, 1769–1772.
- 102 M. Morimoto, S. Kobatake and M. Irie, *Chem. Eur. J.*, 2003, **9**, 621–627.
- 103 M. Irie, T. Fukaminato, K. Matsuda and S. Kobatake, *Chem. Rev.*, 2014, **114**, 12174–12277.
- 104 M. Irie, *Chem. Rev.*, 2000, **100**, 1685–1716.
- 105 M. Irie, S. Kobatake and M. Horichi, *Science.*, 2001, **291**, 1769–1772.
- 106 M. Irie and K. Matsuda, *Electron Transf. Chem.*, 2001, 215–242.
- 107 S. Kobatake, S. Takami, H. Muto, T. Ishikawa and M. Irie, *Nature*, 2007, **446**, 778.
- 108 C. Bechinger, S. Ferrere, A. Zaban, J. Sprague and B. A. Gregg, *Nature*, 1996, **383**, 608–610.
- 109 M. Boggio-Pasqua, M. Ravaglia, M. J. Bearpark, M. Garavelli and M. A. Robb, *J. Phys. Chem. A*, 2003, **107**, 11139–11152.
- 110 B. G. Levine and T. J. Martínez, *Annu. Rev. Phys. Chem.*, 2007, **58**, 613–634.

## Supplementary information

### Generating and submitting inputs to Gaussian

Although there are Linux and Windows versions of Gaussian available, for this project the Stellenbosch high performance computing cluster was utilized which runs on the Linux operating system. This requires jobs to be submitted to the Gaussian program via the Linux command line. In order to do this an input file is required. This contains all the details and specifications of the calculation to be run. The input file is submitted to a cluster or local computer via the command line either via a script, on a cluster, or by recalling the Gaussian program on a local computer.

Figure 8-1 is an example of a standard input file containing some of the basic components required in an input file. Lines 1 and 2 specify the number of processors and memory to be allocated to the job. Line 3 requests that a checkpoint file be written which can be used in a range of instances. Sometimes a job that stopped halfway can be continued from the checkpoint file. Or when a series of jobs have to be performed where each concurrent job depends on the results of the previous one, results can be stored in the checkpoint file and recalled for successive jobs. Another use of the checkpoint file is for the plotting of electrostatic potential maps. Within line 4 the method is specified, which in this case is the B3LYP hybrid functional, along with the basis set and any keywords specifying what kind of calculations should be performed. Line 6 contains any notes about the calculation to be performed and line 8 the charge and spin multiplicity. Thereafter the atoms and their respective x, y and z coordinates are specified followed by two empty spaces.

An input file is in fact just a normal text file ending on .inp and can be prepared manually in a text editor such as Notepad++ or generated in a range of visualisation and editing programs such as Avogadro or Gaussview. Avogadro is handy in this sense as it has a built in and easily accessible molecular dynamics based optimisation tool that makes the generating of good starting geometries easy. This then is the general outline of an input file.

```

01  %nprocs=8
02  %mem=16GB
03  %Chk=acetone.chk
04  #B3LYP/6-31G GFInput Opt Freq
05  ---EMPTY SPACE---
06  acetone Opt
07  ---EMPTY SPACE---
08  0 1
09  O      1.8770816641    -0.0389513320    0.0244963303
10  C     -0.1204851326    -0.0017710425    1.2785869278
11  C      0.6557840462    -0.0263319953   -0.0021604882
12  C     -0.0642112720    -0.0354289407   -1.3155663709
13  H     -0.7712045460    -0.8991479257    1.3378728556
14  H      0.5644293022     0.0021146742    2.1533606800
15  H     -0.7520057036     0.9104273581    1.3148038565
16  H     -0.7122529732    -0.9344073889   -1.3797189302
17  H     -0.6930544714     0.8751680761   -1.4027737298
18  H      0.6579891231    -0.0538442683   -2.1596276621
19  ---EMPTY SPACE---
20  ---EMPTY SPACE---

```

Figure 8-1: A basic Gaussian input file for the optimisation of an acetone molecule.

## Visualisation and processing of data

For this study a proper visualisation program was essential for analysing and presenting data. For this purpose Chemcraft<sup>58</sup> was mostly used but Gaussview<sup>74</sup> also came in handy for some of the features that it contains. Chemcraft was used to make most of the pictures as atom colours, background and the general format can easily be modified as desired. In addition Chemcraft makes the often tedious process of analysing the log files generated by Gaussian fairly easy with built-in functions for visualising free energies and frequencies, MO energies and topologies, electrostatic surface potentials, excited state energies and many other properties. Gaussview was used mostly for generating UV-Vis spectra but has about the same functionality and was used in conjunction with Chemcraft.

These programs are convenient for analysing single jobs, as was done in Chapter 4, however as in Chapter 6 generating  $32 \times 32$  plots requires the extraction of data from a very large set of log files as well as generating and submitting a large amount of input files and scripts simultaneously. To make this process feasible some form of automation was required and this was accomplished by shell scripting.

Figure 8-2 is an example of a simple shell script or program that can be run by the Unix shell in the Linux command line. In order to make a shell script one needs a .sh file, which is then made into an executable by typing `chmod 755 <<script name>>` in the command line and pressing enter. This turns the .sh file into a program that can be executed by the Unix shell. A final requirement is a bin directory in the home folder of the user. Scripts can be executed in any subfolder within the home directory and are executed by typing `./<<script name>>` and pressing enter while being in the folder within which the script resides. The scripts that were utilised in this project is listed at the end of the supplementary information and can be accessed electronically.

```
01  #!/bin/sh
02  # This is my first actual try
03  LIST=*.log
04  for i in $LIST
05  do
06  j=`echo $i | cut -d '.' -f 1`
07  exec &> "$j".output
08  while read f
09  do
10      if [[ $f == *"SCF Done:"* ]]; then
11          echo $f | cut -d ' ' -f 3,5
12      fi
13  done < $i
14  done
15  ---EMPTY SPACE---
```

Figure 8-2: Example of shell script for extracting electronic energies from Gaussian log files.

## Digital Supplementary Information

The attached CD contains the Gaussian input files (.inp or .gjf) and log files (.log) as well as the Shell scripts (.sh) used during the project. The files are divided into folders and organised according to the chapters. For each chapter a description is given as to how the files are arranged.

### Chapter 4

For Chapter 4 the files are separated into the three section in which the results are presented. Below the names of the files are not mentioned but are rather arranged systematically in well-described folders:

- Section 4.3
  - Calculations on the asymmetric unit of mdpaj
    - 1. Optimisation step
    - 2. Calculate orbitals from check
    - 3. Calculate spectra from check
- Section 4.4
  - b3lyp\_disp
    - 1. Optimisation step
    - 2. Calculate excited state energies from check
  - B97D
    - 1. Optimisation step
    - 2. Calculate excited state energies from check
  - B98
    - 1. Optimisation step
    - 2. Calculate excited state energies from check
  - cam-b3lyp\_disp
    - 1. Optimisation step
    - 2. Calculate excited state energies from check
  - M06\_disp
    - 1. Optimisation step
    - 2. Calculate excited state energies from check
  - PBEPBE\_disp

- 1. Optimisation step
- 2. Calculate excited state energies from check
- wB97XD
  - 1. Optimisation step
  - 2. Calculate excited state energies from check
- Section 4.5
  - Optimise in increasing amount of H<sub>2</sub>O experiment

## Chapter 5

Lattice energies were calculated using Material Studio and therefore the Material Studio working folder is presented as well as the Excel Sheets containing the summarised results. Furthermore the relevant cif and cif check files for this chapter are also provided.

- Diarylethene\_lattice\_energies\_Files
  - Documents
    - Energy\_calculations
    - Structures\_of\_the\_three\_known\_phases
- Lattice\_energies.xlsx
- Cif\_and\_cif\_check\_files

## Chapter 6

In Chapter 6 a three step process was described which involves scanning the dihedral angles, scanning the C\_C distance (distance  $d_1$ ) and calculating the excited state energies. This was done for each of the nine diarylethene compounds and thus arranged with each step in a separate folder for each of the compounds. For each step various Shell scripts were utilised which are provided in the relevant folder with a descriptive name.

For each compound an OriginPro document is provided (Energies.opj) which summarises the data in a single file with illustrations. The initial ring-opened and ring-closed structures are also provided (.log files) for each of the nine compounds. Lastly since for DA-2 the geometries were also optimised in the singlet state an extra step (step 4.) is provided and called “Singlet optimised and excited state energies.”

- DA-1
  - 1. Dihedral angles scan
  - 2. C\_C distance scan

- 3. Excited state energies
- Energies.opj
- pyridyl\_propyl\_closed.log
- pyridyl\_propyl\_open.log
- DA-2
  - 1. Dihedral angles scan
  - 2. C\_C distance scan
  - 3. Excited state energies
  - 4. Singlet optimisation and excited state energies
  - Energies.opj
  - difurylene\_photocentre.log
  - difurylene\_photocentre\_closed.log
- DA-3
  - 1. Dihedral angles scan
  - 2. C\_C distance scan
  - 3. Excited state energies
  - Energies.opj
  - difurylene\_methyl\_photocentre.log
  - difurylene\_methyl\_photocentre\_closed.log
- DA-4
  - 1. Dihedral angles scan
  - 2. C\_C distance scan
  - 3. Excited state energies
  - Energies.opj
  - dithienylene\_photocentre.log
  - dithienylene\_photocentre\_closed.log
- DA-5
  - 1. Dihedral angles scan
  - 2. C\_C distance scan
  - 3. Excited state energies
  - Energies.opj
  - dithienylene\_methyl\_photocentre.log

- dithienylethene\_methyl\_photocentre\_closed.log
- DA-6
  - 1. Dihedral angles scan
  - 2. C\_C distance scan
  - 3. Excited state energies
  - Energies.opj
  - dithienylethene\_fluorine\_photocentre.log
  - dithienylethene\_fluorine\_photocentre\_closed.log
- DA-7
  - 1. Dihedral angles scan
  - 2. C\_C distance scan
  - 3. Excited state energies
  - Energies.opj
  - dithienylethene\_methyl\_fluorine\_photocentre.log
  - dithienylethene\_methyl\_fluorine\_photocentre\_closed.log
- DA-8
  - 1. Dihedral angles scan
  - 2. C\_C distance scan
  - 3. Excited state energies
  - Energies.opj
  - pyridyl\_methyl\_closed.log
  - pyridyl\_methyl\_open.log
- DA-9
  - 1. Dihedral angles scan
  - 2. C\_C distance scan
  - 3. Excited state energies
  - Energies.opj
  - pyridyl\_ethyl\_closed.log
  - pyridyl\_ethyl\_open.log